Proposal for US Participation in KamLAND

Kam
LAND

Kamioka Liquid scintillator Anti-Neutrino Detector

March 1999

U.S. KamLAND Collaboration

J. Busenitz and J. Wolf
Department of Physics and Astronomy, University of Alabama

P. Alivisatos
Chemistry Department, University of California, Berkeley

R. N. Cahn, Y. D. Chan, X. Chen, S. J. Freedman*,
B. K. Fujikawa, K. T. Lesko, K.-B. Luk, H. Murayama, D. R. Nygren,
C. E. Okada, A. W. Poon, and H. M. Steiner
Physics Department and Lawrence Berkeley National Laboratory,
University of California, Berkeley

K. B. Lee, R. D. McKeown, V. Novikov, A. Piepke, and P. Vogel
Physics Department, California Institute of Technology

C. E. Lane and R. Steinberg
Physics Department, Drexel University

L. DeBraeckeleer, F. H. Cocks, C. R. Gould, C. R. Howell,
A. Kotwal, R. Rohm, and W. Tornow
Physics Department, Duke University and North Carolina State University,
Triangle Universities Nuclear Laboratory

B.-K. Kim and R. C. Svoboda
Department of Physics, Louisiana State University

B. Dieterle and S. Riley
Physics Department, University of New Mexico

C. Britton, W. Bryan, S. Frank, A. Wintenberg, and J. Wolker
Oak Ridge National Laboratory

N. Sleep
Geophysics Department, Stanford University

G. Gratta*, G. Horton-Smith, H. L. Liew, L. Miller, H. Tanaka, D. Tracy,
and Y-F. Wang
Physics Department, Stanford University

S. Berridge, W. Bugg, H. Cohn, Yu. Efremenko, E. Hart, and Yu. Kamyshkov
Physics Department, University of Tennessee

* U.S. KamLAND Spokespersons

Contents

1 Executive Summary

The persistence of deficits found by solar neutrino experiments and the impressive results from Super-Kamiokande on atmospheric neutrinos are the impetus for new, higher sensitivity measurements of neutrino oscillations. The KamLAND experiment will exploit the old Kamiokande underground site and the presence of large nuclear power reactors to obtain two orders of magnitude more sensitivity than previous reactor experiments. The substantial investment ($20M) already made by the Japanese government provides a firm basis for the development of this experiment. The U.S. KamLAND Collaboration proposes several initiatives designed to make this experiment robust against potentially crippling backgrounds and to increase its sensitivity still further, opening the way to the measurement of ^{7}Be solar neutrino.

The KamLAND detector, shown in Fig. 1, will employ one kiloton of liquid scintillator. This very large mass will result in approximately 750 $\overline{\nu}_e$ events per year from the reactors, though they are 140 to 200 km away. These events are detected in the traditional way, using the delayed coincidence between positron emission and the gamma from neutron capture. The very large ratio of this distance to the neutrino energy will make the experiment sensitive to $\Delta m^2 \approx 7 \times 10^{-6}$ eV^2 for large mixing. This would cover one of the two MSW solutions to the solar neutrino problem for the first time with a terrestrial experiment.

KamLAND can attack the solar neutrino problem directly as well. The observation of elastic scattering of solar neutrinos from ^{7}Be by electrons will produce large numbers of events (more than 300 per day for the full Standard Solar Model), albeit with rather low energies. If the observation of these events can be realized, KamLAND will have the potential to discriminate among the several explanations for the solar neutrino problem. This will place great demands on background suppresion, which can be met by minimizing radioactive contaminants in the construction of the detector itself, by keeping radon away from the active scintillator, and by designing electronics capable of providing extra discrimination. In all these areas, the U.S. Collaboration will make leading contributions. In fact, the reactor neutrino experiment will be enormously enhanced by the steps taken for the solar neutrino experiment. Reduced backgrounds and increased discrimination against surviving backgrounds will provide the kind of robustness so essential to producing a convincing result for a neutrino experiment.

The proposed U.S. contributions to KamLAND and their impact on the experiment are displayed in Table 1. The U.S. Collaborators bring experience gleaned from CHOOZ, Palo Verde, Super-Kamiokande, and SNO that is directly applicable to the challenges of KamLAND.

The U.S. Collaboration will be co-ordinated through LBNL, which has significant technical resources and infrastructure. This organization will enable the other U.S. institutions, many of which have been participating for over a year, to work even more effectively with the Japanese team. The time table for the experiment is very

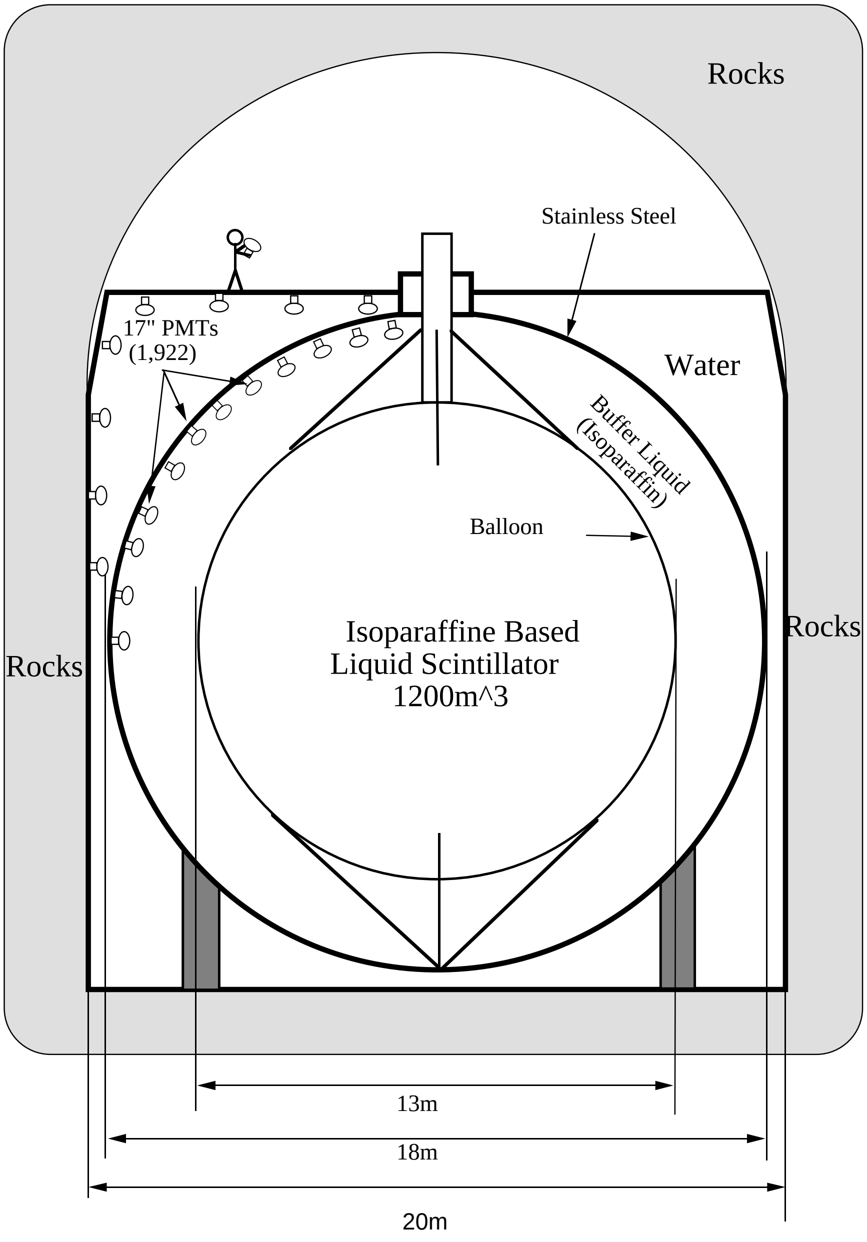

Figure 1: Schematic view of the KamLAND detector.

demanding. A requirement of the Japanese funding agency is that the experiment function early in 2001. The various U.S. contributions will have to be scheduled with this in mind, with the earliest efforts directed towards components that must be ready at turn-on.

Subsystem	Current Problems	Proposed U.S. Effort	Potential Impact	U.S. Inst.
Electronics Trigger, DAQ	lacking full event history no multihit	deadtimeless, multihit electronics	better bkgd rejection, results more robust	LBNL ORNL Stanford UTK
Balloon engineering, R&D	durability transparency	mechanical, chimney, calib. interface	improve lifetime, reduce bkgd. better resolution	LBNL Stanford
Radioassay Clean room design	main facilities in U.S.	Ge detector measurements, HIFR activation	reduce backgrounds	Caltech, LBNL, ORNL
Calibration	no n/γ separation calibration no position scan	build swing arm system n/γ calibration	improve resolution reduce bkgd.	Alabama LBNL, LSU New Mexico,
PMTs	652 missing	purchase	energy resolution bkgd. rej.	LBNL
Scintillator and radon impermeability	must specify monitoring system radon diffusion	scint. R&D radon studies	background reduction	Caltech Drexel Stanford
Veto system	no side veto no roof veto no segmentation	test/build side veto, build roof veto	background reduction	LSU TUNL UTK
Integration				LBNL

Table 1: How the proposed U.S. effort on KamLAND will address the outstanding issues confronting the experiment.

The large distance from the reactors to the KamLAND detector is a great advantage over previous reactor experiments like CHOOZ and Palo Verde. KamLAND's large fiducial volume, six times that of Borexino, will be especially important for the solar neutrino experiment. KamLAND is thus in an excellent position to obtain decisive results in both areas.

2 Physics Considerations

KamLAND is a multi-purpose detector with very pure organic liquid scintillator that can address a variety of scientific topics. KamLAND will increase existing experimental sensitivity to neutrino oscillations by two orders of magnitude in Δm^2 beyond previous reactor measurements. It will thus be the first terrestrial experiment with enough sensitivity to verify or exclude one of the possible solutions to the solar neutrino problem (specifically the large-mixing-angle MSW solution, or LMA). Given the technical and scientific challenges of building a low-background scintillation detector of the required size and sophistication, US participation will be critical in making KamLAND a truly convincing reactor neutrino experiment. The highest priority for KamLAND is a search for reactor anti-electron-neutrino oscillations with unprecedented long baseline.

In principle, the detector will also be capable of detecting solar neutrinos. However, this will require even more rigorous control of the radioactivity in construction components and scintillator radiopurity at the frontier of technical feasibility. Measures to control radioactive backgrounds for both the reactor neutrino experiment and the solar neutrino experiment must begin at construction. How well KamLAND will ultimately do in achieving the scientific goals for solar neutrinos depends critically on the actual background levels that are eventually achieved. Despite the additional challenges, the scientific motivation for studying ^{7}Be neutrinos from the Sun is also compelling, making it a worthy second priority for KamLAND. The US contributions can significantly enhance KamLAND's capabilities, bringing the solar neutrino program into reality.

2.1 Neutrino Oscillation

The experimental hints for neutrino mass are at present based on the phenomenon of neutrino oscillations [1, 2]. If neutrinos are massive particles that behave similarly to quarks, the states with a definite mass (i.e., the "mass eigenstates" which propagate as plane waves in a vacuum) are not necessarily the partners of the charged leptons that couple to the vector bosons $W^{\pm}$ in doublets (*i.e.*, the weak eigenstates). The weak eigenstates $|\nu_l\rangle$ will be in such a case linear superpositions of the mass eigenstates $|\nu_i\rangle$

$$|\nu_l\rangle = \sum_i U_{l,i} |\nu_i\rangle \ , \tag{1}$$

where the coefficients $U_{l,i}$ form the leptonic mixing matrix. If we assume that only three neutrinos can contribute in the Eq. (1) above, then U is a unitary 3×3 matrix.

If the matrix U in Eq. (1) is not diagonal, there are neutrino oscillations in which a neutrino which was initially in the weak eigenstate l can be spontaneously transformed, at least in part, into another weak eigenstate neutrino of flavor l'.

Neutrino oscillation experiments are often analyzed in a simplified way by assuming that only two neutrino flavors mix, *e.g.* e and μ. The mixing matrix U then depends only on one mixing angle θ, and the oscillation probability is given by a simple formula

$$U = \begin{pmatrix} \cos\theta & \sin\theta \\ -\sin\theta & \cos\theta \end{pmatrix} \tag{2}$$

$$P(\nu_{\mathrm{e}} \rightarrow \nu_\mu, L) = \sin^2 2\theta \sin^2\left(\frac{\Delta m^2 L}{4E}\right) = \sin^2 2\theta \sin^2\left(1.27\frac{\Delta m^2(\mathrm{eV}^2)L(\mathrm{m})}{E(\mathrm{MeV})}\right) \tag{3}$$

Here $\Delta m^2 \equiv m_1^2 - m_2^2$. The probability that ν_{e} remains ν_{e} is obviously $P(\nu_{\mathrm{e}} \rightarrow \nu_{\mathrm{e}}, L) = 1 - P(\nu_{\mathrm{e}} \rightarrow \nu_\mu, L)$. The oscillation length is

$$L_{osc} = 2\pi\frac{2E_\nu}{\Delta m^2} = \frac{2.48E_\nu(\mathrm{MeV})}{\Delta m^2(\mathrm{eV}^2)}\mathrm{meters}\ . \tag{4}$$

To test for oscillations, one can perform either an *appearance* search in which one looks for new neutrino flavor, or a *disappearance* test in which one looks for a change in the flux.

When neutrinos propagate in matter, such as in the solar interior, the oscillation pattern may be modified. This happens because electron neutrinos can forward scatter on electrons by charged current interactions while other neutrino flavors cannot. Under favorable circumstances a resonance enhancement of the oscillation amplitude, the so-called Mikheyev-Smirnov-Wolfenstein (MSW) effect [3], can take place.

2.1.1 Neutrino Oscillation Experiments

Numerous searches for neutrino oscillations were performed during the last two decades. Most of them resulted in excluding ranges of the parameters Δm^2 and $\sin^2 2\theta$. See Figure 2 for the case $\nu_{\mathrm{e}} - \nu_\mu$. However, at the present time there are three kinds of measurements that suggest the existence of neutrino oscillations Only these positive results will be discussed here. Details can be found in the latest edition of the Review of Particle Physics [4].

The earliest indication for neutrino oscillations came from measurements of solar neutrinos. The Sun produces an intense flux of electron neutrinos as a byproduct of the fusion reactions that generate solar power. There are several reactions involved and each produces a component of the overall neutrino flux whose spectral shape is well-determined from standard nuclear physics, but whose absolute flux depends on the details of solar structure. Measurements of solar luminosity and helioseismological vibration modes imply that solar structure is sufficiently well understood such that the neutrino flux can be predicted with accuracies varying from roughly 1% to 20%, depending on the specific component.

The solar neutrino fluxes have been measured in five experiments so far. All of them report a deficit, i.e., the measured flux is less than the expected one. Moreover, the reduction may depend on the neutrino energy, inferred experimentally from the thresholds of the individual detectors. The only viable explanation of the deficit

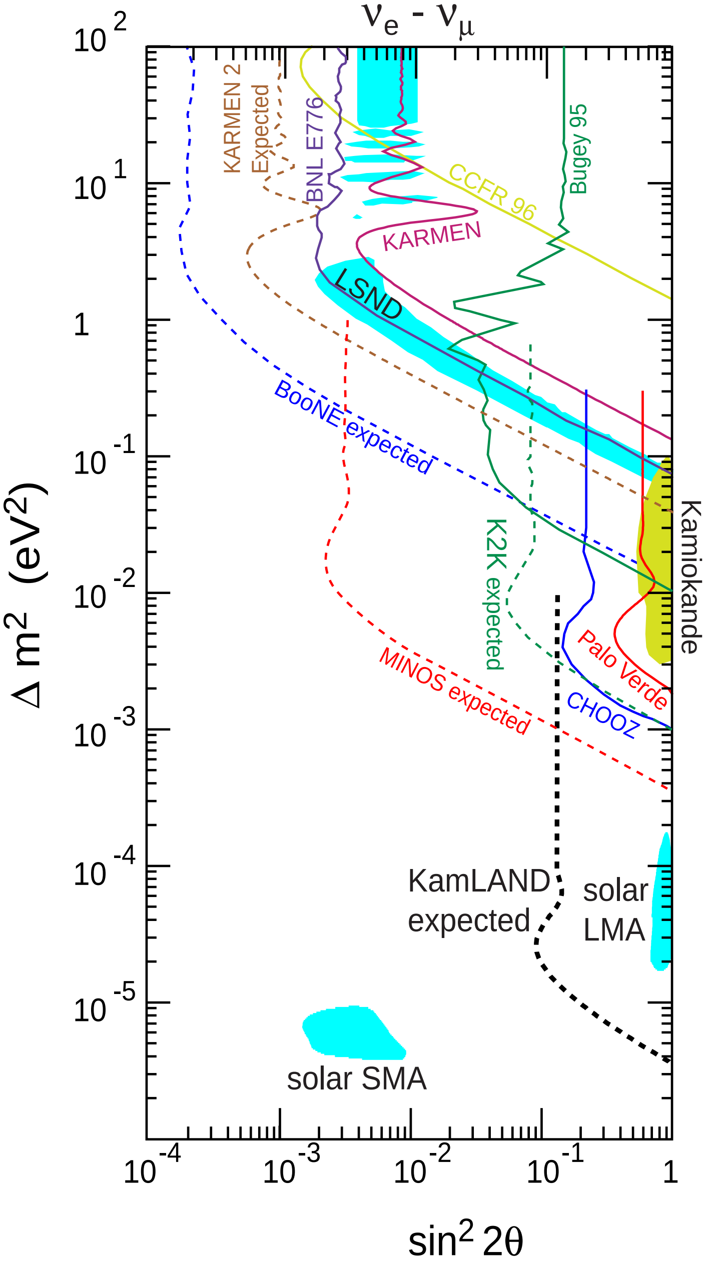

Figure 2: Allowed and excluded regions in the $\Delta m^2 - \sin^2 2\theta$ plane for $\nu_e - \nu_\mu$ oscillations. The existing limits are compared with current and future experiments and the region obtained by interpreting the solar neutrino anomaly as due to oscillations. For KamLAND, the region corresponds just to the reactor experiment. The MSW mechanism is used in deriving two of the solar neutrino regions. The region preferred by Kamiokande atmospheric neutrino data is now disfavored by Super-Kamiokande data. The sensitivity of reactor experiments is the same for $\nu_e - \nu_\tau$ oscillations. Limits are at 90% CL. The Palo Verde curve is for 70 days of running.

appears to be neutrino oscillation (ν_e disappearance). Because of its relevance to KamLAND, we review the status of the solar neutrino problem in more detail in Section 2.1.2.

The second set of measurements that can be interpreted as evidence for neutrino oscillations is the "atmospheric neutrino anomaly." Primary cosmic rays impinging on the nitrogen and oxygen nuclei at the top of the earth's atmosphere produce pions, which subsequently decay via $\pi \rightarrow \mu\bar{\nu}_\mu, \mu \rightarrow \mathrm{e}\bar{\nu}_\mathrm{e}\nu_\mu$. The resulting atmospheric neutrinos therefore are expected to follow the $\nu_\mu : \nu_\mathrm{e} = 2 : 1$ ratio, which is essentially independent of the details of the complicated process that created them. In addition, one can deduce the direction of the incoming neutrinos from the direction of the leptons (e and μ) created by the charged current interactions, at least at high enough energies. Again, one is reasonably confident that this zenith angle distribution can be accurately predicted; especially its up-down symmetry follows purely from geometry and is believed to be robust. If the ν_μ and/or ν_e neutrinos oscillate, one expects deviations from the 2:1 ratio mentioned above. Also, since the zenith angle is simply related to the neutrino path length, one expects that the lepton yield will have a dependence on the zenith angle.

Both signatures of neutrino oscillations were in fact observed. The ν_μ/ν_e ratio is noticeably smaller, only about 60% of the expected value. This result has been confirmed in four detectors thus far [5, 6, 7, 8], while contradicted by one (Fréjus) with smaller statistics [9]. The anomalous zenith angle dependence (a violation of up-down symmetry) was first observed in Kamiokande [10], and has been now confirmed, with much better statistical significance, by Super-Kamiokande [11]. If these effects indeed signify neutrino oscillations (and we do not have another viable explanation) then the corresponding mixing angle is large, $\sin^2 2\theta \approx 1$ [12]. The interpretation of the anomaly as ν_e–ν_μ oscillation gives the parameter range in Figure 2 labeled "Kamiokande." The value of the mass parameter Δm^2 remains uncertain, but is clearly in the range 10^{-1}–10^{-3} eV^2. CHOOZ [13] and Palo Verde [14] contradict this result if only ν_e-ν_μ oscillations are considered, though the results might be reconciled if all three neutrino flavors are considered. Similarly, while Super-Kamiokande data prefer $\nu_\mu \rightarrow \nu_\tau$ oscillations [15], it is not clear that $\nu_\mu \rightarrow \nu_e$ oscillations are impossible [16]. K2K will soon address the same question. KamLAND plans to convincingly confirm or reject this possibility with a "laboratory" measurement.

Finally, the only indication for oscillations involving man-made neutrinos comes from the LSND experiment which finds evidence for the $\bar{\nu}_\mu \rightarrow \bar{\nu}_\mathrm{e}$ [17] and, with more limited statistics, also for $\nu_\mu \rightarrow \nu_\mathrm{e}$ [18]. The former channel uses neutrinos from the pion and muon decay at rest, with energies less than $m_\mu/2$. The latter channel uses neutrinos from the pion decay in flight, which have somewhat higher energies. These are appearance experiments; the observed signal should be absent if neutrinos do not oscillate. The well determined quantity is the oscillation probability $P = (3.1 \pm 0.09 \pm 0.05) \times 10^{-3}$ [19]. The values of Δm^2 and $\sin^2 2\theta$ are so far not determined very well (see the region labeled "LSND" in Figure 2). This result has not been independently confirmed but will be tested by KARMEN-II [20] and BooNE [21].

With the exception of the LSND evidence, these results came from large underground detectors. A number of new experiments are in various stages of planning or construction. It is very exciting that the next decade can bring the final resolution of the neutrino mass puzzle, and KamLAND can play an essential role in this enterprise.

2.1.2 Status of the Solar Neutrino Puzzle

The Sun produces an intense flux of electron neutrinos as a consequence of the fusion reactions generating solar energy, with the combined effect

$$4p + 2e^- \to {}^4\mathrm{He} + 2\nu_e + 26.73\ \mathrm{MeV} - E_\nu\ , \tag{5}$$

where E_ν is the neutrino energy ($\langle E_\nu \rangle \simeq 0.6$ MeV). The solar neutrino spectrum consists of several components [22]; the expected flux according to the Standard Solar Model (SSM) [23] is shown in Figure 3. The observation of solar neutrinos directly tests the SSM, and more generally the theory of stellar evolution and structure. At the same time, it offers an important and unique opportunity to investigate neutrino properties.

So far, five experiments have published results on solar neutrino measurements, and the signal in each of them is less than the expectation. See Table 2. Radiochemical experiments (^{37}Cl at Homestake [24], threshold 814 keV; ^{71}Ga at Gran Sasso [25], and ^{71}Ga at Baksan [26], threshold 233 keV) use neutrino capture on the indicated nuclear targets to produce radioactive daughter nuclei, which are extracted and counted after exposure to solar neutrinos. These experiments measure the solar neutrino flux above their respective thresholds (weighted with the energy dependence of the corresponding cross section) and so provide only indirect information on the contribution of the individual components of the solar neutrino spectrum. The other two experiments are real-time measurements of the electron recoil spectra from the ν-e scattering (Kamiokande [27] and Super-Kamiokande [28]). Due to their relatively high threshold (currently 5.5 MeV) these experiments observe only the high energy part of the ^{8}B neutrino spectrum.

While these experiments have convincingly shown that the Sun indeed is a source of electron neutrinos, and that the corresponding flux has the correct order of magnitude, a consistent explanation of all observations is very difficult, if not impossible, in the framework of the SSM (see, *e.g.*, [29]). From the Kamiokande and Super-Kamiokande measurement one is able to determine the ^{8}B flux. Combining this with the Homestake result leaves no room for ^{7}Be solar neutrinos. This makes an astrophysical solution inconsistent, because ^{8}B nuclei are produced from ^{7}Be in the Sun. A similar conclusion can be reached using the ^{71}Ga measurements. Since the *pp* neutrino flux is essentially determined by the known solar luminosity, the ^{71}Ga measurements again leave no room for ^{7}Be neutrinos which should contribute significantly to the ^{71}Ga signal. Thus one is led to the conclusion that:

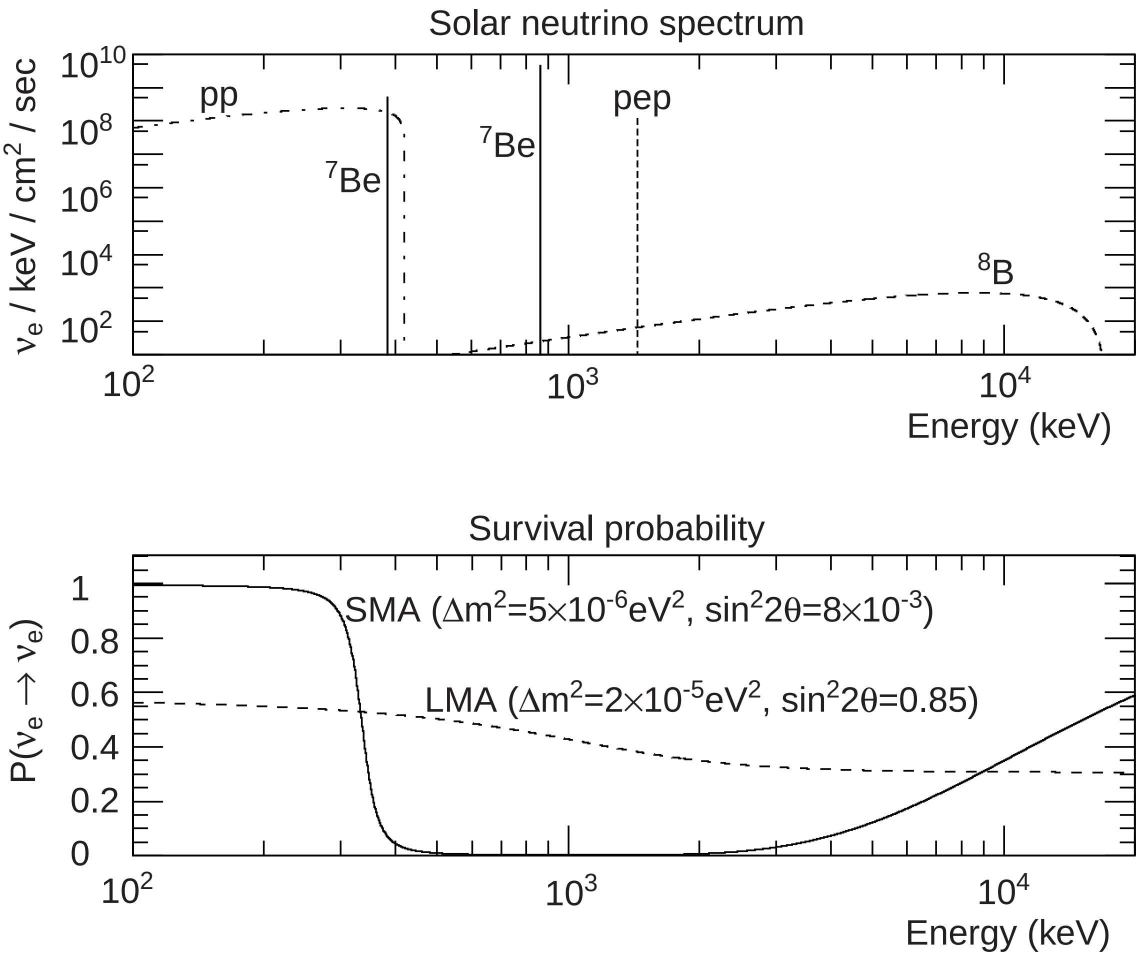

Figure 3: The upper figure depicts the most important components of the solar ν_e spectrum, normalized to the flux given by the SSM. For the discrete line sources the flux is given in cm^{-2}s^{-1}. The lower figure shows the neutrino survival probability for matter-enhanced neutrino oscillations.

Source	Cl(SNU)	Ga(SNU)	Water(data/BP98)
pp	0.0	69.6	
pep	0.2	2.8	
^{7}Be	1.15	34.4	
^{8}B	5.9	12.4	1
All	$7.7^{+1.2}_{-1.0}$	129^{+8}_{-6}	
Data	$2.56 \pm 0.16 \pm 0.16$ (Homestake)	$66.6^{+7.8}_{-8.1}$, $77.5 \pm 6.2^{+4.3}_{-4.7}$ (SAGE), (GALLEX)	$0.474^{+0.010+0.017}_{-0.009-0.014}$ (SuperK)

Table 2: Standard Model Predictions (BP98) for important solar neutrino fluxes and neutrino capture rates, with 1σ uncertainties from all sources (combined quadratically).

- these experiments indicate that the ^{7}Be ν_e solar neutrino flux is strongly suppressed;
- the observations are not only incompatible with the SSM, but also with most of its non-standard modifications.

In view of the above, it is tempting to invoke explanations based on neutrino oscillations. In particular, assuming the MSW mechanism, one can account for all observations by assigning particular values to the fundamental parameters Δm^2 and $\sin^2 2\theta$. Three possibilities are usually referred to as large mixing angle solution (LMA), small mixing angle solution (SMA), and low Δm^2 solution (LOW). LMA and SMA regions are shown in Figure 2, and the corresponding survival probabilities, calculated using the Landau-Zener approximation [30], is depicted in the lower part of Figure 3. A fourth island in the Δm^2 vs. $\sin^2 2\theta$ space involves the so called "just so" or vacuum (VAC) oscillations. In that case there are no matter enhancement effects and the oscillation length is comparable to the Sun-Earth distance (typical best fit parameters are $\Delta m^2 = 7.8 \times 10^{-11}$ eV^2 and $\sin^2 2\theta = 0.71$) [31]. All four solutions are shown in Fig. 4.

For each of these four solutions, one can hypothesize oscillation into an active neutrino $\nu_a = \nu_\mu$ or ν_τ which has neutral-current interaction or a sterile neutrino ν_s which does not.[1]

As we will see in the Section 2.2, KamLAND can directly test the LMA solution of the solar neutrino puzzle with a laboratory-style measurement of reactor neutrinos (assuming from CP invariance that the issues are the same for neutrinos and anti-

---

[1] From the global fit to the overall rates of Super-Kamiokande, Homestake and two Gallium experiments (GALLEX and SAGE), the LMA, LOW, and VAC solutions with a sterile neutrino give poor fits [29]. We discuss them here for the sake of completeness since some astrophysical or nuclear physics uncertainties could change the goodness of the fits.

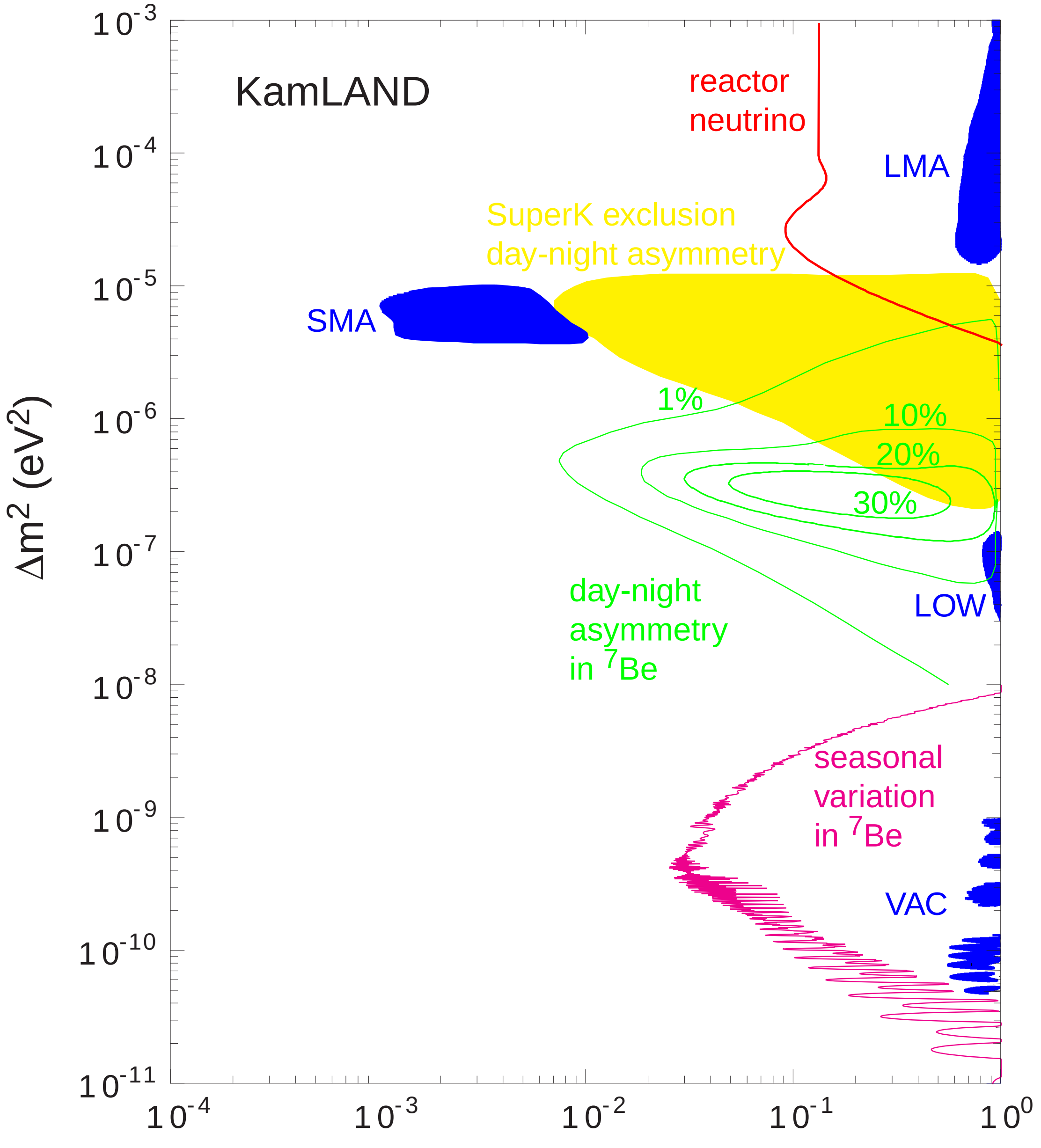

Figure 4: Various solutions to the solar neutrino problem and the sensitivity of KamLAND to them from the reactor neutrino experiment, and *if possible*, from the study of ^{7}Be solar neutrinos. The LMA solution is covered by the reactor neutrino experiment, the LOW solution by day-night asymmetry in the ^{7}Be neutrino flux, and the VAC solution by the seasonal variation in the ^{7}Be neutrino flux. The potential impact of KamLAND on the SMA solution is shown in Fig. 12. The seasonal variation sensitivity region is shown for 95% CL, with statistical errors only. The potential reactor neutrino exclusion domain is shown for 90% CL. The preferred regions for LMA, SMA, LOW, and VAC are 90% CL.

neutrinos). In addition, KamLAND can complement such unique measurements with the direct and independent observation of the ^{7}Be component of the solar neutrino spectrum, if an extremely low background can be realized. KamLAND can measure the ^{7}Be neutrino flux and test if it agrees with the SSM rate. If not, it is capable of determining which, if any, of the above four solutions is correct.

2.2 Reactor Oscillation Experiment

KamLAND, because of the combination of long baseline and low antineutrino energy, will achieve an unprecedented sensitivity, $\Delta m^2 \leq 10^{-5}$ eV^2. This will exceed today's most sensitive reactor experiments by more than two orders of magnitude. This sensitivity to Δm^2 is good enough for KamLAND to be the first direct test of the large mixing angle MSW solution to the solar neutrino problem.

The difficulty of a reactor neutrino experiment at this scale should not be minimized. The US participants propose to enhance the reactor program by increasing phototube coverage, providing an efficient veto, building a system of advanced electronics, and developing systematic methods of calibration in order to make the results convincing.

2.2.1 Laboratory Neutrino Oscillation Experiments

The regions of Δm^2 and $\sin^2 2\theta$ covered by different accelerator, reactor, and solar neutrino experiments are shown in Figure 2 for oscillations involving electron neutrinos. Many recent neutrino experiments have concentrated on the region relevant to the atmospheric neutrino anomaly $\Delta m^2 \simeq 10^{-3}$–$10^{-2}$eV^2. In KamLAND, reactor neutrinos access a very different region of the $\Delta m^2 - \sin^2 2\theta$ plane, down to 6×10^{-6} eV^2 in Δm^2, 100 times smaller than what is projected for MINOS [32] and any other accelerator experiment.

2.2.2 Very-Long Baseline Oscillations with KamLAND

Nuclear reactors produce $\bar{\nu}_{\rm e}$ isotropically in the β decay of the neutron-rich fission fragments. Electron anti-neutrinos are primarily captured on protons in the detector's liquid scintillator according to the reaction:

$$\bar{\nu}_{\rm e} + p \rightarrow e^+ + n.$$

At lowest order the approximate cross section is [33],

$$\begin{aligned}\sigma(E_\nu) &= \frac{2\pi^2}{m_{\rm e}^5 f \tau_n} p_e E_e \\ &= 9.5 \times 10^{-44} p_e(\text{MeV}) E_e(\text{MeV})\ \text{cm}^2, \end{aligned} \tag{6}$$

where $E_e = E_\nu - \Delta M$ with $\Delta M = 1.293$ MeV is the $n - p$ mass difference, $\tau_{\rm n}$ is the neutron lifetime, $f = 1.69$ is the integrated Fermi function for neutron β-decay, and p_e and E_e are the momentum and energy of the positron. Various small corrections to the above formula (from weak magnetism, neutron recoil, QED effects) are well understood and reliably calculated. The angular distribution of the created positrons and recoil neutrons is also well understood.

The positron in the final state deposits its energy in ionization and then annihilates. The neutron is thermalized and captured in the $\rm n + p \rightarrow d + \gamma$ reaction, where the photon energy is 2.2 MeV. The neutron mean thermalization time is 200 μs and anti-neutrino events have a clear signature of a delayed coincidence between the (prompt) positron signal and the (delayed) neutron capture gamma-ray. The neutrino energy threshold of the reaction is $\Delta M + m_{\rm e} \simeq 1.8$ MeV.

For all practical purposes for each reactor the anti-neutrino flux and spectrum depend only on the composition of the core in terms of the four isotopes ^{235}U, ^{238}U, ^{239}Pu and ^{241}Pu. Neutrinos are produced by long chains of daughter isotopes and hundreds of different β-decays have to be included to account for the observed yields. The modeling of such processes is quite a formidable task but there is now very good agreement between theoretical calculations and experimental data. There are two experimental cross checks of the theoretical models. In one case the electron spectra for fission-produced chains can be experimentally measured for each of the four parent isotopes. From these data, available only for ^{235}U, ^{239}Pu and ^{241}Pu, anti-neutrino spectra can be derived without loss of accuracy [34], obtaining a total uncertainty on the flux of about 3%. Alternatively, anti-neutrino flux and spectra have been directly measured [35] in several high-statistic experiments with detectors of known efficiency at small distances. These data are usually a by-product of previous reactor oscillation experiments where the anti-neutrinos have been measured at different distances. Since these observations have been found to be consistent with a $1/r^2$ law (no oscillations at short baselines) they can now be used as a determination of the absolute anti-neutrino spectra. A total error of about 1.4% has been achieved in these measurements. The situation is illustrated in Figure 5 where the measured anti-neutrino induced positron spectrum is compared with its prediction from β-spectroscopy.

All experimental methods and calculations agree with each other within errors so that, given the history of power and fuel composition for a reactor, its anti-neutrino energy spectrum can be computed with an error of about 3%. We note here that for this kind of experiment a "near measurement" is not required. In essence, all the information needed on the shape and magnitude of the primary spectrum is predicted

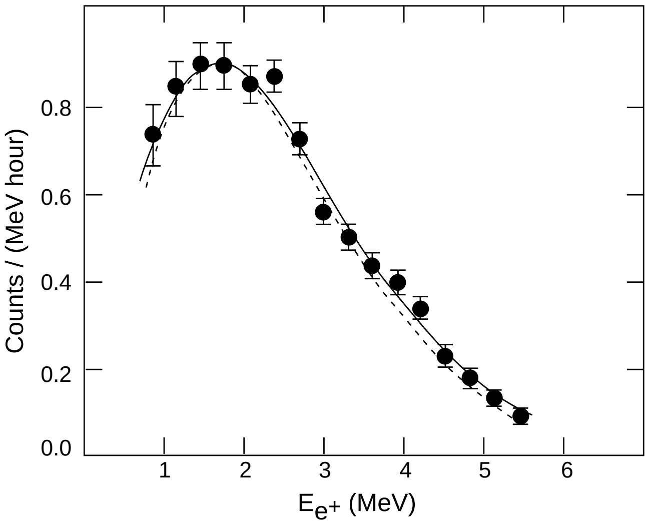

Figure 5: Positron spectrum measured at 45.9 m from the core of the Gösgen reactor [36]. Data points are obtained after background subtraction, errors are statistical only. The solid curve is a fit to the data assuming no oscillations. The dashed curve is derived independently by β-spectroscopy.

from the previous generations of experiments, assuming that no oscillations take place at short ($\lesssim$ 1 km) baselines.

Since the neutrino spectrum is only measured above the 1.8 MeV threshold, only short-lived (energetic) β^- decays contribute to the useful flux and the "neutrino luminosity" tracks very well in time the power output of the reactor. Generally, by a few hours after a reactor shut down the neutrino flux above threshold is negligible. Similarly, for neutrinos above threshold, equilibrium is already established by several hours after a reactor is turned on.

There are 16 commercial nuclear power plants in Japan, supplying one-third (or 130 GW thermal at maximum power) of the total electric power in the country [37]. At the Kamioka site there is an anti-neutrino flux of 1.3×10^6 cm^{-2}s^{-1} for $E_{\bar{\nu}} > 1.8$MeV at maximum power from these reactors. Of this flux, 80% comes from reactors between 140 km and 210 km away, so there is a limited range of baselines. The total number of $\bar{\nu}p \rightarrow ne^+$ events expected from reactors is 1075 kton^{-1}year^{-1} (again at maximum power for a C_nH_{2n+2} target) with 100% live time of the detector. The thermal power, distance, $\bar{\nu}_e$ maximum flux, and the expected event rates from each power station are listed in Table 3.

Since the measurement of absolute flux is essential to reach the best sensitivity, it is customary in reactor experiments to measure the background at zero or at least low reactor power. In our case this is possible even in the presence of a large number of reactors since many are shut down for preventive maintenance in the fall and spring

Reactor Site	Distance (km)	# of reactors	Therm. Power (max) (GW)	Max. Flux (10^5 $\bar{\nu}_e$ /cm^2/s)	Max.Event rate events/kt-year
Kashiwazaki	160	7	24.6	4.25	348
Ohi	180	4	13.7	1.90	154
Takahama	191	4	10.2	1.24	102
Hamaoka	214	4	10.6	1.03	84
Tsuruga	139	2	4.5	1.03	84
Shiga	81	1	1.6	1.08	89
Mihama	145	3	4.9	1.03	84
Fukushima-1	344	6	14.2	0.53	44
Fukushima-2	344	4	13.2	0.49	40
Tokai-II	295	1	3.3	0.17	14
Shimane	414	2	3.8	0.10	8
Ikata	561	3	6.0	0.08	7
Genkai	755	4	6.7	0.05	4
Onagawa	430	2	4.1	0.10	8
Tomari	784	2	3.3	0.02	2
Sendai	824	2	5.3	0.03	3
Total		51	130	13.1	1075

Table 3: Expected contribution of different reactors to the neutrino rates detected in KamLAND in the case of no oscillations. The event rate in the last column has been calculated assuming no oscillation and 100% “live time” for each reactor. Thermal power, flux and event rates are all given for the maximum operation of the reactors. Typically, annual averages are about 80% of the maximum.

when the demand for electricity is lower.

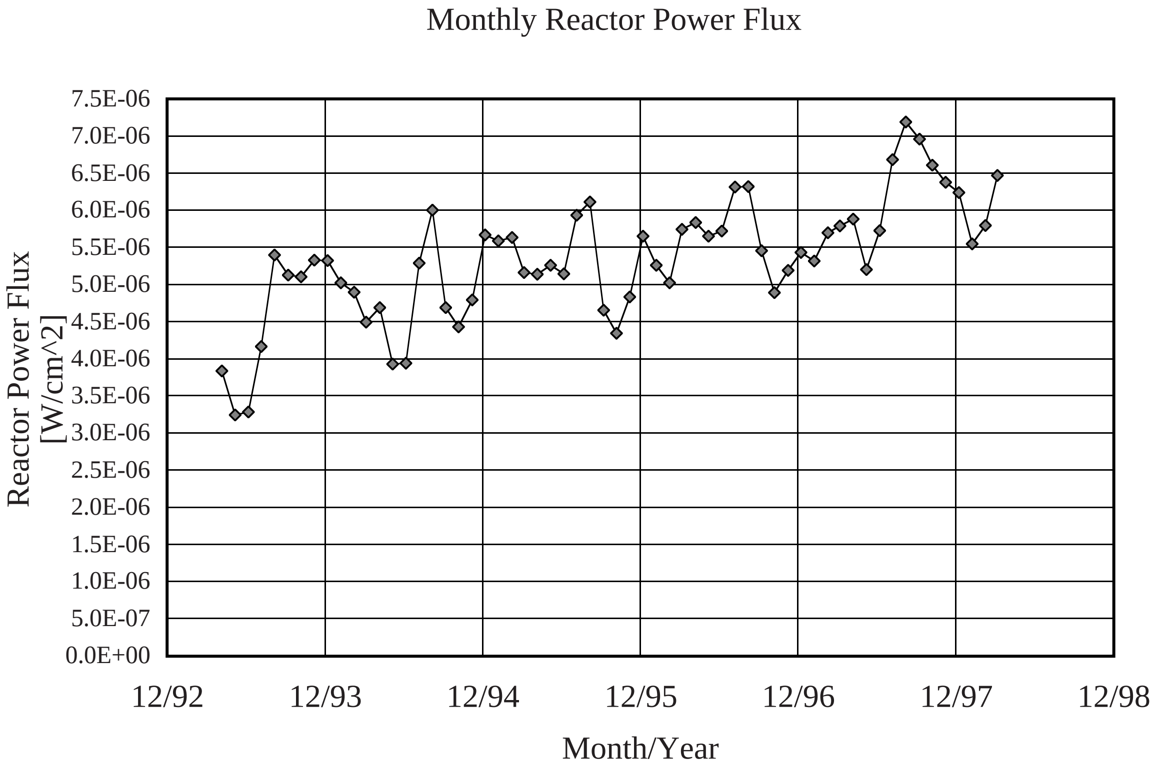

Figure 6: Electrical power flux at Kamioka from Japanese reactors as function of time. Low power periods in the fall season are alternated with peak high power in the summer. The electrical power flux is defined by $\sum_i P_i/(4\pi L_i^2)$, where P_i is the electrical power of the i-th reactor at a distance L_i from Kamioka.

As an illustration, Figure 6 shows the electrical power flux at Kamioka as function of time during the past six years, where 30% variations are seen. Such variations can be used to estimate the background. The electrical power flux is defined by $\sum_i P_i/(4\pi L_i^2)$, where P_i is the electrical power of the i-th reactor at a distance L_i from Kamioka.[2] Note that the neutrino event rate, if there are no oscillations, is proportional to this quantity.

2.2.3 Determining the oscillation parameters

Here we explain in detail how the values (or limits) of the oscillation parameters Δm^2 and $\sin^2 2\theta$ will be determined at KamLAND.

---

[2] The electrical power is smaller than the thermal power given in Table 3 by an efficiency factor of about 33%.

First, for each reactor listed in Table 3 we will know the thermal power as a function of time (supplied by the corresponding power company), and also as a function of time the fraction of power derived from the fission fuels ^{235}U, ^{239}Pu, ^{241}Pu, and ^{238}U. Thus, using the index i to denote the individual reactors, and the index f to denote the four fissioning isotopes, we will have the set of thermal powers $P_{i,f}(t, d_i)$, where d_i are the distances to KamLAND listed in Table 3. Multiplying these numbers by the known energy release per fission, and the known (see above) $\bar{\nu}_e$ spectrum at $d_i = 0$ we obtain for each reactor the initial spectrum $S_i(t, d_i, E_\nu) = \sum_f S_{i,f}(t, d_i, E_\nu)$. The uncertainty in these initial spectra is less than 2% each. Note that the uncertainty caused by the time variation of the fuel composition is less than the error in individual spectra. The thermal power of each reactor is measured with $\leq 1\%$ uncertainty by the power company.

The predicted counting rate at the KamLAND detector for 100% efficiency from each reactor is then

$$N_i(t, E_{e^+}, \Delta m^2, \sin^2 2\theta) = S_i(t, d_i, E_\nu) \times N_p \times \frac{\sigma(E_\nu)}{4\pi d_i^2} \times [1 - \sin^2 2\theta \sin^2 \left(\frac{\Delta m^2 d_i}{4E_\nu}\right)] \ , \quad (7)$$

where N_p is the number of target protons, $\sigma(E_\nu)$ is the cross section (6) (but with all small corrections included), and the neutrino energy and positron kinetic energy are related by $E_\nu = E_{e^+} + \Delta M$. Note that in a large detector such as KamLAND the annihilation radiation will be always recorded together with the positron kinetic energy, so that it is reasonable to assume an efficiency of $\sim 100\%$. This assumption will be carefully verified with calibration data.

Finally adding the contribution of all reactors together, integrating over all positron energies, and adding the background rate we obtain the expected signal

$$N_{tot}(t, \Delta m^2, \sin^2 2\theta) = \int \mathrm{d}E_{e^+} \sum_i N_i(t, E_{e^+}, \Delta m^2, \sin^2 2\theta) + Bkg \ . \quad (8)$$

As we discussed above, the anti-neutrino energy spectrum is modified by oscillations so that, in general, additional information is available besides the absolute neutrino count. In our case, even in the absence of one single baseline, the energy spectrum still plays an important role. This is shown in Figure 7 where the energy spectrum is plotted for the case of no oscillation (original reactor spectrum) and for three different sets of parameters.

A slight complication is from the possible contribution of geological anti-neutrinos. It is believed that 40% of the heat (16 TW) emitted from the Earth's surface (40 TW) comes from ^{238}U and ^{232}Th chains in the Earth. The β-decays in their chains produce anti-neutrinos, which can constitute background to the reactor neutrinos. (This by itself is an interesting scientific question that can be addressed by KamLAND, and is discussed in more detail in Appendix 6.) The event rates for geological neutrinos are small in KamLAND, about 50 events/year (with a large uncertainty depending on models). The energy spectra of anti-neutrinos from ^{238}U and ^{232}Th chains are

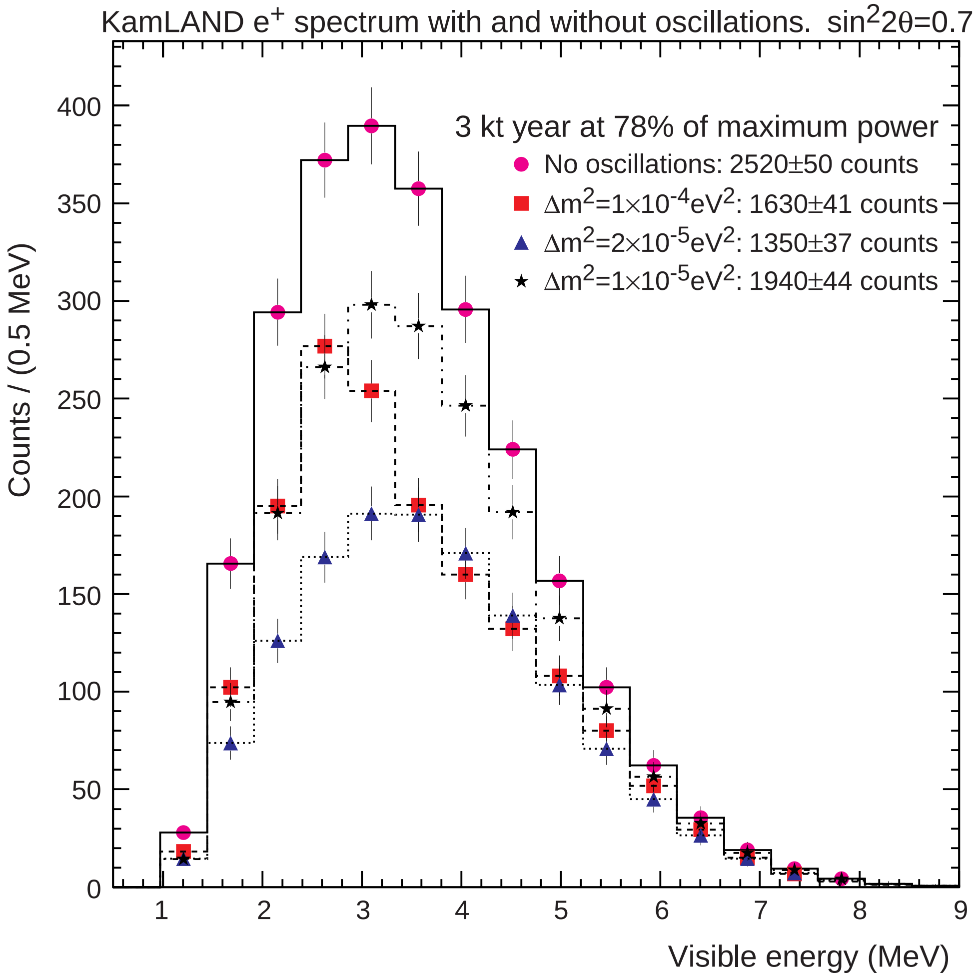

Figure 7: The visible e^+ energy spectrum (including photons from e^+e^- annihilations) from reactor neutrinos expected in KamLAND for different types of oscillation scenarios and for the case of no oscillations. It assumes an exposure of 3-kt-y at 78% of the maximum power flux and 100% detection efficiency.

well known and do not deposit more than 2.49 MeV (including photons from e^+e^- annihilations). The observed positron spectrum at KamLAND will be fit with free normalizations for the geological anti-neutrinos and we expect little degradation in the sensitivity of the reactor neutrino experiment from geological anti-neutrinos.

The sensitivity of the reactor oscillation experiment that can be performed at KamLAND obviously depends on the background level which will be actually achieved. As mentioned above the background level can be determined from the time variation of the reactor signal, as illustrated in Fig. 6. Let us summarize here the estimate of various components in the background described in more detail in the next section. Energetic neutrons from muon spallation in the surrounding rock constitute the largest contribution to the correlated background: a prompt interaction of a neutron, followed by its delayed capture. Requiring the electron anti-neutrino event signature – a prompt signal with a minimum energy of 1 MeV followed by a delayed neutron capture signal – these energetic neutrons are estimated to generate 0.05 background events/day. This is to be compared to 2 signal events/day from reactor neutrinos. The rate of accidental coincidences (10–500 μs window) between background events with a minimum energy of 1 MeV is only 0.05 events/day (uncorrelated background). In our simulation we conservatively took the signal-to-background ratio to be 10:1. Given its smallness, the background cannot be determined accurately from the time variation of the signal correlated to the reactor power. On the other hand, the uncorrelated component of the background will be determined experimentally. The correlated component from fast neutrons has its origin in either muons going through the detector or from muons outside the detector. In the former case, since the muon veto inefficiency will be known, the corresponding background can be determined. One can also use events that occur shortly after the detection of cosmic ray muons in the veto counter to measure the background from muon spallation. In the case of fast neutrons coming from the cavity, the corresponding background for a very large detector such as KamLAND can be determined by looking at the counting rate as a function of the distance from the detector wall.

Guided by these considerations we show in Figure 8 the region of sensitivity for different assumptions about the signal-to-noise and the uncertainty with which the background has been determined. In all cases we assume an exposure of 3 kt-year with 78% of the maximum power flux on average, and use (for the purpose of this figure) only the total count rate after the cuts but not the measured energy spectrum. The sensitivity is shown for three different assumptions. Case a) is with no background. Case b) is with signal-to-background ratio of 10 assuming that the background is determined from measurements of uncorrelated component, muon spallation and dependence of the event on the distance from the wall, to 25%. The last case c) the determination of the background is only from time variation with the reactor power. Even with the most pessimistic assumption c), a mass-difference-squared $\Delta m^2 \simeq 6 \times 10^{-6}$ eV^2 is reached at the maximal mixing, entirely covering the large mixing angle (LMA) solution for the solar neutrinos.

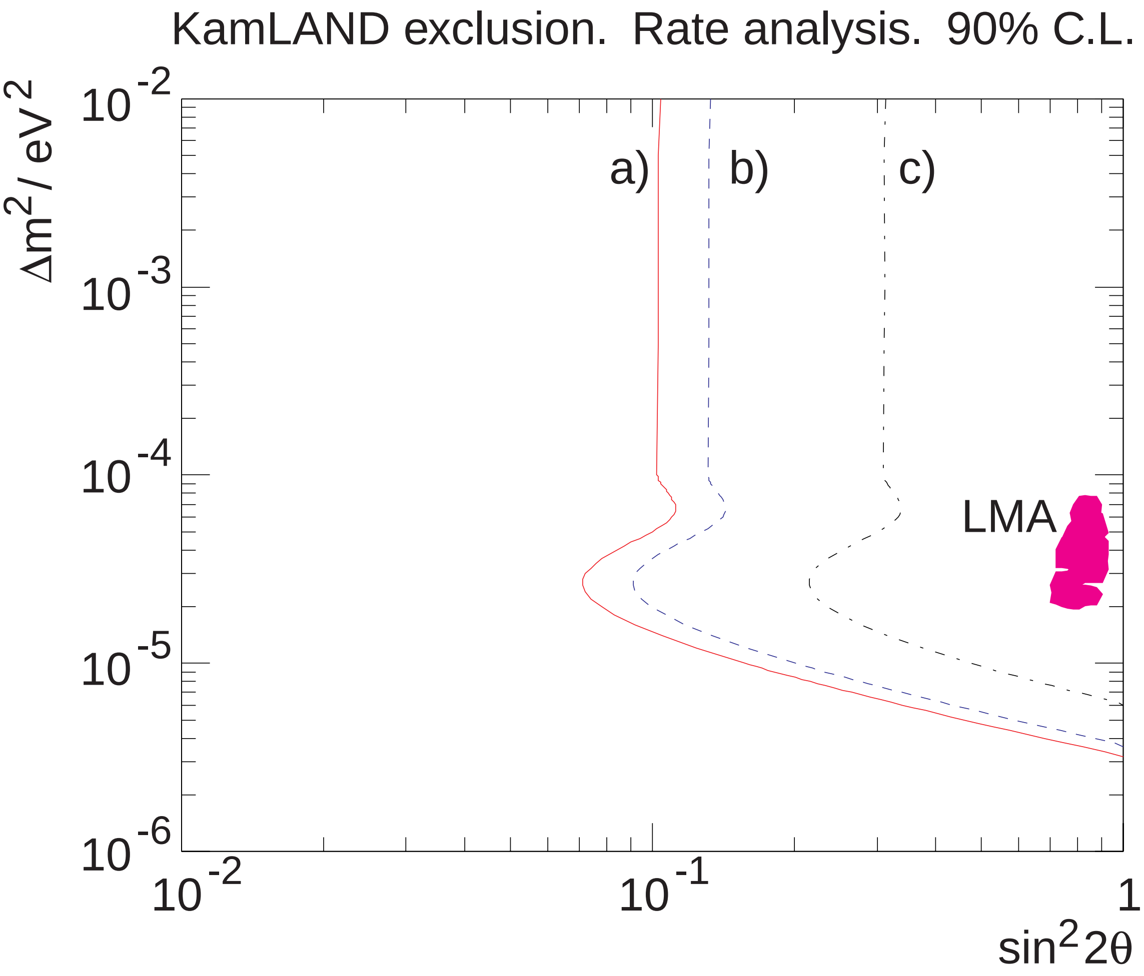

Figure 8: Sensitivity of the neutrino oscillation experiment to be performed at KamLAND. The curves represents the 90% CL sensitivity one can reach with 3 years of running with 78% of the maximum power flux. The following assumptions about the background level and its uncertainty have been made: a) ideal case; no background. b) signal-to-noise 10:1, background known to ±25%. c) signal-to-noise 10:1, background determined by subtraction through reactor on - off.

2.3 Solar neutrinos at KamLAND

The KamLAND detector can also study physics involving single ionization events, if sufficiently low backgrounds are achieved. Prominent among the topics accessible in an ultra-low background environment is the detection of solar neutrinos.

As will be shown in the next section the dominant backgrounds in such a large homogeneous detector derive from natural radioactivity internal to the scintillator, once rigorous efforts are made to select materials for the outside components. It is worth noting that a larger size detector not only gives higher signal rates, but also a better suppression of external backgrounds.

If the required radiopurity levels are reached, KamLAND and Borexino [38] will become decisive solar neutrino experiments. The KamLAND reactor neutrino study would convincingly establish or reject the large mixing angle MSW solution. KamLAND can also measure the ^{7}Be neutrino flux ($\approx$ 300 events/day in the SSM) in a reduced (600 t) fiducial volume and observe the ^{8}B neutrino spectrum to lower energies ($T \simeq 3$ MeV) than possible in Super-Kamiokande. It should be possible to determine the unique solution to the solar neutrino problem with KamLAND data alone.

The US KamLAND Collaboration proposes a co-ordinated program designed to bring the solar neutrino experiment to reality. The daunting obstacle posed by backgrounds will be attacked by suppression of radioactive contaminants, erection of barriers to radon transport, improvement of scintillator purity, and advanced electronics to discriminate against residual backgrounds.

2.3.1 Detection of Solar Neutrinos at KamLAND

Should reactor anti-neutrino oscillations be discovered by KamLAND and the oscillation parameters determined, we would like to test if the solar neutrino flux is consistent with the SSM with neutrino oscillation. This calls for an even more precise measurement of the solar neutrino flux and spectrum. Should the reactor neutrino search yield a negative result, additional measurements of the solar neutrino flux and spectrum will be needed to determine whether the missing solar neutrino flux is due to the SMA, the LOW solution, the VAC oscillations, or to other causes, e.g. problems in the SSM. Hence a measurement of the solar neutrino spectrum would, in either case, constitute a crucially important contribution by KamLAND.

Solar neutrinos interacting with the electrons in the scintillator will scatter and the resulting recoil electron can be detected via the scintillation light. The electron recoil kinetic energy T is restricted by

$$0 \leq T \leq T_{max} = \frac{2E_\nu^2}{2E_\nu + m_e} \; . \tag{9}$$

The discrete ^{7}Be spectrum would give rise to a recoil electron spectrum characterized by a sharp edge at $T_{max} = 665$ keV (see Figure 9). In order to calculate the

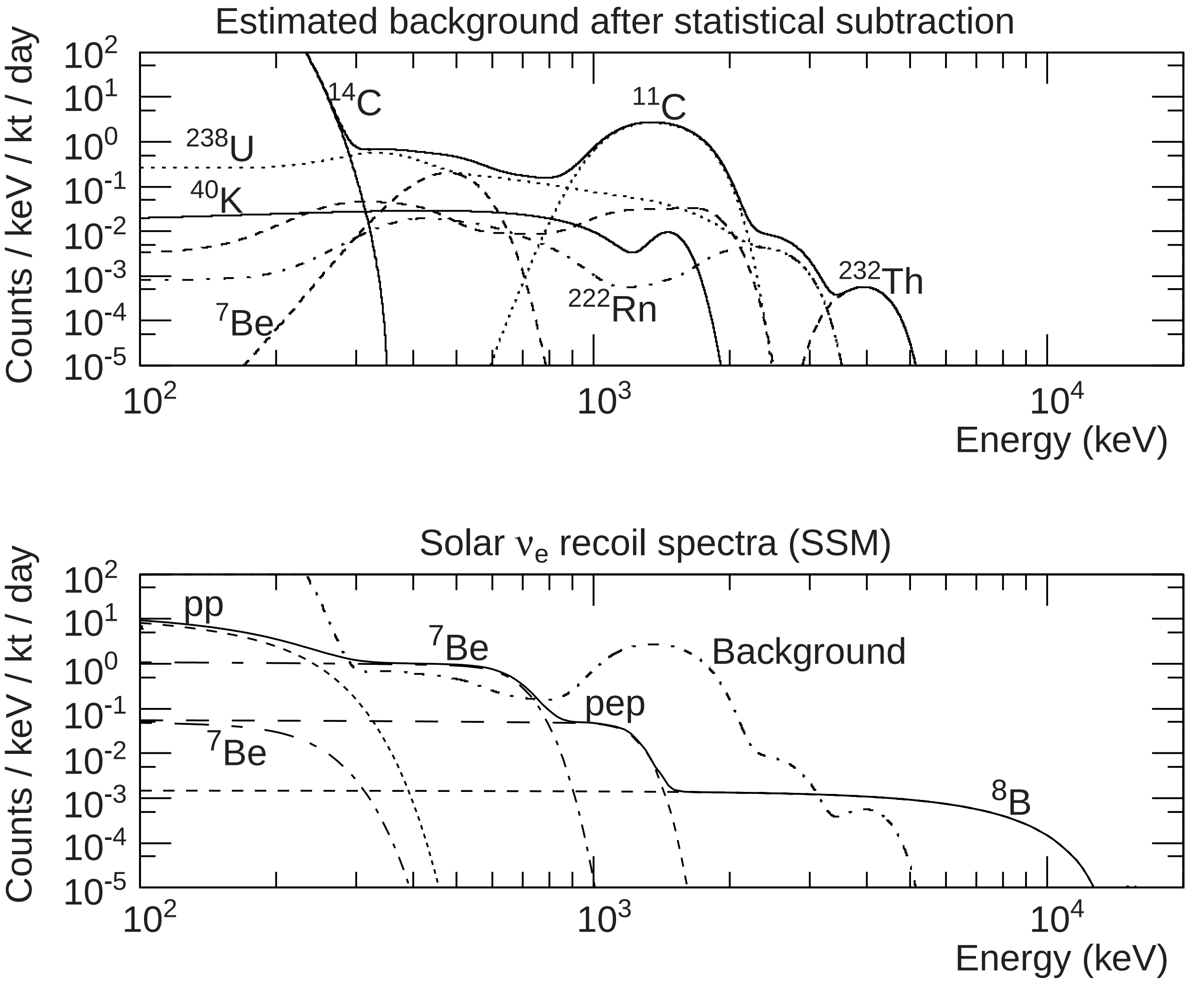

Figure 9: Signal and background for solar neutrinos in KamLAND. The upper plot depicts a decomposition of the calculated background spectrum after the "statistical subtraction" without the solar neutrino signal itself. The ^{11}C production rate is taken to be 1700/day. To reflect the large detector size, β and γ energies were added coherently. The quenched α component was added statistically. The lower plot shows the electron recoil spectrum from the most important components of the neutrino spectrum given by the SSM, together with the total background. For comparison the expected background after the "statistical subtraction" is shown. All spectra are folded with the resolution $\sigma(E)/E$=10% $/E^{1/2}$ (MeV).

total number of events, we convolve ν_e-e scattering cross section with the neutrino spectrum from the SSM [23]. The total expected rate is obtained by integrating over T and multiplying by the number of target electrons (3.4×10^{32} electrons per kt of scintillator). The result is shown in Table 4 for the most important components of the solar neutrino spectrum.

ν source	SSM flux (10^8 cm^{-2}s^{-1})	T_{max} (MeV)	events (1/kt·day)
pp	591	0.25	2033
^{7}Be	51.5	0.66	841
pep	1.4	1.22	46
^{8}B	0.066	13.7	12

Table 4: Expected rates in KamLAND for the most important components of SSM neutrino fluxes. The event rate is for all recoil electrons, with T from 0 to T_{max}. We take fiducial volume of 0.6 kt in later discussions.

As shown in Table 4 we expect a substantial solar neutrino event rate in KamLAND, much larger than the reactor neutrino rate. Since the experimental signature is simply a few hundred keV energy deposition, it is essential to reduce background from radioactivity. Further reduction of this background will be achieved by a "statistical subtraction"[3] based on tagged coincidences in the U/Th decay chains. (This method will be also employed in the Borexino experiment.)

In the following discussion the backgrounds are mostly from internal activities assuming rigorous care is taken to minimize the radioactivity of the detector components and that an appropriate fiducial volume cut is made (see Section 3.2). Low radioactive background is achieved by careful selection of materials and by arranging a large buffer region and a fiducial volume cut of 1 m from the balloon reducing the fiducial volume to 600 tons. The internal background was estimated according to the following assumptions on the radiopurity in the scintillator: U/Th 10^{-16} g/g ($1.2 \cdot 10^{-3}$ and $4.1 \cdot 10^{-4}$ Bq/kt, respectively), ^{40}K 10^{-18} g/g ($3.1 \cdot 10^{-4}$ Bq/kt), ^{14}C/^{12}C=10^{-18} (163 Bq/kt); the same assumptions as those made by the Borexino collaboration. We assume that some Rn gas diffuses through a radon barrier, bringing the Rn specific activity to 1μBq/m3 inside the balloon. (Borexino assumes no diffusion.) The cosmogenic background, which is larger at Kamioka than in the deeper Gran Sasso site, is taken into account in the estimate. It is assumed that α particles can be differentiated from electrons and photons by the pulse shape discrimination (PSD) with 90% efficiency. This efficiency has been routinely achieved in many experiments

---

[3] This method was named "statistical subtraction" by the Borexino collaboration. Note, however, that this method would not introduce an additional statistical uncertainty. This is explained below and in Section 3.2 in more detail.

including the most recent study at the Counting Test Facility of Borexino [39]. ^{214}Bi-^{214}Po pairs in ^{238}U and ^{212}Bi-^{212}Po pairs in ^{232}Th chains can be rejected using β-α coincidences ($t_{1/2} = 164\mu$sec and 0.30μsec, respectively) with 95% efficiency, which is also a reasonable expectation [40]. Once Bi-Po pairs are tagged, the radioactive decays in the U/Th chains that precede the coincidences and are in equilibrium (up to ^{222}Rn in ^{238}U and ^{224}Ra in ^{232}Th chains) must have also taken place in the detector. Therefore one can subtract the number of background events due to the preceding decays in the U/Th chains accurately from the number of observed events ("statistical subtraction"). Under these assumptions, the expected background is shown in Figure 9 (upper panel) together with the solar neutrino signal with SSM. Our choice of the analysis interval 280–800 keV for the ^{7}Be solar neutrinos is obvious: the energy threshold of 280 keV is dictated by the ^{14}C background (end point 157 keV) while 800 keV is taken above the kinematic limit of the electron recoil energy by ^{7}Be solar neutrino (665 keV). Also, one can see the relevance of the ^{208}Tl (associated with the ^{232}Th decay chain) for the detection of the ^{8}B neutrinos. Details of this analysis are given in Section 3. It cannot be overemphasized that achieving the level of radiopurity assumed here is a formidable task that is yet to be demonstrated. The Counting Test Facility (CTF) by the Borexino Collaboration achieved its design goal [39, 40, 41], but did not demonstrate the level of radio-purity required for the solar neutrino experiment. Nevertheless, for this discussion we will *assume* that a low background environment can be achieved and explore the physics that would then be accessible.

In Table 5 we list the event rate in the selected interval for the various oscillation scenarios. The background rates with and without "statistical subtraction" are also shown. To judge the significance of these rates we assume that the background can be determined independently from radio-assay (*e.g.*, neutron activation analysis) of the scintillator and components of the detector, muon spallation rate and other auxiliary measurements with an accuracy of 10% after "statistical subtraction"; it is difficult to predict the accuracy in advance, but this level of accuracy appears reasonable. Once the experiment is run for sufficient time (already after a few days) the statistical uncertainty is smaller than the assumed systematic uncertainty. While the determination of the full extent of the background at KamLAND would be quite difficult, there is another powerful method to isolate the signal: the seasonal variation.

2.3.2 Extracting the ^{7}Be signal

The solar ^{7}Be neutrino signal can be isolated from the background because it has a seasonal variation as a consequence of the eccentricity of the Earth's orbit.[4] This uniquely identifies the source of the effect as solar. The distance from the Sun to the

---

[4] If Δm^2 is in the region relevant to the VAC solution, there is an interesting seasonal modulation on top of the change of the flux due to the eccentricity of the Earth's orbit. This will be discussed later in this section.

Source	Rate (280-800 keV) [Counts/(kt day)]	
	$\nu_e \longrightarrow \nu_{\mu,\tau}$	$\nu_e \longrightarrow \nu_s$
SSM	466	
LMA	262	207
SMA	98	2
Background		
without “statistical subtraction”	438	
with “statistical subtraction”	217	

Table 5: Event rates in the energy interval 280-800 keV. ν_s denotes sterile neutrinos. We will assume 600 t fiducial volume in later discussions and the event rates are 60% of the numbers given above.

Earth varies as

$$L = L_0(1 - \epsilon \cos(2\pi t)) \tag{10}$$

where $\epsilon = 0.017$ is the orbit's eccentricity, and t is measured in years from the perihelion of the Earth, which happens to be January 1. L varies by 3.4% from minimum to maximum, and hence the flux, being proportional to $1/L^2$, as much as 6.8%. The neutrino signal, then, will have the form

$$B + S(1 + 2\epsilon \cos(2\pi t)) \tag{11}$$

With $N = B + S$ being the total number of events, the fractional uncertainty in S is thus

$$\frac{\sigma_S}{S} = \frac{1 + B/S}{\epsilon\sqrt{2N}} \tag{12}$$

Using the numbers above, $B \approx 130$ events/day after “statistical subtraction”of background, with only a 600 t fiducial volume, while for the SSM $S \approx 280$ events/day. In a year of running there would be a total of about $N = 1.5 \times 10^5$ events. The fractional uncertainty in the signal would be 0.16, while in three years it would be 0.11. Even if the solar ν_es are completely transformed into ν_μ or ν_τ, as in the SMA, they still generate neutral current events, albeit with only about 21% of the ν_e cross section. For the anticipated rates, the signal can be seen at more than 3-sigma level ($0.213 \pm 0.063\times$ the SSM rate). This would discriminate between the SMA solution, with 21% of the SSM rate and the LMA solution, with 56% of the SSM rate. Figure 10 shows such an analysis for the case of the SMA solution. No assumption has been made about energy spectrum of the background in determining the signal.

Using the seasonal modulation to extract the signal requires a thorough understanding of backgrounds, especially ones that might have a yearly modulation. Environmental radon is such a background. Knowledge of the phase of the solar signal, together with its frequency, will help greatly, but to exploit the yearly modulation large statistics are needed. KamLAND, with its unprecedented size, has a clear advantage over any other experiment.

If the seasonally varying backgrounds are successfully controlled by careful calibration (see Section5.8) then the ^{7}Be signal can be seen even if the (non-seasonally-varying) background is larger. Suppose, in particular, the backgrounds are ten times higher than anticipated. Then, considering just the statistical limitations and setting aside inevitable systematic issues, three years of running would give a 19% measurement of the SSM signal.

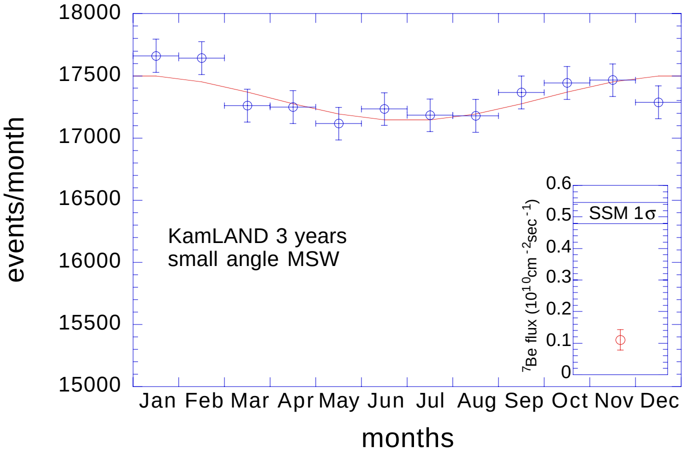

Figure 10: Measurement of the ^{7}Be solar neutrino flux from the seasonal variation. The input signal corresponds to the SMA MSW oscillation of ν_e into an active neutrino, and the background as discussed in section 2.3.1. Both the signal and the background are allowed to float in the fit to the variation due to the eccentricity of the Earth's orbit. The inset shows the extracted ^{7}Be flux from the analysis.

The seasonal variation itself can be also a useful way to find neutrino oscillations [43]. If the correct explanation of the solar neutrino problem is the VAC solution, then there are a few or a few tens of oscillations that occur between the Sun and the Earth. The 3.4% variation in the distance to the Sun will change the neutrino oscillation probability Eq. (3) as a function of seasons:

$$P(\nu_e \to \nu_e) = 1 - \sin^2 2\theta \sin^2 \left(\frac{\Delta m^2}{4.5 \times 10^{-12} \mathrm{eV}^2} - \frac{\Delta m^2}{2.7 \times 10^{-10} \mathrm{eV}^2} \cos(2\pi t) \right). \quad (13)$$

For $\Delta m^2 \lesssim 3 \times 10^{-11}$ eV^2, the effect of the eccentricity (the second term in the bracket) in P is small. However, with larger Δm^2, the second term modulates the survival probability in a non-trivial way. An example is shown in Figure 11 using parameters for the best-fit VAC solution to the existing solar neutrino flux measurements [31].

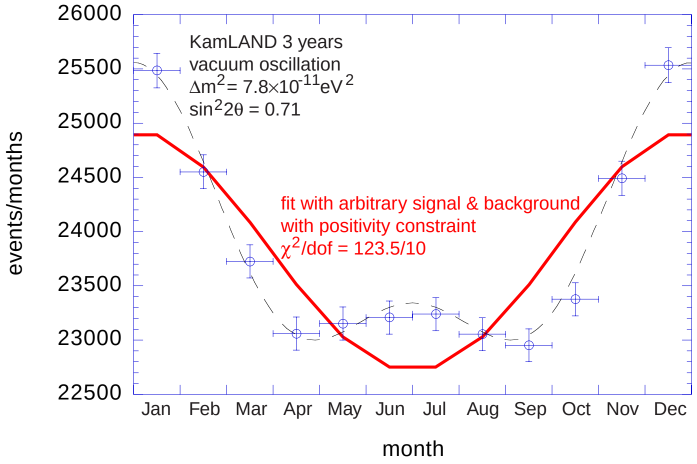

Figure 11: A simulation of data showing the seasonal variation with $\Delta m^2 = 7.8 \times 10^{-11}\text{eV}^2$ and $\sin^2 2\theta = 0.71$ corresponding to the best-fit VAC solution. The solid curve shows the best fit allowing only for the variation in flux caused by the eccentricity of the Earth's orbit and no neutrino oscillations. In this fit, both signal and background are allowed to float as long as they remain positive. For this particular parameter set, the background from the fit comes out negative; it is forced to be zero in calculating χ^2. The dashed curve shows the actual input distribution.

A fit to Eq. (11), which includes the variation in the flux of solar neutrinos, with an arbitrary signal and background levels shows a very poor χ^2. The presence of these more complex oscillations would be the signal for the VAC solution and would allow a measurement of Δm^2. The parameter region where the fit would yield a poor χ^2 at more than 95% CL (the sensitivity region) from this analysis is shown in Figure 4 (with statistical error only) [44].

Finally, KamLAND can study the possible day-night asymmetry $A = (N - D)/(N + D)$ where N (D) is the total number of events during the night (day) time. Solar neutrinos that reach the detector at night have traversed the Earth, while those reaching it in the day have not. Thus the night-observed neutrinos may experience the MSW effect while the day-observed neutrinos cannot. Statistically, the day-night asymmetry can be studied down to the permille level, but the ultimate precision is likely to be limited by systematic uncertainty. It is hard to guess what the limiting systematics will be. The current Super-Kamiokande analysis on the day-night asymmetry quotes the estimated systematic uncertainty of 0.4%. It is not unreasonable to assume that the systematics for KamLAND can be controlled to a similar level. Given S/B of about 1 (which can be determined from the seasonal variation), such a measurement would place a 95% CL limit on the up-down asymmetry of about 1%, and would exclude the LOW solution (see [45] and Figure 4).

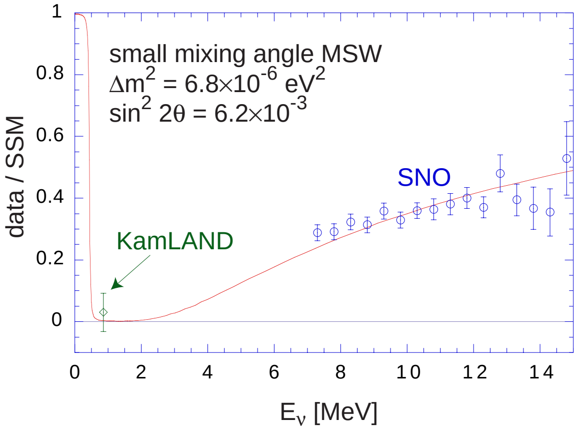

Figure 12: The energy spectrum distortion in the solar neutrinos for the SMA solution. The points above 6 MeV are from the SNO experiment (1 year), while the point at 0.862 MeV is from KamLAND. The case of $\nu_e \to \nu_s$ oscillation is shown for the purpose of illustration. The normalization of the points from SNO has an overall uncertainty of about 15% due to the uncertainty in the theoretical prediction of the solar ^{8}B neutrino flux, while that on ^{7}Be neutrino is about 9% [46].

Combining three capabilities of KamLAND, namely the reactor neutrino experiment, sensitivity to day-night asymmetry and seasonal variation of solar ^{7}Be neutrinos, KamLAND could cover a large range of Δm^2 independent of the solar model (Fig. 4). Given the possibility of studying ^{7}Be neutrinos from the Sun, the potential impact of KamLAND on the neutrino oscillation in general and more specifically on the solar neutrino problem is compelling. In particular, KamLAND is capable of discriminating between the four presently favored solutions to the solar neutrino problem. This argument is summarized qualitatively in Tables 6 and 7.

KamLAND may also extend the range of observation of the ^{8}B neutrinos. As stressed above and shown in Fig. 9, between 3 and 5 MeV the background is expected to be dominated by the ^{208}Tl decay which can be removed statistically with good accuracy, and possibly on an event-by-event basis. Then it would be possible to measure the ^{8}B electron recoil spectrum down to about 3 MeV. In KamLAND's 600 tons fiducial volume one would expect about 4 events per day (assuming 100% efficiency) from the SSM, or 2 events/day with 0.5 reduction as determined by Super-Kamiokande. Moreover, this is a new window in the ^{8}B neutrino spectrum extending the capabilities of Super-Kamiokande and SNO. The observation of ^{8}B neutrino would also facilitate the comparison of results from KamLAND to other experiments, providing valuable confirmation of potentially important scientific conclusions.

Active ν with:	KamLAND	SNO
SMA	low but finite ^{7}Be rate	NC/CC high E_{ν_e} spectrum distortion
LMA	low rate in reactor experiment	NC/CC high
VAC	unusual seasonal variation in ^{7}Be	NC/CC high
LOW	day-night effect in ^{7}Be rate	NC/CC high

Table 6: The capabilities of both KamLAND and SNO for the four solutions to the solar neutrino problem for oscillations to active neutrinos (ν_μ or ν_τ). KamLAND not only sees effects, but sees different effects in each case. SNO will see an excess in all cases in the neutral-current to charged-current (NC/CC) ratio due to ν_μ or ν_τ, and may also see day-night effect for a small portion of the LMA solution parameter space and spectrum distortion for a large portion of the VAC solution parameter space, but may not fully distinguish between the LMA, VAC and LOW solutions.

Sterile ν with:	KamLAND	SNO
SMA	low or vanishing ^{7}Be rate	E_{ν_e} spectrum distortion
LMA	low rate in reactor experiment	
VAC	unusual seasonal variation in ^{7}Be	
LOW	day-night effect in ^{7}Be rate	

Table 7: The capabilities of both KamLAND and SNO for the four solutions to the solar neutrino problem when the oscillations are to sterile neutrinos. KamLAND not only sees effects, but sees different effects in each case. SNO does not see a signal for any cases in the NC/CC ratio, but may see day-night effect for a small portion of the LMA solution parameter space and spectrum distortion for a large portion of the VAC solution parameter space, yet may not fully distinguish between the LMA, VAC and LOW solutions.

2.3.3 Competing Experiments

The existing radio-chemical experiments have only a limited sensitivity for ^{7}Be neutrinos. Their inclusive flux measurements do not allow separation of the contributions of the different solar neutrino species. Since the Cl and Ga experiments have different reaction threshold energies and hence different contributions from various neutrino species there is a strong constraint on the allowed ^{7}Be flux as explained above. Super-Kamiokande and SNO [42] are only sensitive to the energetic ^{8}B neutrinos. KamLAND has the opportunity of extending the range of electron recoil energies down to about 3 MeV.

The Borexino experiment [38], being built in the Italian Gran Sasso laboratory, also plans to measure the ^{7}Be solar neutrino flux via neutrino electron scattering using a liquid scintillator. Borexino expects to begin data-taking in 2001 with a fiducial volume of 100t. The Borexino collaboration has pioneered the field of large volume ultra-low background scintillation detectors [41]. KamLAND is a natural extension of that effort. We expect to provide valuable and independent information on the ^{7}Be solar neutrino flux on a time scale similar to Borexino. The main advantage of KamLAND over Borexino as a solar neutrino experiment, assuming radiopurity requirements are met, is that KamLAND is significantly larger.

2.4 Other Physics Opportunities with KamLAND

KamLAND can address other scientific questions in addition to possible reactor neutrino oscillations and the solar neutrino problem. While these other questions are both interesting and potentially very important, they are secondary goals. Some are discussed in Appendix 6.

Nevertheless, it is worth recalling that the past underground detectors made important contributions in totally unexpected areas. For example, Kamiokande was originally conceived as a proton-decay experiment (sub-GeV energy). It failed to discover proton decay, but it was later improved to study both solar (about 10 MeV energy) and atmospheric neutrinos (sub-GeV and multi-GeV energies), due in part to the activities of the US participants. Kamiokande convincingly demonstrated that neutrinos are coming from the Sun, and that there is an anomaly in atmospheric neutrinos both in the flavor ratio and the zenith angle dependence. It provided important information about ^{8}B solar neutrinos, providing hints for the MSW effect in the Sun. It furthermore detected neutrinos from the SN1987A which was the first observation of neutrinos from outside our solar system. There is a good reason to believe that extending the reach down to MeV and sub-MeV energies with KamLAND will open up other new frontiers in areas that have not yet been anticipated. Appendix 6 contains several additional scientific questions of significance that may be addressed by KamLAND.

3 Backgrounds

Backgrounds for physics measurements at KamLAND are produced by cosmic-muon-induced processes and natural radioactivity. Two signatures are of interest for KamLAND: double events and single events.

- Double events are typical for anti-neutrino detection. The signature for reactor anti-neutrinos consists of a prompt part for the positron and a delayed part for neutron capture. We require a minimum 1-MeV energy deposit for the prompt part and $1.8 - 2.7$ MeV energy deposit for the delayed part (a 3-σ cut for the 2.2-MeV neutron capture signal). We require a delay of $10-500$ μs. In addition, the neutron capture is required to be within 1 m of the vertex of the positron. The Monte Carlo simulation shows that, given the small kinetic energy of these neutrons ($<$ 100 keV), such a cut retains more than 99% of signal events.
- Singles events, for instance from low-energy neutrino scattering on electrons, are selected by only requiring a minimum energy deposition of 280 keV. To reduce the background from radioactive sources at the periphery, like the PMTs and surrounding rock, a fiducial volume will be defined to include only the innermost 0.6 kt of the scintillator detector. This will be achieved by reconstructing off-line the position of the events inside the scintillator.

In the following we shall analyze in detail the absolute values and relative importance of different backgrounds.

3.1 Background from Cosmic Ray Events

KamLAND is shielded from cosmic radiation by 2700 mwe of rock. The total muon rate measured by the full Kamiokande detector, where KamLAND will be situated, was 0.37 Hz[47]. The energy distribution of muons is expected to be flat from 0-100 GeV and then to drop exponentially [48]. The angular variation should be well approximated by a $\cos^2\theta$ distribution. Under these conditions we expect muon rates of 0.21 Hz in the scintillator and 0.15 Hz in the solar neutrino (0.60 kton) fiducial volume. The muon rate in a 1 m thick rock shell will be 0.85 Hz, of which 0.15 Hz will not be detected by the veto.

When a muon traverses the veto detector, events within the subsequent 50 ms window will be vetoed, but that veto need only be applied in the region around the muon. Similarly, all muons traversing the central detector will result in a 250 ms veto, again restricted to the proximity of the muon. Using a conservative veto volume of 10% of the detector volume we easily obtain dead-times of, respectively, 0.3% and 0.5% for the two types of events. In this way we will essentially remove all background from pion and muon decay, and short-half-life induced radioactivity, with negligible impact on the detector's efficiency.

Given the above veto condition, cosmic ray muons can generate background only through spallation. This happens in two ways:

- in the rock outside of the KamLAND detector, generating an energetic neutron that could pass undetected through the veto detector and generate a background event in the central detector.
- in the central detector, resulting in radioactive nuclei with lifetimes of order 100 ms or greater.

For this second class of events the decay may happen well after the cosmic ray occurrence. Which of these events can be rejected will depend on the lifetimes and on the details of scintillation and mass transport. Further rejection could rely only on detailed analysis of the event shape and energy. For this reason we will describe cosmogenic radioactivity separately from the prompt neutrons. It is very important to realize that cosmogenic activation never results in a background for the reactor experiment, which has a delayed-correlation signal. At the same time, it is one of the most important backgrounds for the solar neutrino experiment, whose signal is due to a single electron. Clearly, electronics able to extract all the time and amplitude information from the detector will be as essential as extreme cleanliness in obtaining robust results from KamLAND.

3.1.1 Background from Prompt Neutrons

Although there are two different neutron-generating processes, muon capture and muon spallation, neutrons from the second process are more energetic and hence more dangerous. Therefore in the following study we concentrate only on the background from muon spallation. We only consider neutrons produced in a shell of rock of 1 m thickness, since muons in the detector are vetoed and neutron produced deeper than 1 m get absorbed. This corresponds to a total active volume of 1.9×10^{9} cm^{3}. Neutrons production by muons has been measured by several underground experiments [49]. Using their measurements the neutron yield for each muon at 2700 mwe is $4\times10^{-4}\text{g}^{-1}\cdot$ cm^{2}. Using a rock density of 2.7 g/cm^{3}, we can then calculate that 6000 n/day are produced (untagged) in the surrounding rock.

Since the energy spectrum of these neutrons is not well understood we conservatively assume that all neutrons have a hard spectrum. This gives a power-law behavior that can be fitted to $E_{\mathrm{n}}^{-1.86}$ as measured by several experiments [50]. The angular distribution is obtained from [51].

Using all the information above, we generated half a million neutron background events in our detector (corresponding to about 80 days of data-taking).

By requiring an energy deposition of at least 0.3 MeV only 2 events/day are retained in the 600-t fiducial region. This background for singles is negligible compared to the natural radioactivity background described below. For double correlated events, where the threshold is 1 MeV and the full 1-kt detector is used, we apply the

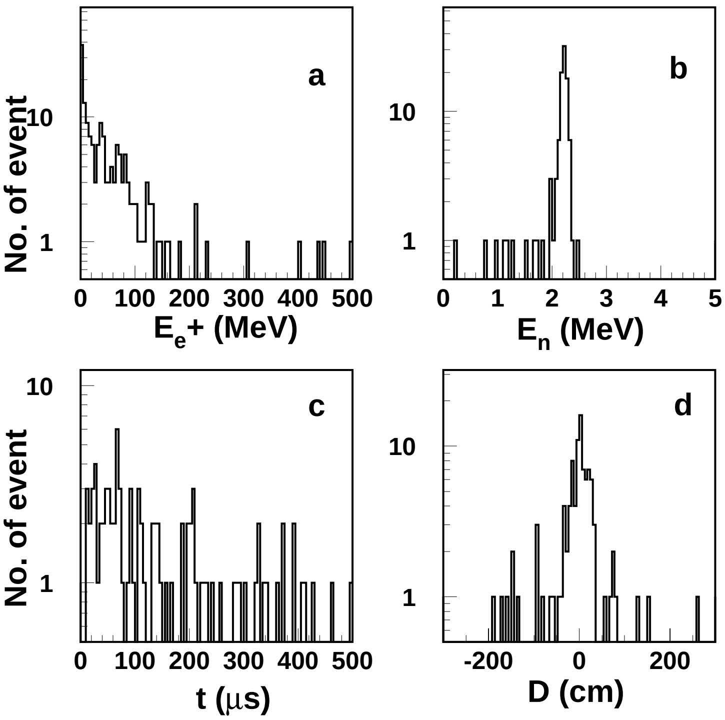

Figure 13: Simulation of cosmic muon-induced fast neutron in KamLAND. a: Energy distribution of the prompt part (fake positron); b: Energy distribution of the delayed part (neutron capture); c: time difference between prompt and delayed part; d: vertex difference between prompt and delays part.

cuts described above and retain only < 0.05 events/day, with a signature consistent with anti-neutrinos. This is to be compared to 2 events/day of signal from the reactors. In Figure 13 we show, as an example, some of the variables of interest for the neutron background suppression for correlated event signatures. Only pairs of events with energy in both the prompt and the delayed parts are plotted.

We conclude that signals from cosmic-ray induced neutrons do not limit the ability to do physics at KamLAND.

3.1.2 Background from Cosmogenic Activation

Nuclei in the scintillator materials can be excited by capturing a muon/neutron, or through muon/neutron spallation. The excited nucleus will quickly ($<$ ns) de-excite by emitting γ, neutron, proton or α, plus another nucleus, which could be a radioactive isotope with lifetime from milliseconds to years. Only if the lifetime is short enough can the event be rejected by the cosmic ray veto. In our study we will assume the scintillator composition given below (80% isoparaffin ($\simeq$ nCH_2), 20% pseudocumene (C_9H_{12}) and 2g/l PPO ($C_{15}H_{11}NO$)). Since the mass of ^{14}N and ^{16}O is only 0.02% of that of the proton and carbon, we will neglect them in the following discussions.

Calculating now the neutron production inside the detector, we obtain a rate of 5000 n/day in the 1-kt detector and 3000 n/day inside the 600-t fiducial volume. In the following we will use this number to estimate the number of isotope-producing processes. It is easy to see that cosmogenic activation gives a negligible contribution to the background to the reactor experiment, which has a correlated signature, and thus we concentrate on backgrounds to solar neutrino experiment.

- *Activation by muon spallation:*

  The process that initiates the neutron production is spallation by cosmic-ray muons. The main reactions from muon spallation are $^{12}C + \gamma \rightarrow n +^{11} C$, $^{12}C+\gamma \rightarrow 2n+^{10}C$, $^{12}C+\gamma \rightarrow p+^{11}B$, $^{12}C+\gamma \rightarrow np+^{10}B$ and $^{13}C+\gamma \rightarrow n+^{12}C$ where the γ is a virtual photon emitted by the muon. Of all the final states only ^{10}C and ^{11}C give origin to problematic decays. Although a precise calculation for the rate of production of these isotopes is cannot be achieved, we can easily compute an extreme upper limit by conservatively assuming that every neutron created in the detector is associated with the production of the two dangerous isotopes. We then obtain a rate of ^{10}C and ^{11}C production of < 1800 day^{-1}. It is likely that the relatively short-lived (19.3 s) ^{10}C will be suppressed off-line by an extended veto for small regions of the detector. The actual ^{11}C production by muon spallation is likely to be rather less than this, as discussed below.

- *Activation by neutron spallation:*

  Neutron spallation can produce many radioactive isotopes according to the reaction $N + n \rightarrow h + N'$ where h can be a neutron, proton, γ, α or π. While the

Isotopes	Lifetime (s)	cross section (mb)	No. day^{-1}	background day^{-1}
^{12}B	0.02	30 [56]	< 1700	< 1700
^{11}C	1218	28.7 [55]	< 1700	< 1700
^{10}C	19.3	1.1 [55]	< 65	< 65
^{10}Be	1.5×10^6 y	2.5 [55]	<150	0
^{7}Be	53.28 d	7.1 [55]	<409	<40

Table 8: Monte Carlo results for neutron spallation on ^{12}C, giving rise to particular nuclides. The upper limits should be regarded as representing approximately the relative proportions of the varies species produced.

prompt production of h is well described by intra-nuclear cascade plus evaporation models [54], which have been incorporated in FLUKA, more important to us is the understanding of the nuclear component N$'$ that is not theoretically well understood. To study these cases of activation we use the production cross sections measured in[55]. The results are displayed in Table 8.

The results of the Monte Carlos can be anticipated from the displayed cross sections. The dominantly produced species are ^{12}B, ^{11}C, and ^{7}Be. The first of these has a lifetime of 20 ms and can be vetoed. The last is produced in negligible amounts compared to the total ^{7}Be content of the detector. The production of ^{11}C is already effectively taken into account in our conservative estimate for muon spallation where it was assumed that every produced neutron left a ^{11}C nucleus behind.

- *Activation by neutron capture*

  Most of neutrons capture on protons and, to a lesser extent on ^{12}C resulting in stable isotopes (^{2}H and ^{13}C). A very small fraction of them are captured on ^{13}C (about 1% of natural carbon), giving the radioactive ^{14}C, but in numbers insignificant compared to the 10^{13} nuclei of ^{14}C already present in the scintillator. From extensive studies conducted by the Borexino-collaboration[57] it is known that activation of ^{13}C during the scintillator production does not result in dangerous backgrounds.

- *Activation by muon capture:*

  The muon capture reactions $\mu + (A, Z) \longrightarrow \nu_\mu + (A, Z-1)^*$ produce excited nuclei $(A, Z-1)^*$, which then de-excite into radioactive isotopes. The only final state isotopes that can be produced inside KamLAND are ^{12}B and ^{13}B. Both these isotopes can be vetoed given their rather short half-life ($\simeq$ 20 ms). Our calculation shows that even with no veto the background rate does not exceed

1 day^{-1} in 600 tons of scintillator.

While these simple estimates show that the backgrounds from muon and neutron spallation may be important for the solar neutrino detection, it should be remarked that such estimates are pessimistic. In fact, there is good reason to believe that most of the neutrons result not from muon spallation, or even from neutron spallation subsequent to the original muon collision, but from the collision of pions with nuclei [52]. These pions are part of the shower initiated by the incident muon. Negative pions, in particular, through their collisions or capture will be a copious source of neutrons. Many of these neutron-production events will leave behind nuclei that are not important sources of background.

In fact, measurements by the Borexino Collaboration [53] indicate that the figure for KamLAND is likely to be around 1400 ^{11}C created per day in the 1-kt scintillator volume.

3.2 Background from Natural Radioactivity

There are three possible sources of background due to natural radioactivity:

- decay chains of the long lived ^{238}U, ^{232}Th and ^{40}K naturally present in small amounts in rocks surrounding the detector and material used in the detector construction;
- decay of ^{60}Co artificially added to steel during production for quality monitoring purposes;
- decay of ^{222}Rn continuously produced in the disintegration of ^{238}U contained in rocks and detector materials. Since the radon readily diffuses into many materials and has a lifetime of a few days, it effectively acts as a carrier that disperses the radioactivity through the entire detector unless special precautions are taken.

3.2.1 Monte Carlo study of radioactive background

In order to study these backgrounds, we have modeled the complete decay chains of these isotopes, derived from [59], in our Monte Carlo program as shown in Tables 16-19 of Appendix 7. ^{222}Rn is part of the ^{238}U chain and it is not listed separately. We have performed a full simulation using GEANT [60] for the detector geometry, materials and the electromagnetic interactions between particles and the detector materials; FLUKA [61] for hadronic interactions and GCALOR [62] for low energy neutron transport.

For simplicity we explicitly considered only those decays with branching ratios greater than 0.5%, while the remaining modes have been lumped together in a fictitious mode marked with *. This mode has been assigned conservatively equal energy

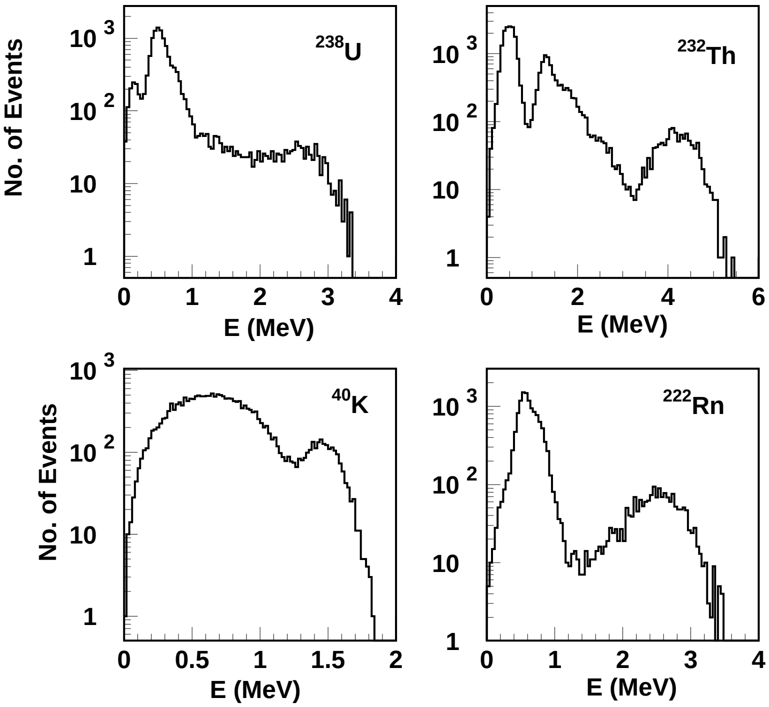

Figure 14: Energy spectra resulting from our Monte Carlo simulation of the decay chains from different isotopes distributed in the scintillator.

sharing among β-decay and a single γ line, resulting in relatively large energy γs in the detector. Finally in β-decays only the three-body kinematics are simulated, disregarding modifications of the energy spectra and angular correlations due to matrix elements and coulomb corrections. Particles are then tracked by GEANT and when energy is deposited in the scintillator resolution functions for the energy and position are applied. In addition α absorption is "quenched" by multiplying the light emitted by a quenching factor $q = 0.1$. This is a conservative assumption since we have measure the quenching factor of our scintillator to be 0.07 (see Section 5.4). Energy depositions in a time window of $1\mu s$ are added together. The resulting energy spectra for the case of some important isotopes distributed in the scintillator are shown in Figure 14. ^{60}Co is not shown since it is not expected to be present in the bulk scintillator and has a trivial spectrum, while we explicitly show the ^{222}Rn spectrum since, as previously noted, Rn will have a distribution largely independent from the U sources.

Isotope	$T_{1/2}$ (yr)	Natural Abundance	Activity (Bq/g)	No. of Decays in chain
^{238}U	4.47×10^9	0.993	12344	10
^{232}Th	1.41×10^{10}	1.000	4044	6
^{40}K	1.28×10^9	1.17×10^{-4}	2.5×10^5	1
^{222}Rn	3.8 day	0	5.7×10^{15}	5
^{60}Co	5.3	0	4.2×10^{13}	1

Table 9: Summary of decay parameters for the five main isotopes considered in the simulation. Only decays with $T_{1/2} > 500$ s are individually counted, while decays with shorter $T_{1/2}$ are combined with their mother as cascade. As already mentioned decays with total energy less than 100 keV are excluded. The specific activity in column 4 refers to the radioactive isotope listed only.

Finally, to transform these distributions into a background estimate we need to assign the appropriate isotope concentrations to the different materials in the detector. In Table 9 we summarize the decay properties of the isotopes considered. Nuclear data for the five main isotopes used in the simulation are given in in Appendix 7. In counting the number of decays or the number of daughters, those with $T_{1/2} < 500$ s are combined with their mother as cascade, therefore not counted. Those decays with total energy less than 100 keV are excluded.

It is clear that, while the very large volume of our detector gives us a tremendous shielding factor towards external radioactivity, radon can still travel inside KamLAND carried by the liquids in which it easily dissolves. Therefore the detector will be equipped with barriers designed, among other things, to confine the radon outside the fiducial volume. Radon emanation rates in the same type of glass used for the KamLAND photomultipliers have been measured by the SuperKamiokande collaboration [63]. The radon specific activity in the buffer volume can then be estimated to be 10 mBq/m^3. For the purpose of background simulation we assume that one barrier film is present (balloon) with a permeability coefficient for radon of 10 cm^3 mm m^{-2} day^{-1} atm. This figure, which can be achieved with properly engineered nylon films, reduces the specific radon activity in the active volume to 1 μBq/m^3. The use of two barriers or a more impermeable film is under study.

The result of the simulation of several millions of events is shown in Table 10 together with the expected contaminations of the different parts of the detector. Contaminations in the steel are obtained from measurements of KamLAND samples from the Mitsui Company. In the case of the rock surrounding the detector we use measured activities of the worst rocks sampled from the KamLAND cavity. The contamination figures for the glass are obtained by direct measurements on prototype Hamamatsu tubes.

For the scintillator we use a contamination of 10^{-16} g/g, similar to what has been planned by the Borexino Collaboration.

Material	Mass (tons)	Isotope	Purity (ppb)	bkgd. in 1.0 kt (Hz)	bkgd in 0.6 kt (Hz)
Scint.	1000	^{238}U	10^{-7}	0.003	0.002
		^{232}Th	10^{-7}	0.001	0.0005
		^{40}K	10^{-7}	0.004	0.002
		^{222}Rn	1 μBq/m^3	0.002	0.001
Buffer Oil	1523	^{238}U	10^{-5}	0.003	0.0
		^{232}Th	10^{-5}	0.001	0.0
		^{40}K	10^{-5}	0.009	0.0
		^{222}Rn	10 mBq/m^3	0.030	0.0
Steel Tank	31	^{238}U	1	0.001	0.0
		^{232}Th	1	0.004	0.0
		^{40}K	1	0.010	0.0
		^{60}Co	10^{-9}	0.005	0.0
PMT	7.2	^{238}U	400	0.503	0.003
		^{232}Th	300	0.137	0.0004
		^{40}K	180	0.046	0.0002
Rock	627	^{238}U	73000	0.199	0.001
		^{232}Th	200000	0.059	0.002
		^{40}K	4600	0	0
Total				1.02	<0.012

Table 10: Single rates above 1 MeV for all materials and radon. The rates for the solar neutrino experiment, where the threshold is 280 keV, would be higher.

In Table 11 we summarize the signal and background situation for the reactor

Backgrounds for doubles	day^{-1}
Neutrons produced by cosmic rays	0.05
Natural radioactivity (random coincidence)	0.05
Natural radioactivity (correlated)	0.00
Anti-neutrino signal (no oscillations)	2.2

Table 11: Summary of background rates and signal for correlated events in 1-kt (reactor anti-neutrino measurements).

oscillation measurements and a 1 kton active volume. A 10^{-14}g/g U and Th concentration in the scintillator would increase the "random coincidence" contribution to 0.15 day^{-1}. Our conclusion is that, while the reactor measurements will be possible even with a more conservative level of purity, the possibility of reaching 10^{-16}g/g will substantially increase the reliability of the measurements.

From a cursory inspection of Table 10 it is clear that in order to gain access to a clean solar neutrino measurement several requirements need to be met:

- The internal contamination of the scintillator has to be at the level of 10^{-16}g/g for U, Th and K;
- The fiducial volume has to be reduced in order to provide extra shielding from external radioactivity;
- Once the fiducial volume is reduced to 600 tons the background is dominated by internal (secular and cosmogenic) activity. Proper use of time correlations allow further background subtraction (event-by-event and statistically).

3.2.2 Subtraction of observed decay chains

The most crucial U/Th and Rn background contribution can be determined through Bi-Po $\alpha - \beta$ coincidences. In case of U/Rn the ^{214}Bi β-decay is quickly followed by the ^{214}Po α-decay ($T_{1/2} = 162\mu$s). The ^{212}Bi-^{212}Po pair in the Th decay series has a correlation time of $T_{1/2} = 0.30\mu$s. A tagged background sample would also give the measured spectral shape of these components. We assume that the tagging has 95% efficiency and thus removes the ^{214}Bi β and γ, and the corresponding ^{214}Po α on the event-by-event basis. Similarly, the pair of decays ^{212}Bi, ^{212}Po $\beta + \gamma$ and α will be also identified and removed event-by-event.

Moreover, since the correlated Bi-Po rates will be accurately known, other decays which are necessarily in equilibrium with them can be accurately subtracted (so-called "statistical subtraction"). In the U/Rn chain this set contains the ^{222}Rn, ^{218}Po α and the ^{214}Pb $\beta + \gamma$. In the Th chain the subtraction involves ^{224}Ra, ^{220}Rn, ^{216}Po and ^{212}Bi α and ^{212}Pb and ^{208}Tl $\beta + \gamma$. The shape of these decays can be independently determined. The remaining decays in these chains involve long lived activities that are not necessarily in equilibrium.

The ^{208}Tl decays are the most important, in fact the only, background relevant for the identification of the recoil electron scattered by the solar ^{8}B neutrinos for $T \geq 3$ MeV. The ^{208}Tl betas and gammas extend up to 5 MeV. As pointed out above, they can be efficiently removed statistically. Moreover, the lifetime of ^{208}Tl is only 4.5 minutes, and is preceded by the ^{212}Bi alpha decay. Further studies of the mass transport properties of the scintillator are needed to see if the α/β correlation method can be extended to such long time intervals. If the corresponding vertices are less than 2 meters apart after $\simeq$ 10 minutes, the correlated events can be removed event-by-event.

Finally, as explained elsewhere, we assume that α particles can be separated from the electrons and photons by the pulse shape discrimination (PSD). In making the background estimates we assume that the PSD will be 90% efficient.

The in situ background determination will be complemented by a high sensitivity neutron activation analysis (NAA) to test for a broken secular equilibrium. The analysis of the spectral shape at higher energies would constrain this determination by normalizing a Monte Carlo background model. The ^{40}K activity would also be determined through NAA. The ^{7}Be production rate would be determined independently e.g. by exposing scintillator to an energetic muon beam.

Using all of the above assumptions we present in Table 12 the individual components of the background in the energy interval 280-800 keV . In this interval the signal will be dominated by the solar ^{7}Be. The lower edge of that interval is determined by the ^{14}C contamination as shown in Figure 9.

3.3 Background Summary

The background to the reactor $\bar{\nu}_e$ signal is dominated by random coincidences of natural radioactivity and correlated signals from neutrons produced by muon spallation in the rock. A scintillator purity of 10^{-16} g/g in U, Th and K helps reducing the (first) background and hence to make the measurement more reliable.

For the solar neutrino experiment the cosmogenic ^{11}C and the internal U/Th activity of the scintillator (at 10^{-16} g/g) dominate the backgrounds. The rejection of these backgrounds calls for a high quality detector capable of the best possible energy and time resolution. While the measurement of the ^{7}Be line of solar neutrinos is very challenging, KamLAND with its unprecedented size and statistical power, full photocathode coverage and advanced electronics will be in the best position to perform conclusive measurements.

Source	Isotope	Total rate (day^{-1})	Rate with PSD and α/β corr. (day^{-1})	Rate with PSD, α/β and Stat. Subtr. (day^{-1})
U $\beta+\gamma$	^{234}Pa	39.3	39.3	39.3
	^{214}Pb	90.5	90.5	4.5
	^{214}Bi	4.4	0.2	0.2
	^{210}Bi	46.8	46.8	46.8
α	all	755.8	46.6	46.6
Rn $\beta+\gamma$	^{214}Pb	91.3	91.3	4.6
	^{214}Bi	4.4	0.2	0.2
α	all	318.6	26.5	1.6
Th $\beta+\gamma$	^{228}Ac	3.3	3.3	3.3
	^{212}Pb	23.1	23.1	1.2
	^{212}Bi	9.8	0.5	0.5
	^{208}Tl	0	0	0
α	all	191.2	6.5	6.2
K $\beta+\gamma$	^{40}K	14	14	14
Cosmogenic	^{14}C	13	13	13
	^{11}C	0.6	0.6	0.6
	^{7}Be	35	35	35
total		2463	438	217

Table 12: Internal background estimates (events/kt day). Internal contamination assumptions are listed in the text. The energy interval 280-800 keV is used. In column 3 the rates are total rates without corrections, in column 4 after the PSD and α/β correlation elimination, and in column 5 after the statistical subtraction using the Bi-Po pairs. The Bi-Po pairs used in the statistical subtraction can be determined to the relative accuracy of ±0.7% for U and Rn, and ±1.5% for Th.

4 The Site

The KamLAND detector will be sited in the Kamiokande detector cavity under the summit of Mt. Ikenoyama in the Japanese Alps. The site is within 50 km of the town of Toyama. The rock overburden in any direction is more than 1,000 meters. With an average rock density of 2.7 g/cm^3 the minimum surface energy required for a muon to reach the detector is 1.3 TeV. This overburden provides a well-studied cosmic-ray muon attenuation factor of 10^5 with respect to the surface flux of 130 m^{-2} s^{-1}.

The KamLAND detector will be 500 meters from the SuperKamiokande detector currently operating under the same mountain. The detector location inside Mt. Ikenoyama and its position relative to SuperKamiokande are shown in Figure 15.

For nearly two decades the detectors operated under Mt. Ikenoyama have been used extensively for cosmic-ray research. These experiments present the KamLAND collaboration with a mature underground infrastructure and good working relationship with the mining company. The recent international conference, Neutrino 98, has further bolstered the excellent relationship between the scientific community working there and the local communities. These are all the more important since there is no local accelerator to host the effort.

Starting in March 1998 the Kamiokande cavity has been drained and the Kamiokande detector dismantled in preparation for KamLAND. The cavity was enlarged to accommodate the new detector geometry and to provide additional shielding. Access to the KamLAND site (shown in Figure 16) is possible through a smaller railroad tunnel from the Mozumi entrance or through a newer, enlarged tunnel accessing the SuperKamiokande site from the Atotsu mine entrance. The Atotsu entrance has been extended to the KamLAND site by enlarging one of the smaller tunnels previously existing between the two laboratory sites.

As shown in Figure 16 at least four enlarged drifts will be provided along the access tunnels to accommodate the anticipated counting facilities, scintillator and water purification plants and processing equipment and the electrical sub-station. Special fireproof doors will seal the experiment from the rest of the mine during critical scintillator processing. A mechanical ventilation system will assist natural ventilation (used by Kamiokande and SuperKamiokande) in order to guarantee safe conditions for scintillator handling. These special ventilation systems using external air intakes will also reduce air-borne radioactivity during detector construction and operation phases by providing filtered and low radon content air. To reduce radioactive backgrounds the experiment will install radon barriers by treating the detector cavity and experimental area walls with a special impermeable polyurethane coating already used by the SuperKamiokande and Sudbury Neutrino Observatory (SNO) experiments. KamLAND is investigating installing additional background reduction measures based on clean room technologies successfully employed by SNO.

A new 3-kV line will be brought to the KamLAND electrical sub-station. Both 110 V and 220 V will be distributed through the detector site.

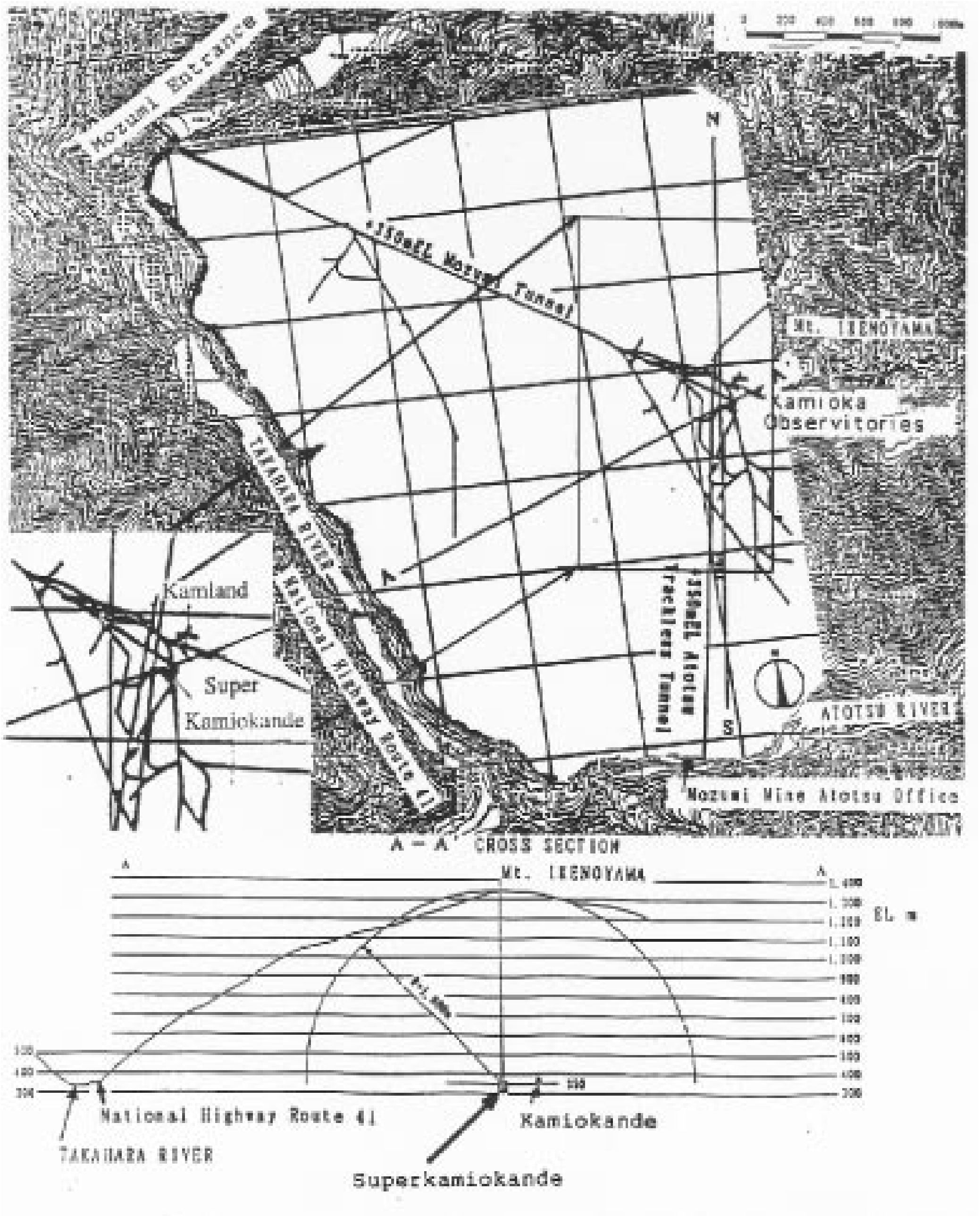

Figure 15: Partial view of the system of tunnels inside Mount Ikenoyama with the locations of KamLAND and SuperKamiokande. The Atotsu tunnel is a large road tunnel accessible to regular size trucks. A profile of the mountain along the direction of smallest extent is also shown.

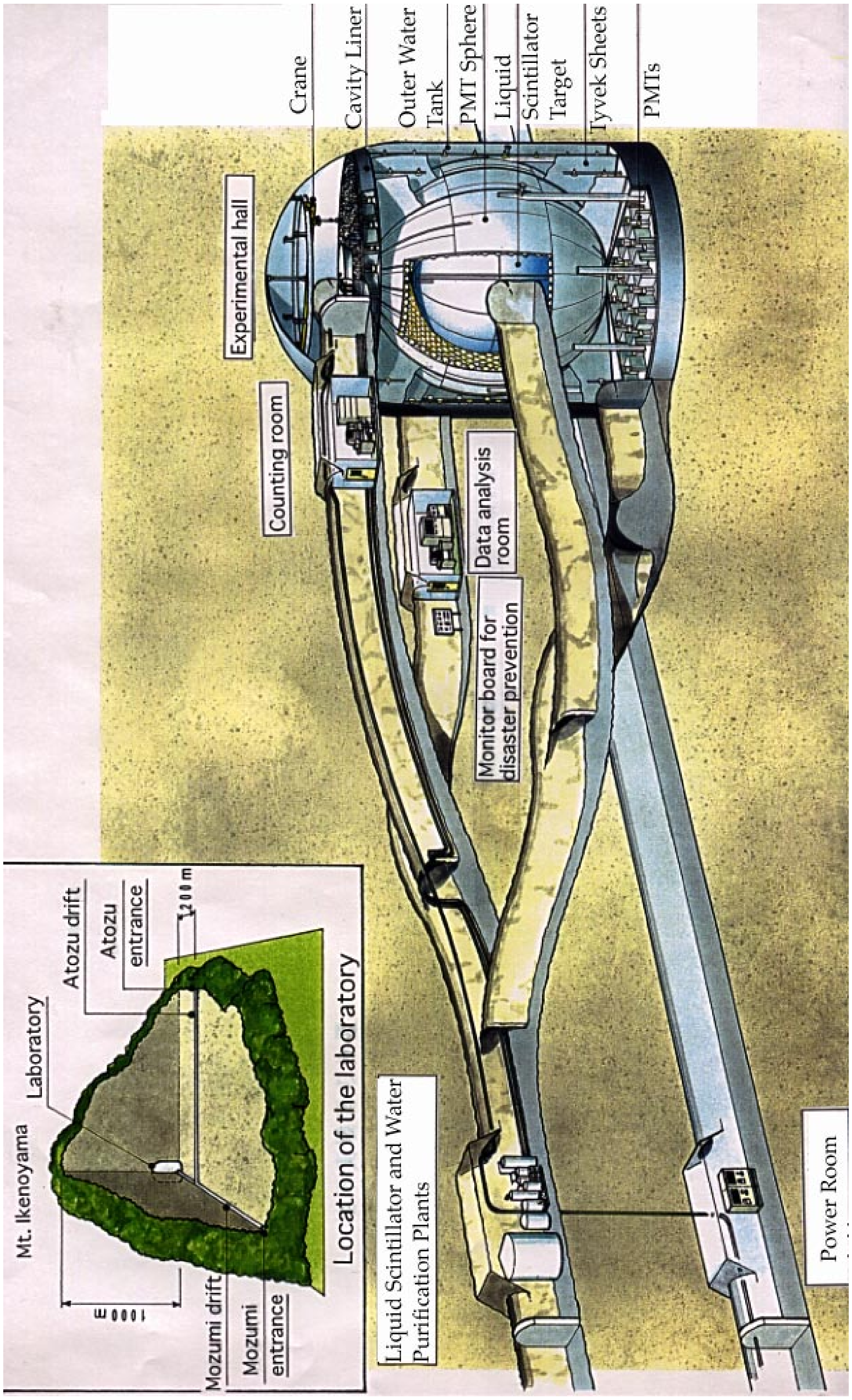

Figure 16: General view of the underground layout in the KamLAND detector region. Several enlarged tunnel sections will house the electronics, scintillator and water purification systems, ventilation system and electrical sub-station.

5 Detector Design

5.1 Overview

A cutaway view of the KamLAND detector is shown in Figure 16. The detector consists of a series of concentric spherical shells. The primary detector target consists of 1000 tons of ultrapure liquid scintillator located at the center of the detector. Surrounding the scintillator is a spherical shielding shell $\sim$ 2.5-m thick of ultrapure mineral oil buffer. Separating these two regions is a thin wall, transparent plastic sphere ($\sim$ 6350 mm radius). The plastic sphere, or balloon, primarily functions to separate the shielding buffer oil from the scintillator. The balloon can not, by itself, support the mass of scintillator, but will support the small difference of densities of the two fluids. The scintillator is viewed by an array of photomultipier tubes (PMTs) supported on a 9000-mm radius stainless steel spherical vessel. The balloon will be positioned and supported within the PMT vessel on a series of rope-supports. While normally completely surrounded and immersed in an external shield of ultrapure water filling the remainder of the detector cavity, the steel vessel is designed to support the mass of buffer oil and liquid scintillator. The steel sphere is secured to the cavity floor and walls with stainless steel supports. Access to the central volumes is provided by a concentric chimney structure from the upper experimental deck structure through the steel vessel and buffer oil, and provides the top section of the balloon. The outer water shield will be instrumented to provide a cosmic-ray veto detector.

The liquid scintillator produces both a small, directional Cerenkov light signal and a much large isotropic light output for ionizing radiation. Neutron (proton) / gamma (electron) signals will be separated using pulse-shape analysis. Event vertices will be determined using PMT-timing signals and photon distributions.

To record the passage of cosmic rays, the veto counter will record the Cerenkov signals generated in the shielding water. The three regions of the veto counter (ceiling, walls, and floor) will be divided into optically isolated segments.

5.2 Mechanical Structure

The major mechanical component of the experiment is a stainless steel sphere, which contains the liquid scintillator, buffer liquid and inner detector PMTs. The PMT sphere has a diameter of 18 meters and will support a load of 2,500 tons when unsupported by external shielding water. The sphere will be constructed from spherically-formed stainless steel sheets of thickness ranging from 6 mm (top) to 17 mm (bottom). This stainless steel alloy for the sphere and elsewhere in this region of the detector will be selected to survive the aggressive ultrapure water environment and the radioactive contamination requirements of the experiment. There exists extensive literature from the reactor industry to aid in the selection of the stainless steels alloys. Experiences obtained in construction the SNO experiment can provide assistance in specifying appropriate fabrication and decontamination processes to reduce the risks of radioactive contamination of sensitive regions of the experiment. A set of 16 vertical columns and wall braces will support the sphere at its equator via a special ring reinforcement. The detailed design and construction of the PMT sphere has been contracted to The Mitsui Ship-building Company. Mitsui handled the steel construction for SuperKamiokande. It is important to realize that the sphere, besides representing the safety containment vessel for the flammable liquids, is also an essential component for the reduction of radon in the detector. Such a thick metal shell, together with appropriate seals for its only opening at the top, guarantees that no radon from the rocks and other external materials can enter the detector volume, reducing the problem of radon suppression to the clean materials inside the sphere.

A cylindrical stainless steel chimney of ∼3 m diameter will protrude from the top of the sphere to permit access to the central detector. Concentric with the stainless steel chimney will be an acrylic chimney connected to the balloon. Buffer oil will fill the volume between the two chimneys (and between the PMT sphere and the balloon). Scintillator recirculation lines and calibration device deployment fixtures will be mounted in the acrylic chimney. The PMT signal and high voltage cables will be fed out of the buffer oil between the two chimneys and into the detector electronics using special radon-impermeable penetrations. These aspects of detector are illustrated in Figure 17.

The support ropes for the balloon will be fed up through the region between the two chimneys using a deflection sheave. The support ropes will terminate in load-sensing and balancing whiffle-tree structures supported on the deck structure in the cavity. The support ropes will be sealed inside radon-impermeable feed-throughs.

Photomultipliers for the central detector will be mounted inside the sphere on a hexagonal lattice structure as shown in Figure 18. All surfaces on the PMT sphere except the PMT photocathode will be light absorbing to reduce light reflections that confuse event reconstruction. The support structure is designed to accommodate 1,922 17-inch PMTs. In this proposal, the US participants propose the purchase of an additional 652 PMTs, in addition to the Japanese purchase of 1280 PMTs, to realize this full complement plus ten spares.

The veto detector will register traversing cosmic-ray muons via the Cerenkov light deposited in the water layer surrounding the sphere. The total volume of 4,500 m^3 of ultrapure water will be divided in three main sections and contained by the rock painted with water-resistant urethane coating impermeable to radon.

The veto detector will consist of 800 20-inch tubes salvaged from the Kamiokande detector. The PMTs on the ceiling and floor will be suspended from a common PMT mounting secured to the deck structure and cavity floor, respectively. Using the same mounting structure, the PMTs along the cavity walls will be supported along cable structures secured between the deck and the cavity floor. Anti-magnetic shielding from the Kamioka experiment will be utilized to decrease the sensitivity of the veto PMTs to the magnetic fields existing at the walls of the cavity.

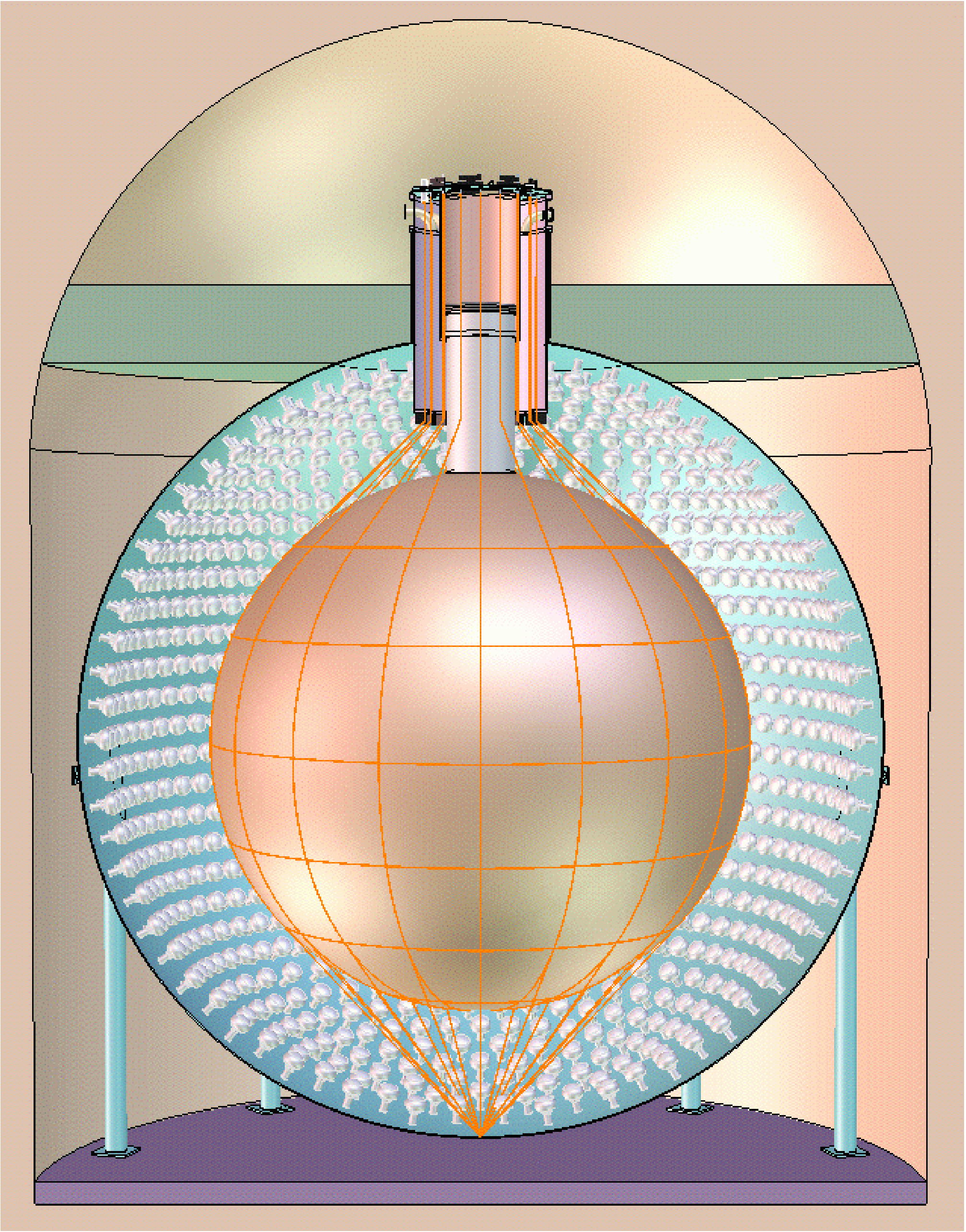

Figure 17: Schematic drawing of the detector chimney. The liquid scintillator, containment balloon, buffer oil, PMT sphere, and chimney sections are illustrated.

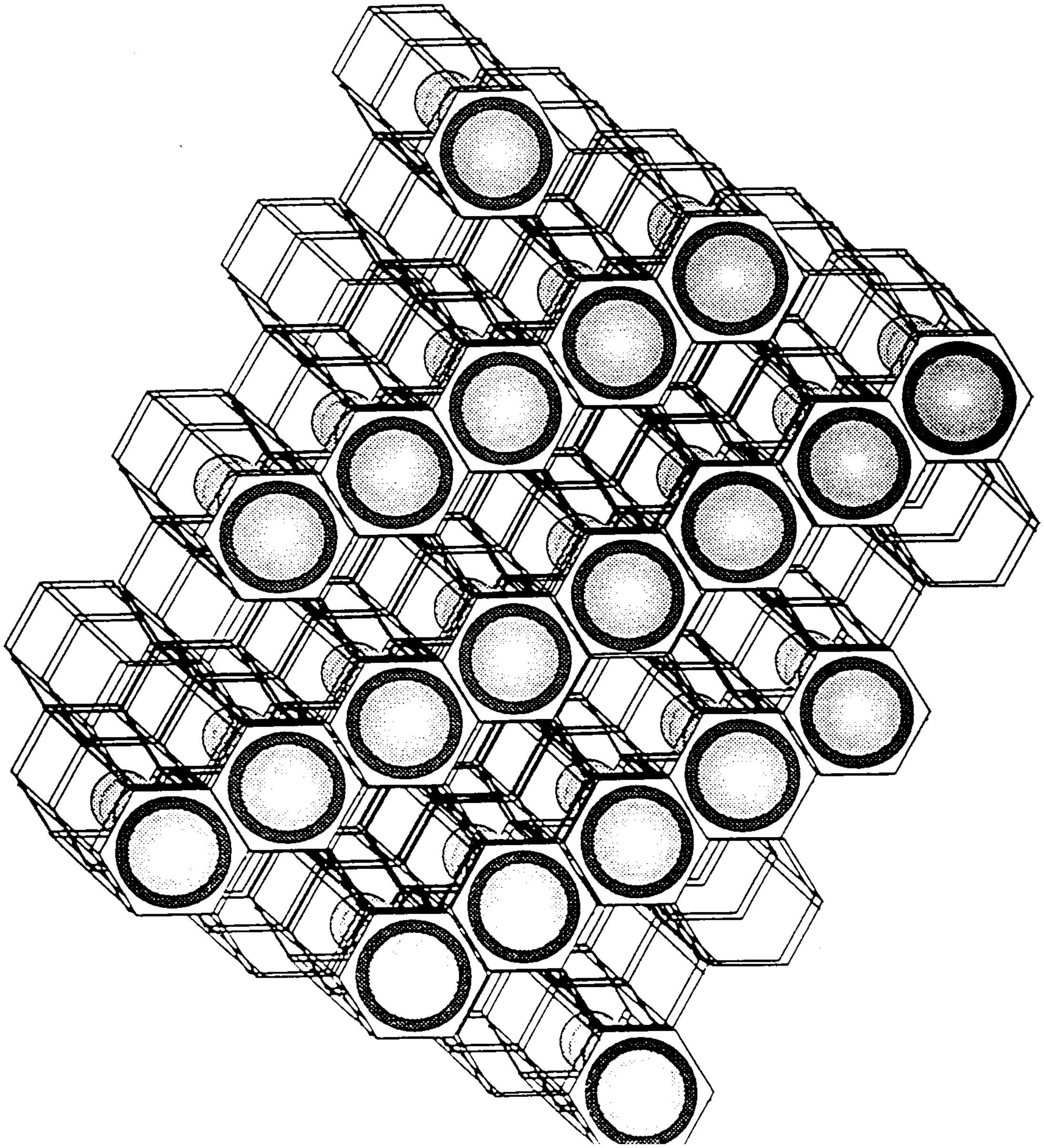

Figure 18: Mechanical structure holding photomultipliers in place inside the sphere. The matrix is shown half-filled, corresponding to a total of about 960 phototubes.

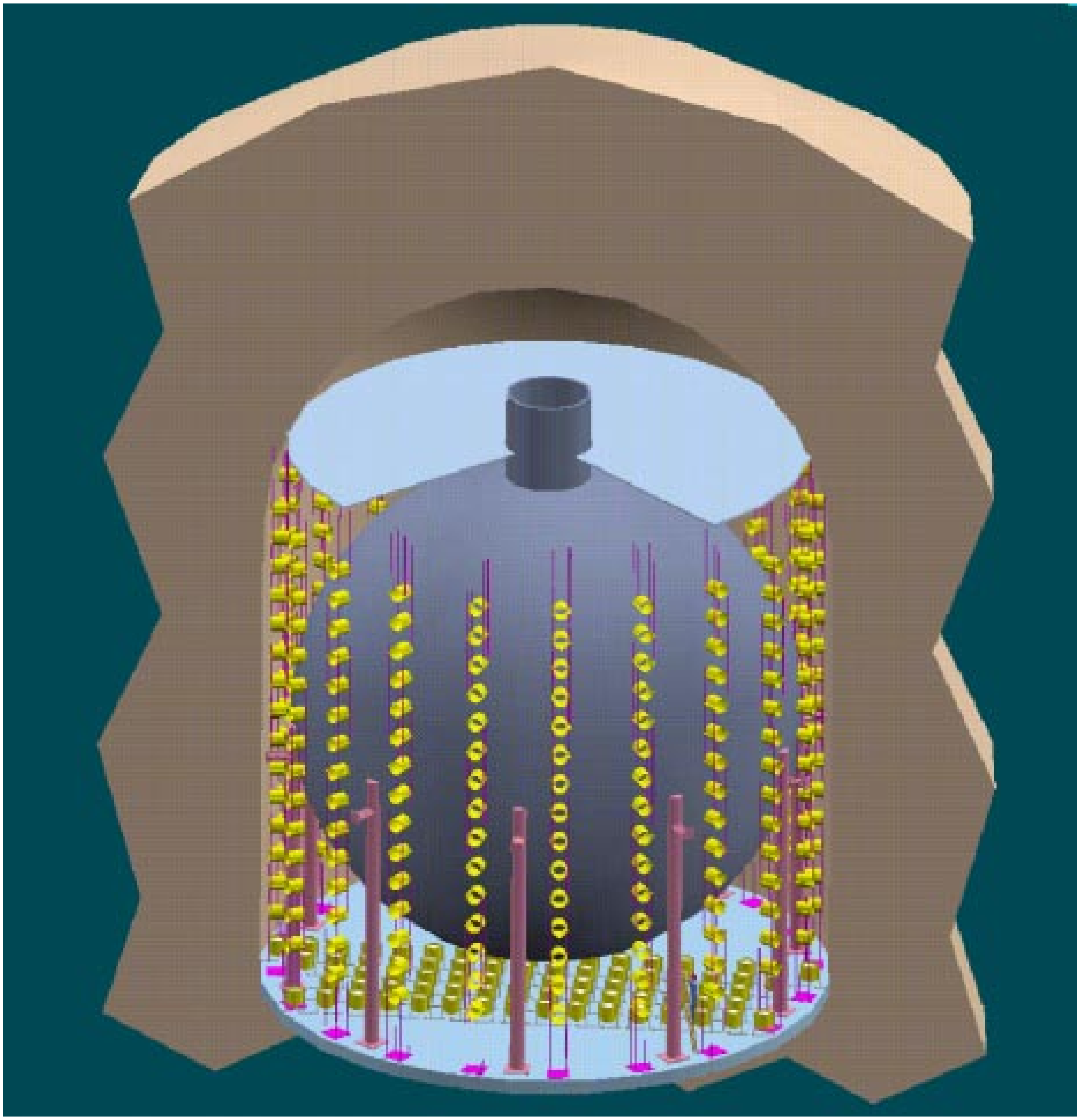

Figure 19: The arrangement of the PMTs in the veto region of the detector. The PMTs on the floor and ceiling are segmented into optically separated cubes. The PMTs along the walls are segmented into vertical lunes. The segmentation is achieved with the suspension of highly reflective materials between the PMTs and the reflective cavity coating.

5.3 Scintillator Balloon Systems

The confinement balloon, separating the liquid scintillator from the surrounding shielding mineral oil defines the central scintillation target in the KamLAND experiment. The balloon is separated into three components: 1) the region-defining material (balloon) and its support mechanism; 2) the chimney coupling the balloon to the outer regions of the experiment; and 3) the external support structure for the balloon.

5.3.1 Target Volume Balloon

The central balloon, a very thin flexible membrane that isolates the liquid scintillator from the external oil, is an extremely critical component of the detector. Its material must be selected to be radiologically pure, transparent for light in the 300 to 500 nm window, chemically inert to both the surrounding oil and to the liquid scintillator, impermeable to radon gas, and stable enough for its properties to remain adequate for the lifetime of the detector. The mechanical and structural design of the balloon must take into account the mechanical properties of the film, bonding techniques and support by the members of the "cargo net" support structure that will carry the load of the balloon to the structural support at the top of the stainless steel vessel. These properties include nonlinear ultimate strength and modulus, creep behavior, and chemical interactions with the surrounding liquids and bonding agents.

A single polymer film that provides all these properties is probably not available, so efforts are being made in Japan to identify films that can be incorporated into a multilayer sandwich that would provide the required properties. The leading candidate is a sandwich of Nylon/EVOH/Nylon. The Nylon provides strength and compatibility with the oil and scintillator and the EVOH provides very low gas permeability.

Initial calculations made at Stanford indicate that a 0.2 mm film with fifteen 3.1 mm × 3.1 mm vertical straps can support a 2.5% density difference between the fluid inside the balloon and the surrounding fluid. In this case seven 3.1 mm × 3.1 mm rings are required at varying elevations along the circumference of the balloon. This number of straps and rings would cover only about 0.3% of the balloon's surface. Several factors will go into the final design of the "cargo net" support for the balloon film, including the available width of the finally selected sandwich. Assuming material available in 48 inch widths and placement of the net cords at the joints between segments where the joint overlap could provide reinforcement, a reasonable design may be 36 (or 18) straps and a corresponding number of rings. Doubling the diameter of the net cords would still only cover about 1% of the balloon's surface. Reducing the density difference between the inner and outer fluids will also make the design of the balloon easier and safer.

5.3.2 Acrylic Chimney

A one-meter diameter opening at the top of the target-volume balloon is required for insertion of calibration sources, scintillator recirculation piping, and sampling devices. In a design similar to the SNO detector, an acrylic chimney will be used for this purpose, the acrylic being a structural material that has very low radioactive contamination and can therefore be extended to the balloon. An inner stainless steel tube extends the chimney from near the top of the stainless steel vessel to the top of the target-volume balloon support structure. Supports for the calibration sources would be provided in the chimney and a slip joint between the stainless and acrylic portions provides compliance from the supporting structure to the balloon while assuring a gas seal between the interior and exterior of the balloon and chimney. A sealing ring at the bottom of the chimney would provide a seal to the balloon film.

5.3.3 Target Volume Balloon Support Structure

The weight of the target volume balloon and its contents must be taken to the detector stainless steel vessel neck and deck. To do this, a system of balanced supports is envisioned in the space between the outer diameter of the acrylic chimney and the inner diameter of the stainless steel vessel neck. The straps of the balloon net would be gathered together after they leave the surface of the balloon and led over pulleys at the bottom of the vessel neck, then brought through gas seals to "whiffle trees" that would carry the load of adjacent straps though a load cell to a cover flange and then to the structural support. These whiffle trees would balance the load of adjacent straps and the load cells would allow balancing the loads of each pair of straps so that uniform loads are maintained over the surface of the balloon. The target-volume balloon support structure also provides space and gas seals for the cables from the photomultiplier tubes inside the stainless steel vessel.

A conceptual drawing of the target balloon, support system, and chimney access is presented in Figure 20.

5.4 Liquid Scintillator and Buffer Fluid

The liquid scintillator confined by the balloon in the center of the detector is arguably the single most critical component of KamLAND. The detection of energy deposits as small as 1 MeV in a 1-kt detector will be possible only if the scintillator has excellent light output and optical clarity. The use of pulse-shape discrimination to separate direct ionization from proton recoil places additional demands on the system. The extremely high purity needed to count singles from solar neutrinos adds complexity to the task of formulating, procuring, blending and purifying such a large amount of scintillator. Moreover, the choice of scintillators is restricted by hazardous materials regulations in the Kamioka mine and by price and availability considerations.

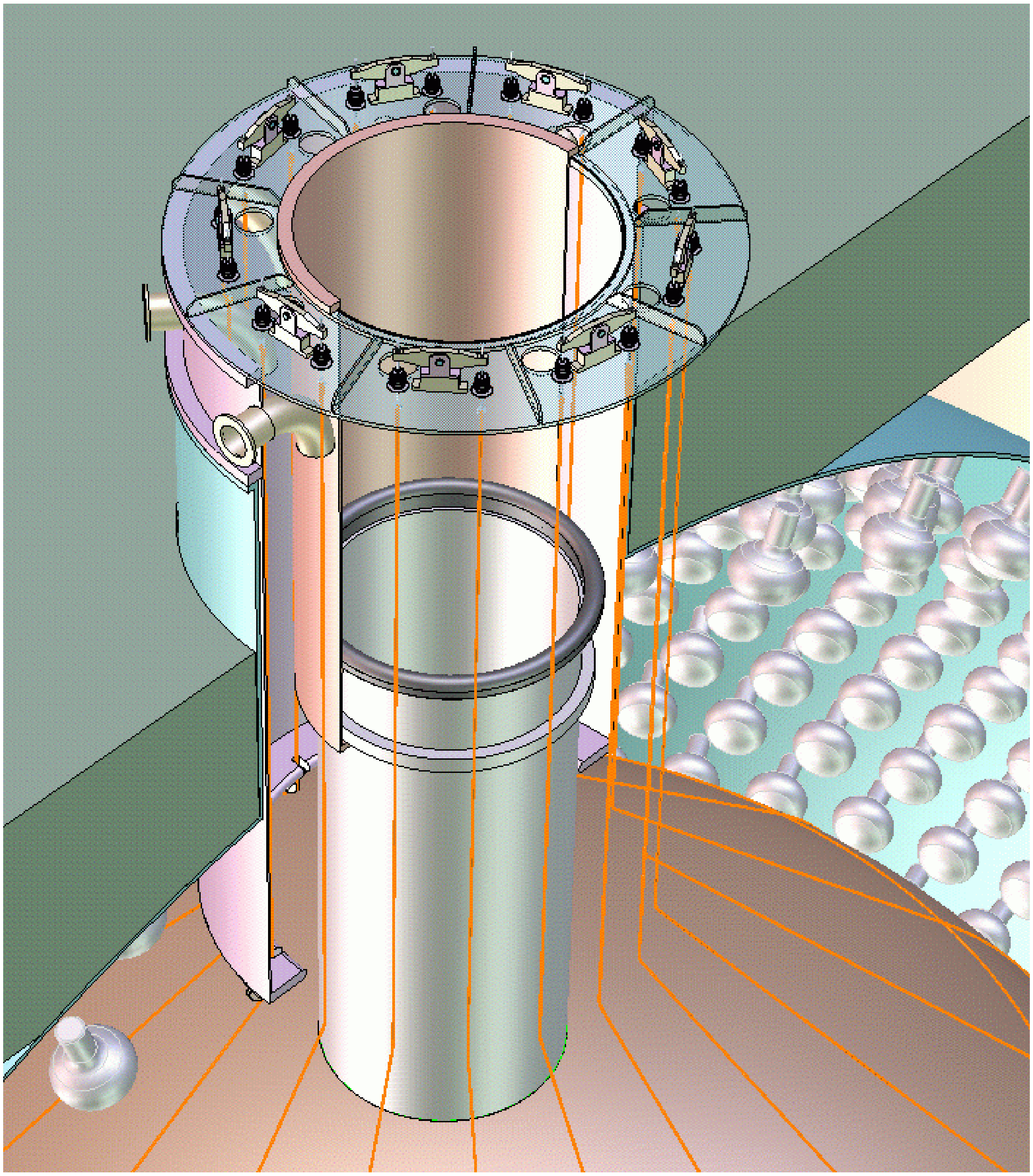

Figure 20: Sketch of the target-volume balloon, supporting ropes, and load-balancing support structure. The transparent balloon and cargo net are supported from the experimental deck structure. The cargo net may be secured to the PMT sphere at the bottom or at additional locations to define and maintain the experimental fiducial volume.

While the Japanese collaboration has responsibility for obtaining and deploying the liquid scintillator, some of the U.S. collaborators bring extensive experience from MACRO, CHOOZ, and Palo Verde, which will be exploited in the R&D program on the scintillator.

The formulation of organic liquid scintillators [64] is based on a general scheme involving the ionization of a bulk solvent and the successive non-radiative energy transfer from the solvent molecules to fluorescent molecules (fluor) dispersed in the solvent at relatively small concentrations. The fluorescent molecules de-excite with emission of photons that are typically in the near-UV to green region of the spectrum. This two-step chain is essential since it allows one to use low concentrations of fluor resulting in small self-absorption and reasonable cost (the solvent being, in general, dramatically cheaper than the fluor). It is important to find solvents with long radiative lifetimes (so that direct de-excitation is not likely) and good ability to delocalize the excitation over large distance, so that a low-concentration fluor has still very high probability of being excited. It is well known that aromatic solvents are very efficient in this respect and most liquid scintillators have been based on such materials.

Because of KamLAND's large dimensions, the attenuation length is an important factor in selecting the scintillator. Since all practical solvents and fluors have absorption bands in the short-wavelength region of the spectrum an obvious solution is to shift the wavelength towards longer wavelength, while remaining within the sensitive region of the photocathode, i.e. between green and the near-UV.

While many experiments choose to use gadolinium-doped scintillators to improve the response to neutrons, this is less compelling for a deep, large detector like KamLAND, where backgrounds are intrinsically lower.

KamLAND has chosen to use a scintillator of simple and well proven formulation: pseudocumene (1,2,4-Trimethylbenzene) as primary solvent with PPO (2,5-Diphenyloxazole) as primary fluor. In Figure 21 we show the light yield in arbitrary units as function of different concentrations of PPO in different aromatic solvents. At least for concentrations above 2g/l there is a very small difference in light yield between the various solvents. The flash-point is lower for toluene (4°C) than for pseudocumene (48°C). The last solvent, DIN (Di-isopropylnaphtalene) is essentially non-flammable (flash point is 148°C) and it presents essentially no health hazard. Unfortunately measurements done at Caltech and Stanford show that phosphorescent states limit the light attenuation length in DIN to a few meters.

In order to keep the flash point of the fluid above the value required by the Mining Company at Kamioka we have studied the possibility of diluting the pseudocumene in a co-solvent like isoparaffin or mineral oil. Both these compounds have low vapor pressure, high flash point (90°C), and low toxicity. In Figure 22 we show how the light yield decreases for increasing dilution of the primary solvent in the isoparaffin.

Choosing a 20% concentration of pseudocumene in the oil retains most of the scintillator properties while substantially reducing flammability, toxicity and cost.

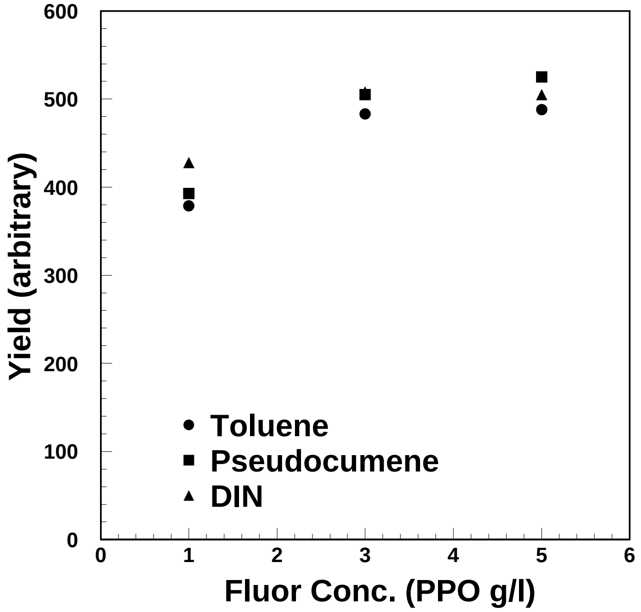

Figure 21: Light yield for different concentrations of PPO in Pseudocumene (squares). Also shown are the yields for the same fluor in Toluene and DIN.

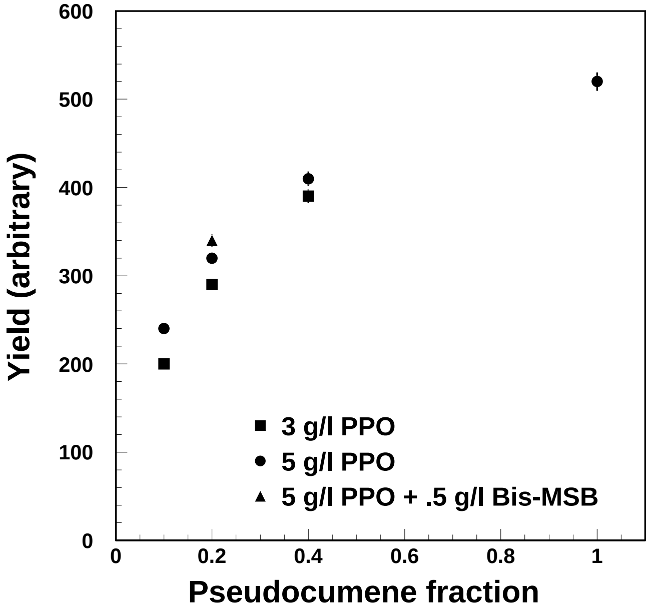

Figure 22: Light yield for different concentrations of primary solvent (Pseudocumene) in a co-solvent (isoparaffin). Data for different fluor concentrations is shown. We also show (triangle), for one case, the effect of adding a secondary wavelength shifter bis-MSB to the cocktail.

The flash point of such an cocktail is increased to (62.5°C), above the (60°C) limit mandated by the mine operations.

While some details of the formulation like the exact concentration of PPO and the possibility of adding a secondary shifter (bis-MSD) to better match the wavelength of the scintillation to the transparency of the liquid are still under study, the cocktail described above has been demonstrated to achieve properties that are totally adequate to the physics to be performed in the first phase of Kamland. In particular it has a light yield of 50% of anthracene and attenuation length better than 12 m (at $\lambda = 440$ nm), resulting in an energy resolution $\sigma(E)/E = 10\%/\sqrt{E}$ (assuming 30% photocathode coverage, 20% photocathode quantum efficiency and 80% transmission from balloon and glass). For γs we have also measured a pulse FWHM of 9 ns that we expect, from simulation studies, to result in a position resolution $\sigma = 10$ cm at 1 MeV.

From laboratory tests we expect a quenching factor of about 14 for scintillation produced by α particles (relative to γs). This factor is used in our Monte Carlo studies and it is very important in the suppression of backgrounds from radioactive decays. We have also measured good pulse-shape discrimination (PSD) between scintillation produced by neutron-induced recoils and γs. This is shown in Figure 23 where we show the measured ratio between the total charge in a pulse and the charge after 25 ns for γ events and neutron recoils. The three plots represent different pseudocumene concentrations. It is clear that the 20% pseudocumene concentration chosen for the KamLAND formulation still gives a substantial PSD. Since our detector is built in such a way that only direct photons from scintillation are detected (light is absorbed at the first scattering) PSD will also be functional in the full-size bulk scintillator. However, while still investigating how to best use this property for background suppression, we have conservatively not used it in the simulations performed for this Proposal. PSD will be further studied at the Tohoku University Test Bench Facility briefly described below and it will be routinely measured in KamLAND by the standard detector calibration runs.

Since the hydrogen/carbon ratio is $\simeq 2$ for isoparaffin or oil (C_nH_{2n+2}) and 1.33 for Pseudocumene (C_9H_{12}) the cocktail described above will have a ratio of $\simeq 1.87$.

Since the liquid outside the balloon does not contain pseudocumene it is important to understand the difference in specific gravity between the fluids on the two sides of the balloon. A 1% difference gives a 10-ton force that the balloon has to withstand. In a recent study performed at Drexel it was found that oil with appropriate light transparency can be obtained in a broad enough range of specific gravity (and viscosity) to be able to compensate for the somewhat heavier pseusocumene fraction. While it is in principle possible to design a completely neutral situation it is convenient to guarantee the direction of the force on the balloon (to simplify the restraint system).

During the experiment lifetime both scintillator and buffer fluid will be continuously purified to reduce the background from internal radioactivity. While typical levels of U, Th and ^{40}K contamination in good quality isoparaffin are 10^{-13} g/g, we

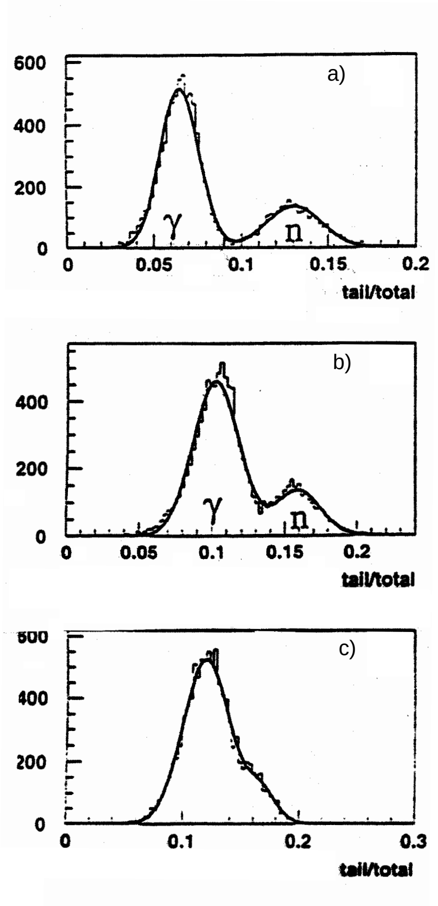

Figure 23: Pulse-shape discrimination in KamLAND scintillator. We use the ratio between the total charge and the tail charge (25 ns to ∞) as a variable to statistically discriminate between γ-like events and n-recoils. This variable is shown for 50%, 20% and 10% Pseudocumene concentration in the scintillator (respectively parts a), b) and c)). Neutron contamination for a cut preserving 90% of the γs is respectively 1.5%, 6.5% and 20%.

will need to reduce them to at least 10^{-14} g/g for the reactor experiment and 10^{-16} g/g for the solar neutrinos . The purification system will need to remove these "original" contaminations as well as the radioactive nuclei produced initially and during the lifetime of the experiment by cosmogenic activation (mainly ^{7}Be) and radon decay (^{210}Pb).

Purification methods [65] have been developed by the Borexino group that needs, from the very beginning, contaminations of order 10^{-16} g/g. These methods are highly effective at removing U, Th, Pb, K and Be and purity levels below 10^{-15} have been reached for U, Th, at their test facility. The process, that serves to extract Pb and Be as well, is based on the higher affinity of metals for highly polar solvents like water. Water is first mixed with scintillator and then separated into two fluids by gravity. Nitrogen purging then removes the dissolved water as well as the radon (although the recirculation time in the purification process is too slow to serve as an effective Rn abatement tool). Since the efficiency for removing Be is several orders of magnitude lower than for U, Th, K, and Pb, vacuum distillation is then used to remove Be and to increase the attenuation length by removing chemical compounds. In addition $0.05-\mu$m filtration is used to remove dust and other macroscopic contaminants.

Although these techniques (developed for a pure pseudocumene scintillator) cannot be directly employed on the KamLAND two-solvent scintillator, we are currently developing a similar purification system employing only water extraction and ultra-filtration steps. A prototype of this system has been built to work with the scintillator Test Bench Facility at Tohoku, processing 20 l/hr of scintillator. With such a detector we will be able to test the effects of purification down to 10^{-13} g/g of U and Th by detecting sequential decays in the decay chain. To achieve the greater sensitivity we are developing condensation and neutron activation analysis techniques. In Figure 24 we show the 1 m^3 test bench now in operation at Tohoku University.

A large water purification system will be built at KamLAND to treat the water of the veto counter and to provide ultra-clean water for the scintillator plant. The system will use water from the same springs under Mt. Ikenoyama that are already feeding SuperKamiokande. Ultra-filtering and ionic exchange in CR55 chelate resin provide the purification. Great expertise on this topic is available in the group from the past experience at Kamiokande and SuperKamiokande.

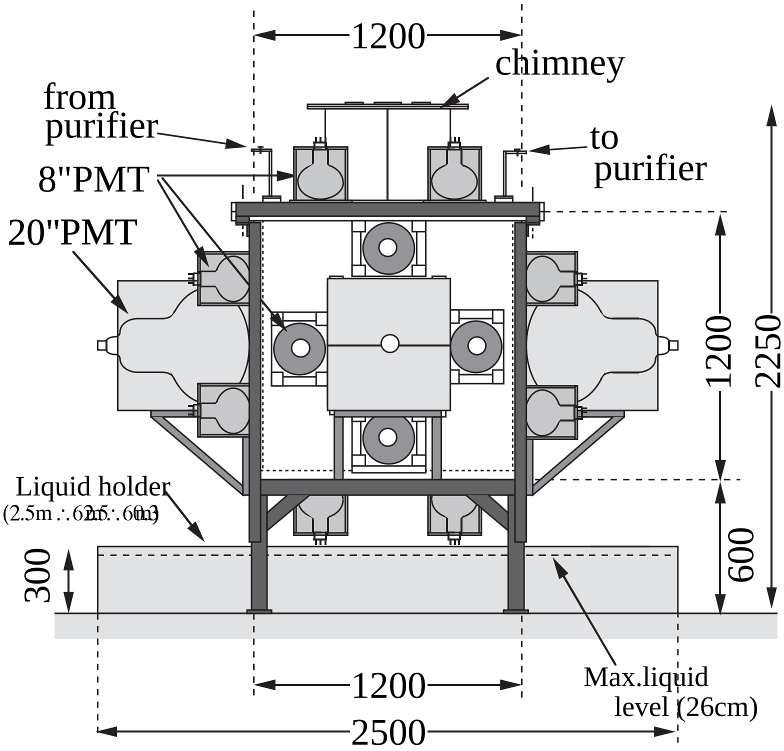

Figure 24: View of the test bench in operation at Tohoku University.

Parameter	Minimum	Typical	Maximum
Quantum Efficiency at 480 nm	20%	22%	-
HV for 10^7 gain	1600 V	2300 V	2500 V
Dark current at 10^7 gain, 25° C	-	83 nA	400 nA
Dark rate, > 0.25 p.e. at 10^7 gain, 25° C	-	25 kHz	60 kHz
Time resolution (FWHM)	2 ns	3.1 ns	4.0 ns
Rise time at 10^7gain	-	7 ns	9 ns
Transit Time 10^7gain	-	110 ns	130 ns
Peak-to-Valley Ratio at 10^7 gain	1.8	3.3	6.0
Cathode uniformity	-	-	10%
After-pulse fraction (150ns $< t <$ 30s)	-	-	7%

Table 13: Characteristics of 17-inch Hamamatsu R7250 PMTs for KamLAND. These characteristics are guaranteed for the first three years of life.

5.5 Photomultipliers

To optimize the photon collection efficiency and physics reconstruction accuracy, a large fraction of the experimental surface needs to be instrumented for photon detection. KamLAND will use a hybrid of the 20-inch photomultiplier (R3602) manufactured in large quantities for SuperKamiokande experiment by Hamamatsu. To significantly improve on the transit time spread (TTS) in the timing signals from the large area tube, the photocathode is masked down to the equivalent acceptance of a 17-inch PMT. By reducing the photon acceptance to the central 17 inches of the front face and by introducing a fast linear focusing in place of the older and intrinsically slower venetian-blind multiplier section, the TTS is reduced from ~ 10 ns to the order of 3 ns with a small and acceptable trade-off in collection efficiency. Production of the new model (R7250) has commenced and the first several hundred of these PMTs has been received in Tohoku in February 1999 for acceptance testing.

The full characteristics of the PMT are presented in Table 13. See also Fig. 25.

The photomultiplier mechanical support structure can hold a maximum number of 1,922 tubes arranged on a hexagonal lattice. This would correspond to about 32% photocathode coverage. Hamamatsu has been contracted to provide 1280 PMTs for Tohoku University and the current US proposal is to provide the remaining 642 PMTs to produce the full complement of 1922 PMTs and spares.

The veto part of the detector will be equipped with approximately 800 20-inch photomultipliers salvaged and refurbished from the Kamiokande detector.

A set of compensating coils embedded in the cavity walls will be installed in the cavern to cancel the Earth's magnetic field (~ 350 mGauss) to a level well below the 50-mGauss limit necessary for proper operation of the photomultipliers. A similar technique is already in use at SuperKamiokande.

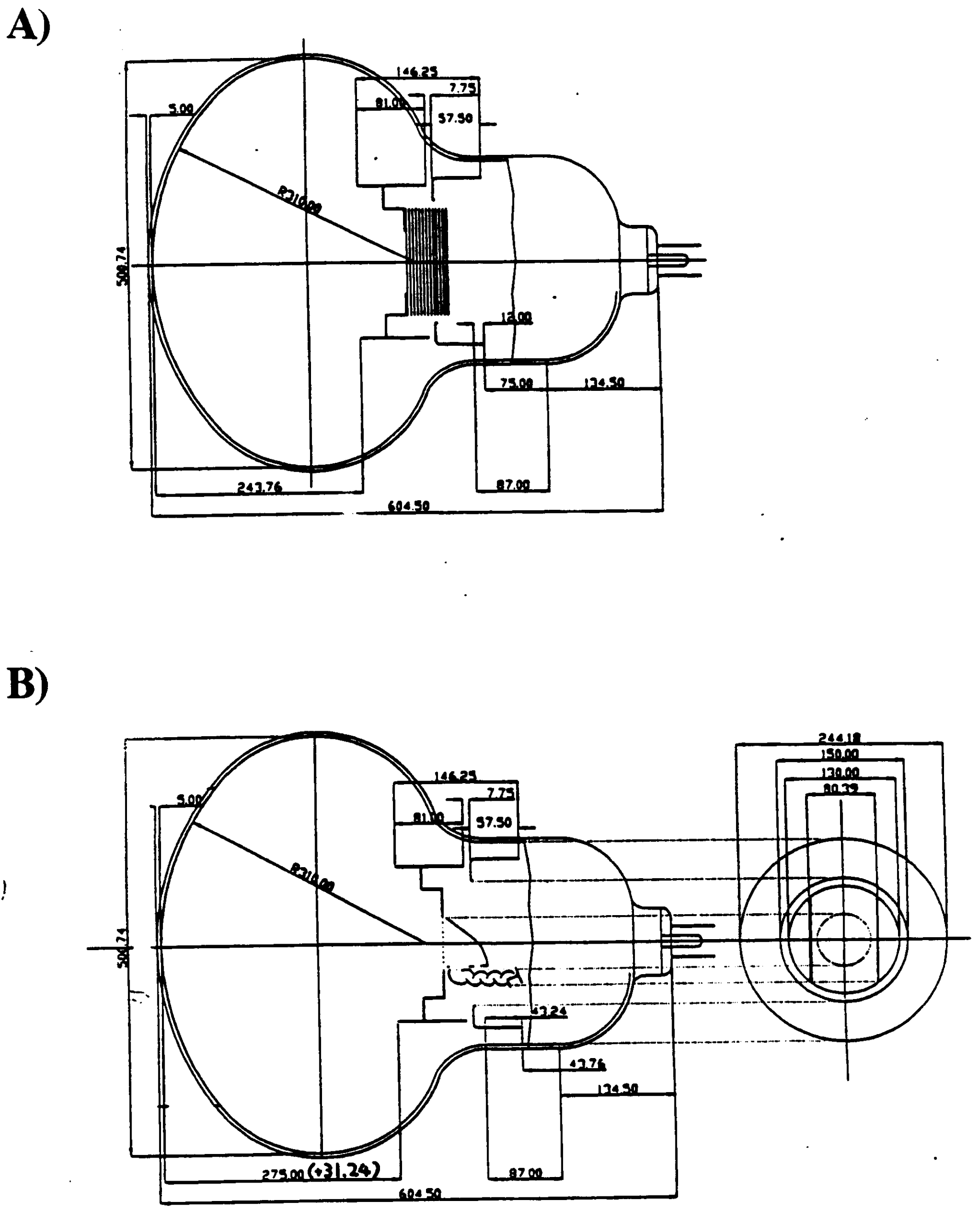

Figure 25: A) The Hamatsu R3602 PMT used by Super-K. B) The new R7250 17-inch PMT from Hamamatsu. The timing characteristics of this hybrid tube are significantly improved.

An oil-proof housing and integral cable connection for both the high voltage and fast signals have been developed using the vast experiences with Kamiokande and SuperKamiokande experiments.

5.6 Electronics

KamLAND will need sophisticated electronics to study reactor anti-neutrinos and solar neutrinos. The physics signals will have rates in the hundreds per day or fewer, while the backgrounds will be orders of magnitude larger. Electronics that provides detailed information on the signals will be essential to overcoming these backgrounds.

A single ionizing particle will generate a signal in many PMTs. The measurement of the arrival times, pulse width, and total charge will reveal the spatial location, the track length, and energy of the signal's source. The pulse shape will carry particle identification information as well. In KamLAND, the maximum difference between the arrival times at the PMTs from a single track is $\sim$ 80 ns, while the maximum duration of a pulse in a single PMT is $\sim$ 100 ns.

A single physics event may be composed of several distinct events, each due to a single particle. These events will be separated by time intervals ranging from tens of nanoseconds to hundreds of microseconds and even to seconds or minutes. The correct identification of an event (e.g., as natural radioactivity, cosmic-ray induced background, or a neutrino signal) requires that all the distinct elements associated with the physics event be detected and properly characterized. Thus the electronics must have "multi-hit" capability over a large range of time scales and a trigger system that can select the events to be recorded.

The specific requirements for the electronics follow from the characteristics of the detector. Two options for the electronics are under consideration and these are described below. Full analysis of these different options is still in progress and must be completed before a final decision is made.

5.6.1 Specifications

We have identified the following major requirements for the KamLAND front-end electronics:

- *Multi-hit capability:*

  Multi-hit capability is required for both the time and amplitude measurements. In anti-neutrino events, the neutron will be detected within $\sim 500\mu$s of the positron's detection (average capture time in liquid scintillator is $\sim 180\mu$s). Electronics with more than two-hit capability will provide:

  - optimized neutron/γ discrimination from detailed pulse history information;

  - suppression of low-energy multi-hit background;
  - full future-past history of single hits in the detector and veto, enabling study of the time correlation between the single hits at the time scale between nsec to minutes.

- *Bandwidth:* Since the risetime of the PMTs is ~ 7 ns and, in addition, ~ 40 m of coaxial cable RG-303 between PMT and the processing electronics will be used, an overall risetime of ~ 8 ns should be expected.

- *Time resolution:* Since the transit time spread (TTS) of a R7250 PMT is 3.5 ns FWHM and the fast decay time constant of the liquid scintillator is a few nanoseconds, an accuracy of the time measurement in each individual channel of ~ 0.5 ns or better is adequate. Overall an off-line space point reconstruction accuracy of ≤ 10 cm FWHM (at 1 MeV) will result from averaging the timing information from several PMTs in an event.

- *Charge measurement and dynamic range:*

  Detection of low energy events requires that each photomultipler tube be capable of single photoelectron (s.p.e.) detection (the scintillator provides a total light yield of ~ 100 s.p.e. per MeV). Thus the range of amplitude measurements is limited on the lower side by the necessity of s.p.e. detection and we assume that the s.p.e. signal will be digitized as ~ 50 ADC counts above the pedestal. This is the most important criterion. However, we also wish to identify and characterize muons that can yield ~ 1000 s.p.e. per PMT. We assume a maximum amplitude per PMT of 2000 s.p.e., requiring an ADC conversion dynamic range of $\sim 100,000$; the global saturation level of ~ 17 GeV.

- *Time development of PMT pulses:* The time interval between different PMT hits, as well as the pulse length for individual PMTs, is in the range of 100 ns. The scintillation process introduces at least two decay times of several nanoseconds and ~ 100 ns; the relative contribution of each depends on the initiating particle. This makes possible discrimination between neutrons and gammas by pulse shape analysis.

5.6.2 Front-End Electronics (FEE)

As noted above, there are two options under consideration to fulfill the demanding requirements of the FEE system. The KEK group will provide a system with minimal capability at low cost available at turn-on. This system would be similar to that used in the Kamiokande, CHOOZ, and Palo Verde experiments and would have two-hit detection capabilities for only 1280 PMT channels in the central detector. Only very limited pulse shape information would be available which would severely limit the n-γ discrimination capability.

The US groups propose to instrument KamLAND with a more complete set of advanced multi-hit electronics that would provide n-γ discrimination. All 1922 PMT's for the central detector would be instrumented. At present we are pursuing the development of two different options for this FEE system which are designated as options 1 and 2 and described in detail below. After a choice is made between these options and the selected electronics is fabricated, the KEK electronics will be moved to the veto system.

The KEK system [71] is built around a conventional ADC-TDC scheme that was developed for previous experiments at KEK [72]. Deadtimeless operation for most events is achieved by fast switching of the trigger controls between two banks of equivalent front-end electronics, as shown in Figure 26.

Additional flash-ADC readout is also envisaged for analog sums of large groups of PMTs; total $\sim$ 10 FADC channels. The trigger will be based essentially on the multiplicity of single hits. Front-end modules will provide two ADC-measurements of signal charge (with slow $\sim 1\mu s$ and fast $\sim 50ns$ gates) and one TDC-measurement of the signal arrival time.

The KEK system has a number of limitations when used for the central detector:

- it will not be possible to achieve complete neutron/γ discrimination in the detector due to the lack of detailed pulse-shape information;
- it will be not possible to suppress certain types of backgrounds. An example is multiple-neutron production by high-energy spallation neutrons and $(n, 2n)$ reactions, which can mimic reactor neutrino interactions in the detector;
- it will not provide effective future and past protection history for background reduction;
- it will not provide deadtimeless operation should there be a close-by supernova event.

Option 1

This electronics concept is based on an approach [73] pioneered by some members of our Collaboration. The system uses a monolithic analog memory ASIC chip (AMU - analog memory unit) [74] including 32 channels of random-access precision analog memory, each with 64 storage cells (time slices). The sampling and recording frequency of the AMU chip is 10 MHz (or one measurement/storage every 100 ns). Each of 32 channels has a built-in ADC, which allows conversion of any or all of 64 stored analog measurements into 11 bits ($\sim 15\mu$sec conversion time). Simultaneous read-write capability and the flexible memory address list manager (MALM) will allow deadtime-less data acquisition in KamLAND at trigger rates even above 1 kHz, and with built-in multi-hit performance.

The second important component in this option is another monolithic ASIC, that we call "instrumentation chip". This device consists of 8 identical signal processing

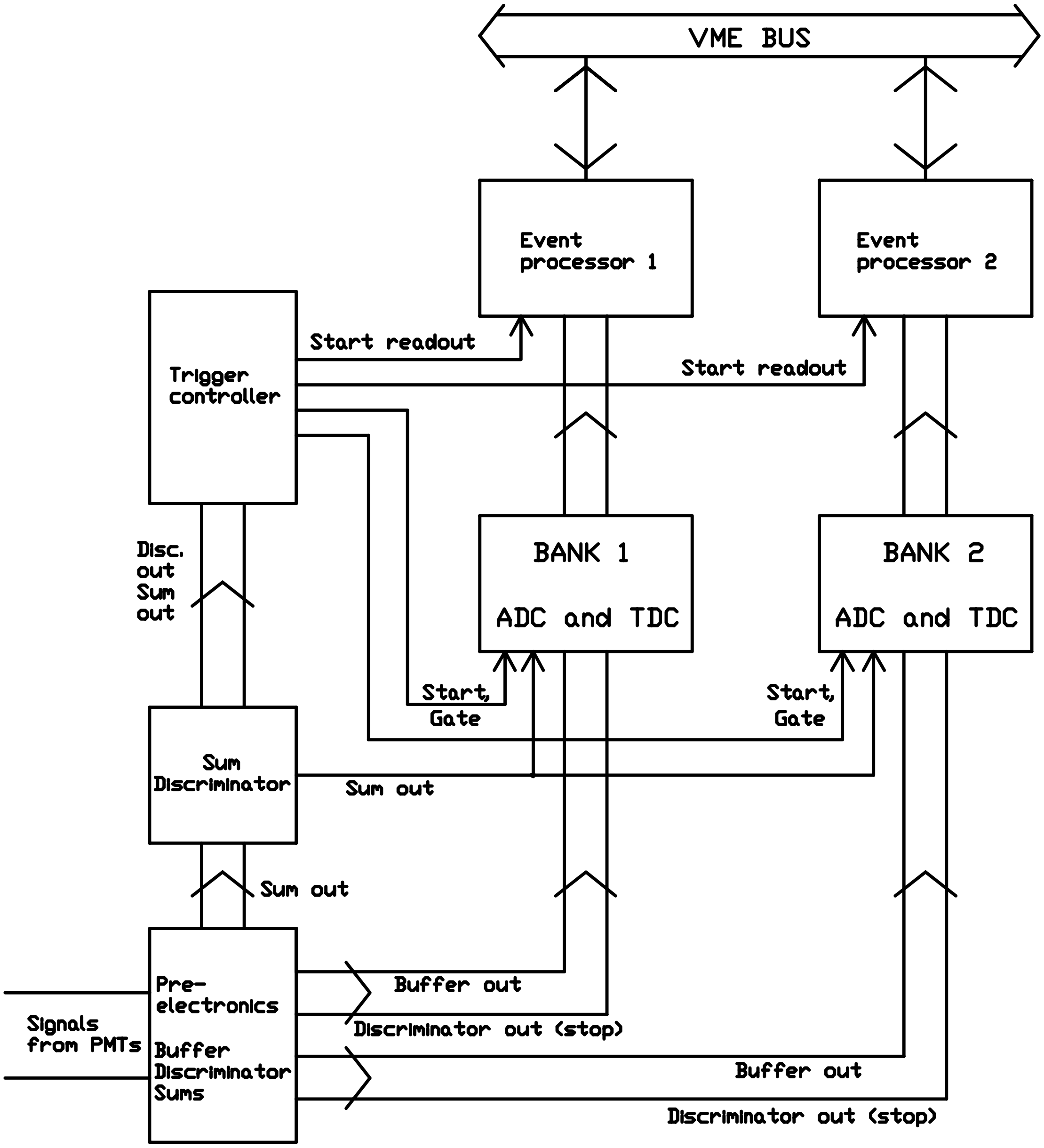

Figure 26: KEK front-end two-hit electronics with two banks of ADC and TDC can provide deadtime-less operation for the first two simple events.

channels, each including constant fraction (or leading-edge) discriminator, charge-integrating amplifier (CIA), programmable gain amplifier, and time-amplitude converter (TAC). Each chip also has calibration circuitry, 2×4 analog sum outputs for triggering, and the serial controls. The particular set and configuration of instruments inside the chip needed for application in KamLAND can be obtained by a customization process prior to mass production of the chip. Typically, one instrumentation chip can provide an input for 16 AMU channels.

The general concept of multi-hit option-1 electronics is shown in Figure 27. Fast PMT signals arrive via 50 Ω RG-303 cables ∼ 40 m long to the receiving buffer amplifier/analog splitter. Various measurable parameters of the input signal (charge integral, arrival time, signal length, etc.) are formed and converted into amplitude information by the instrumentation chip. The various amplitudes are then sampled every 100 ns and stored in the AMU as a sequence of time slices. To provide more detailed pulse-shape sensitive analog information we anticipate that each PMT analog signal will be sampled in parallel by 8 clocks (delayed from each other by 1/8 of the main clock cycle) in 8 separate AMU channels.

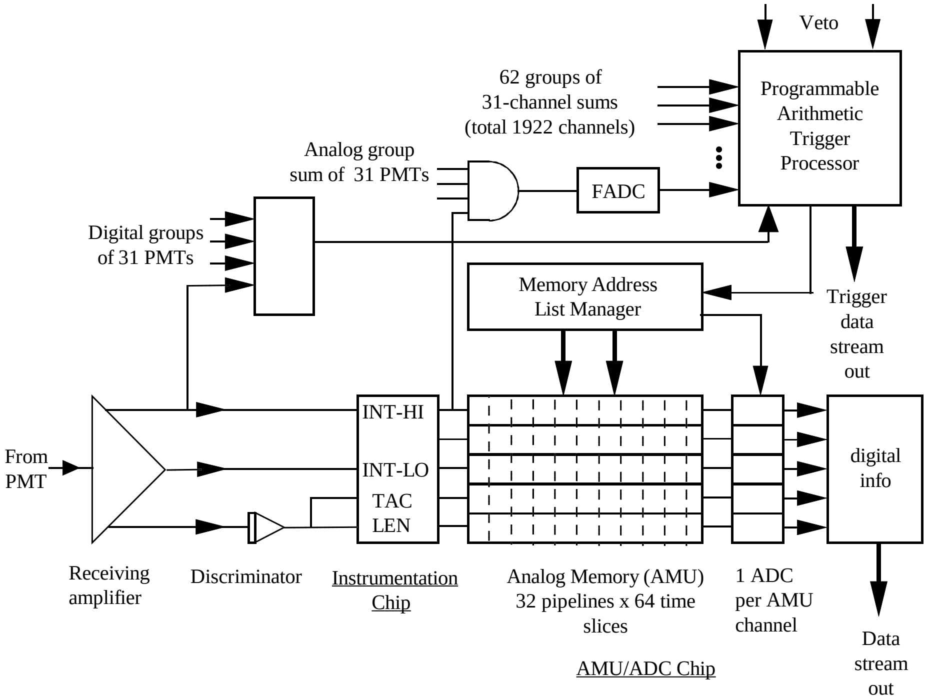

Figure 27: General concept of option 1 front-end electronics.

The principles of operation of this electronics for the measurement of amplitude, arrival time, and signal width are illustrated in Figure 28. The electronics operate with a stable free-running 10 MHz clock. The clock is synchronized with a "Universal Time Standard" and provides an absolute time stamp to the headers of digitized and recorded events.

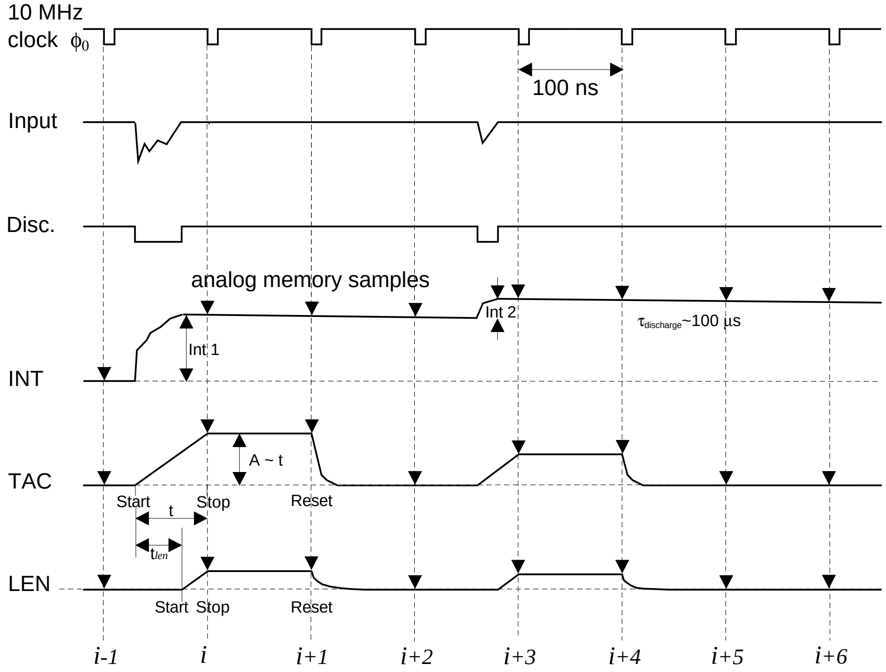

Figure 28: Simplified timing sequence of integrated charge, arrival time and pulse width measurements for readout option 1.

The PMT current signals are integrated by a charge-integrating amplifier in the instrumentation chip (INT time diagram in Figure 28). The charge-integrating amplifier is set to discharge the integrated signal with an RC of the order of a hundred μseconds, which should be chosen to match the average anode current of the PMT and to prevent the saturation of the integrated output. Several signals are integrated and overlapped at the CIA output within a discharge time interval. The reading of any particular integrated signal corresponding to the i-th 100 ns time interval is obtained as an amplitude difference of i-th and (i-1)-th digitized samples .

The measurement of the arrival time is performed as follows. An analog PMT signal triggers the discriminator (with the threshold corresponding to 0.2-0.3 s.p.e.). The leading edge of the discriminator output starts the integration of a constant current in a capacitor. This process lasts until the next clock cycle (TAC in Figure 28) so that the integrated amplitude is proportional to the time interval between the start of the signal and the next clock time signal. The integrated amplitude level is held for the next clock cycle, to allow the storage of its value in the AMU, and then resets during the following clock cycle. Thus, the arrival time measurement requires three clock cycles ($\approx$300 ns). The signal length can be measured similarly (LEN in Figure 28). In the latter case the integration is started by the trailing edge of discriminated PMT signal and stopped by the next clock signal. To provide time measurements for several simple events separated by the time intervals less than three clock cycles, up to four hits per PMT channel are envisaged to be processed in parallel channels for leading and trailing edges of the PMT signals. Several hits in a single PMT channel will occur in KamLAND rather often at a single photo-electron level due to the spread of light in the scintillator decay. Detection of these separate hits will be essential for the ultimate pulse shape discrimination analysis.

All time intervals will be measured with an electronic accuracy of ~ 0.3 ns [73] which will not contribute significantly to the overall time measurement accuracy of $\sigma \sim 1.5$ ns determined by PMT time resolution.

To cover the whole dynamic range of amplitudes from a PMT, two parallel integrator-AMU channels will be used with different sensitivity providing two ranges of 11-bit conversion: 50 ADC counts/s.p.e. and 1 ADC count/s.p.e., respectively. If the high-sensitivity range is saturated the high-sensitivity integrator will be reset during the next 100 ns cycle. Detailed information for the pulse shape discrimination (PSD) will be obtained by multiple sampling of the integrated analog signals for the high- and low-sensitivity range. Eight AMU chips running in parallel with the clock phase shift of 1/8 (12.5 ns) of the main clock cycle (100 ns) will be used. Thus, the analog information will be recorded in 16 AMU-channels for each PMT-channel.

Each PMT-channel is served by 16 analog measurements and 8 time measurements to provide detailed and comprehensive information on the time structure of the event, including PSD. This is equivalent to the 24 channels of the conventional ADC-TDC electronics. It is important to take this factor into account when considering the cost-per-channel for this type of system. Also important that the cost of the proposed electronics is dominated by the constant term related to the customization of ASIC chips and FEE boards design and testing; only the smaller fraction of the cost is proportional to the channel count.

The option 1 electronics would be divided among three types of cards. The first, called "front-end card", contains all the electronics necessary to process 16 PMT signals into various energy and timing values and to digitize them. This card includes 16 instrumentation chips and 16 AMU/ADC chips. Data from 16 front-end cards would travel on a data bus to the second type of card, the "data collection card". This card contains a FIFO memory to buffer the data received from the front-end cards before transfer to the next level of readout. It also contains the memory address list manager (MALM) which controls the reading and writing of the AMUs and the conversion process and readout of the ADCs. The third type of card is the "trigger card". Analog energy signals developed on the front-end cards pass over the trigger data bus segments and are summed by the trigger card. The trigger card completes the processing of trigger information for groups of 64 PMTs and passes that data to the next level of the trigger processor. The entire crate processes the signals from 256 PMTs, so approximately 9-10 crates would be required for all of KamLAND FEE including veto PMTs.

Option 2

In this option we propose to implement a waveform recording technique to capture the PMT signals at a sampling rate of 1 GHz. Thus the shape of each PMT pulse will be well measured, including rise and fall times as well as any structure caused by pulse pile-up. This technique should, in principle, provide not only the best possible recognition of overlapping signals or otherwise anomalous data, but also the best possible time resolution, since the natural variations in pulse shape caused by the stochastic development of the PMT signal may be compensated for at the data analysis stage. (More traditional approaches such as a constant-fraction or zero-crossing discriminator rely on the assumption of approximately invariant waveforms.)

The realization of a 1 GHz waveform sampling capability would be accomplished by an innovative, yet quite conservative, design based on a novel LBNL ASIC called the Analog Transient Waveform Digitizer (ATWD). In this concept, the PMT waveform is captured at a high sampling rate and held temporarily as analog data in an array of storage capacitors within the ASIC. The sampling action of the ATWD is triggered by a pulse-sensing discriminator, and the PMT signals delayed a few ns to ensure that baseline appears prior to the PMT pulse.

The analog data are digitized only if a valid trigger is generated, within a short latency interval. Digitization occurs much less frequently than waveform capture, by roughly a factor of 1000. Thus, the digitization process can occur at much more comfortable speeds, using e.g., a 40 MHz clock. Deadtime for a triggered ATWD begins after the sampling period is complete if the trigger decision is not yet available. Deadtime associated with trigger latency or digitization may be brought to an insignificant level by employing two ATWDs, which can be alternately selected to maximize readiness.

The current version of the ATWD is a third generation design using ordinary 1.2 micron CMOS technology. The sampling action is generated by an active delay line, hard-wired to sequentially close and open the switches connecting the input line to the capacitor array. The sampling speed is controllable from about 200 MHz to 2 GHz by a simple analog DC current. A look-ahead design ensures that the sampling aperture is adequate to achieve settling to approximately 0.1% at sampling speeds at least up to 1 GHz.

The ATWD samples four input channels simultaneously, an extremely powerful capability, facilitating a natural triple-range solution to the challenge of the very high dynamic range requirement. The triple range solution permits the capture of SPE waveforms with quite high resolution. The fourth channel captures the 40 MHz master clock waveform and is utilized for sampling rate calibration and monitoring, which needs only occasional attention.

An internal ATWD 10-bit common-ramp Wilkinson multi-ADC converts all 128 samples of one ATWD channel simultaneously. The internal ADC scalers count on both clock edges, so for example, conversion time with a 40 MHz clock is less than 15 microseconds. As digitization will occur only for those PMT+ATWD channels that contribute to a given trigger, a rate of about 10 Hz, deadtime due to digitization is very small, much less than 0.01%. If saturation is sensed in the highest gain channel, the ADC system can be switched to the next lower gain channel, and so forth.

The ATWD v3 properties are summarized below:

- number of input channels: 4
- number of samples/channel: 128
- sampling rate: 0.2 to 2 GHz, controllable by analog current
- sample span: 64 to 640 ns, depending on sample rate
- input bandwidth: > 300 MHz
- noise/maximum signal: 0.001
- input signal range: 0.2 to 2.4 V
- power dissipation: rate dependent, typically $\ll 100$ mW
- ADC type: common-ramp 128 Wilkinson 10-bit

For Kamland, a fourth generation ATWD could be realized with some straightforward new features that would augment performance and system design. The number of samples could be increased somewhat, perhaps approaching 200 samples/channel. To reduce deadtime further, a "conversion complete" signal would be implemented by adding a simple AND logic to the comparator array, so that after the last comparator switches, clocking could be interrupted and data transfer begun by block transfer to an internal FIFO. If the difference between sampling span and trigger latency can be reduced to roughly 100 ns, then a single ATWD should meet the deadtime requirement.

Time-stamping at the ns scale is accomplished by a coarse and fine measurement approach. Coarse time-stamping involves counting a master 40 MHz clock in a 32-bit scaler, transferring the instantaneous value to a register upon a trigger. The fine time-stamp is determined by the relative "phase" of the clock waveform and the PMT pulse, as captured by the ATWD. Thus the fine time-stamp is unaffected by finite threshold/time-walk effects. A simplification can be obtained by resynchronizing the ATWD "launch" to the master clock; this ensures that the clock waveform always appears with identical timing in channel four. Thus, channel four need be read out only rarely. In this scenario, the PMT signal must be delayed at least by the clock period to accommodate the additional resynchronization delay.

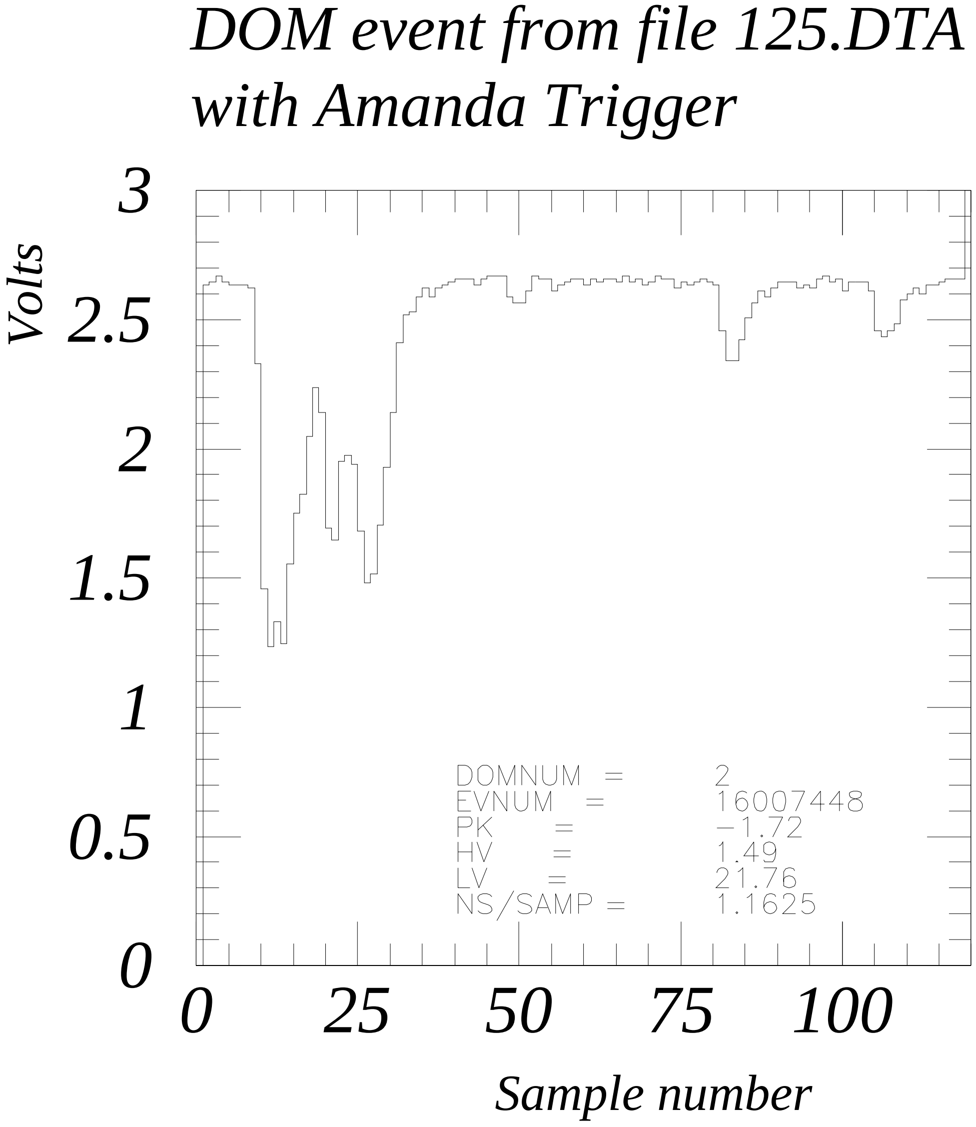

Figure 29: Sample waveforms recorded with the ATWD chip in a DOM-module of AMANDA deployed in the deep ice at the South Pole.

The second generation ATWD has been incorporated in a prototype ”digital optical module” (DOM) for AMANDA. Two prototype DOMs were deployed in the deep ice at the south pole for evaluation purposes. These DOMs returned digitized PMT waveforms caused by Cerenkov light from high-energy muons reaching the deployed DOM depth. Example waveforms are shown in Figure 29, illustrating the detailed nature of the information available with this basic technique. In particular, it is clear that highly overlapping pulses are easily resolvable. Such a capability should improve the quality of KamLAND data substantially. In summary, the proven capability of the ATWD provides a natural, economical, and powerful approach to the challenging issues of high resolution primary data capture.

5.6.3 Trigger and Data Acquisition

We begin with a discussion of the general requirements and specifications of the trigger.

- *Threshold:* The lowest energy trigger threshold will be determined by PMT thermal noise and by low-energy γ background. The PMT thermal noise ranges from 5 kHz to 60 kHz per PMT with an average of 25 kHz in the air at room temperature. The operation of PMT in oil at a temperature of $\sim$ 10°C in the Kamland detector should reduce the average noise down to a level below 5 kHz per PMT. The average noise in the Super-Kamiokande detector is 3.9 kHz per PMT. From this point of view a global single-event threshold of 0.2 MeV (30 s.p.e.) is attainable.

- *Trigger rate and dead time:* One of the limitations of high trigger rates generally associated with low trigger threshold is an increase of the dead time due to event conversion and readout. In particular, high trigger rate capability is also required for the efficient detection of supernova neutrino-events where the trigger rate can be as high as a kilohertz for a time interval of several seconds.

- *Trigger time resolution:* Since the maximum duration of the PMT signals and the time difference between PMTs are both $\sim$ 100 ns, a trigger resolution time of $\sim$ 200 ns is appropriate. That means that all data required for the trigger of each simple event will be contained within a $\sim$200 ns time interval.

The trigger in KamLAND could simply be based on a global threshold for the total energy deposit in the detector. A trigger rate below 10 Hz should be possible with a global threshold of $\sim$ 0.3 MeV. A set of energies from several large PMT patches and/or the hit pattern from small clusters of PMTs may be used in addition to accept or reject special categories of events. There are some differences in the trigger organization for the options of the front-end electronics which were discussed in the previous section.

For the KEK system, the trigger decision time should be as short as possible to save cable length in each PMT channel (used for compensation of the trigger delay). Trigger decisions here will be made by forming the local analog sums of the anode signals in groups of 16, and then by discriminating the integrated-in-time summed signal of all PMT groups (corresponding to 1280 PMTs). Readout dead-time will limit the trigger rate and might require adjusting the global threshold to the higher values or implying a specific coincidence between the first and second simple event triggers in a real event. In the latter case, the global trigger becomes non-universal, and some physics processes based on a single, simple event counting might be sacrificed. Trigger/read-out rate limitations may also affect the efficiency of events associated with supernova bursts.

For option 1, a trigger latency of $\sim 2 - 4\mu$s will be acceptable, and a universal trigger with lower threshold and with more sophisticated event recognition can be used. Readout will be deadtime-less for trigger rates in excess of 1 kHz. Considerable experience exists in our collaboration with the design and implementation of trigger processors [75].

As shown earlier in Figure 27, the integrated analog PMT signals would also be summed into 62 groups of 31 channels for fast flash ADC digitization with the clock frequency of 10 MHz. The flash ADC will provide an energy deposition signal (in the group of 31-PMTs) per time slice of 100 ns to be fed to the trigger processor. Discriminator outputs for individual channels will also be fed to the trigger processor for pattern recognition.

The trigger signal, generated about 2 μs delay after the simple event in the detector, will command the analog memory address list manager (MALM) to mark the time slices containing useful events for digitization. With 64 time-slices-deep AMU, 10 MHz clock, 2 μsecond trigger latency, and with 6 useful time slices per simple event, a trigger rate of up to $\sim$ 7 kHz should provide practically deadtime-less conversion/read-out operation in each channel of the system.

For a single physics event of maximum complexity in KamLAND, there are 24 words of data from each energy channel per time slice (8 analog samples × 2 gain ranges) and 8 words from each timing channel (4 samples × 2 for leading and trailing). With 6 time slices per simple physics event the total of 144 words per PMT-event should be expected. That should be rounded up slightly in calculating the total data rates to allow for headers and other incidental data. Assuming 160 words per PMT-event, two bytes/word and an average event rate of 10 Hz, the data rate for a single PMT comes to 3,200 byte/s. For a 256-channel crate, the average data rate would then be 820 Kbyte/s (or 82 Kbyte per crate per event). For a supernova, the event rate could potentially go to 1 kHz, and the data rate would increase to 82 Mbyte/s for perhaps ten seconds. This data rate could be handled by using more than one 20-Mbyte busses and larger size FIFO memory on the data collection cards. Since the bulk rate of triggers will correspond mostly to the single γ background events with energy deposit ≤ 10 MeV (or average signal level less than several s.p.e. per PMT) a simple zero-channel read-out suppression algorithm can substantially reduce the size of the data stream.

For FEE option 2, triggering will require rapid calculation of PMT hit multiplicity, N_{hits} and deposited energy E_{sum}. These calculations can be done rapidly, as each front-end DAQ card can assemble running digital sums for all channels, and transmit them to the main trigger circuitry within 100 ns. Each DAQ card will sum shaped analog signals and digitize this combined signal at 40 MHz; any of several commercially available FADCs are suitable for this task. The N_{hits} summing is easy. The main trigger unit must assemble the incoming partial sums in sequence and compare the result to predetermined thresholds. The trigger decision should be available at the DAQ front-end cards in less than 300 ns after discriminator transition, perhaps in less than 250, thereby minimizing trigger latency deadtime.

5.7 Veto Counter

The ultrapure water surrounding the PMT sphere serves two important functions. As a passive shield it absorbs much of the radioactivity coming from the walls and moderates the fast neutrons produced by cosmic rays in the rock. As an active anti-coincidence veto it detects cosmic-ray muons traversing it by recording the resultant Cerenkov radiation. The general layout of the veto counter is illustrated in Figure 30. A common stainless steel mounting fixture was developed to secure the PMTs in all three locations. Sensitivity of the PMTs to the magnetic fields at the edge of the cavity may require the use of μ-metal shields. These shields are also available from the Kamiokande experiment. A sketch of the mounting of the PMTs is presented in Figure 31.

The function of the cosmic-ray veto is primarily to record the passage of cosmic rays, not to provide detailed geometric reconstruction of their paths, their energies, or to achieve detailed timing signals. Therefore, to enhance the veto effectiveness, especially considering the directional and relatively short visible flight-path of cosmic rays around the PMT sphere, we have designed a segmentation and reflection screen using a highly reflective material to encase and divide the different regions of the veto shield. The curtains of white specular reflective material on the floors and ceiling will be suspended from a light-duty stainless steel frame (unistrut or similar material). The lune sections along the cavity walls will be formed with material secured with light stainless steel cables. The outer surface of the vessel and the cavity walls will be made reflective, as well, to form the 20 vertical segments. If additional photon collection is required at the waist of the PMT sphere, either smaller 8-inch PMTs can be located there or alternatively, plastic scintillator sheeting might be used. The photocathode coverage on the floor and ceiling would approximately 16% for direct light. The use of the reflective material will significantly enhance this coverage. For a high-energy muon we would expect the detection of more than 600 photoelectrons in each cube. The sparser spacing of the PMTs along the vertical lunes at the edge of the

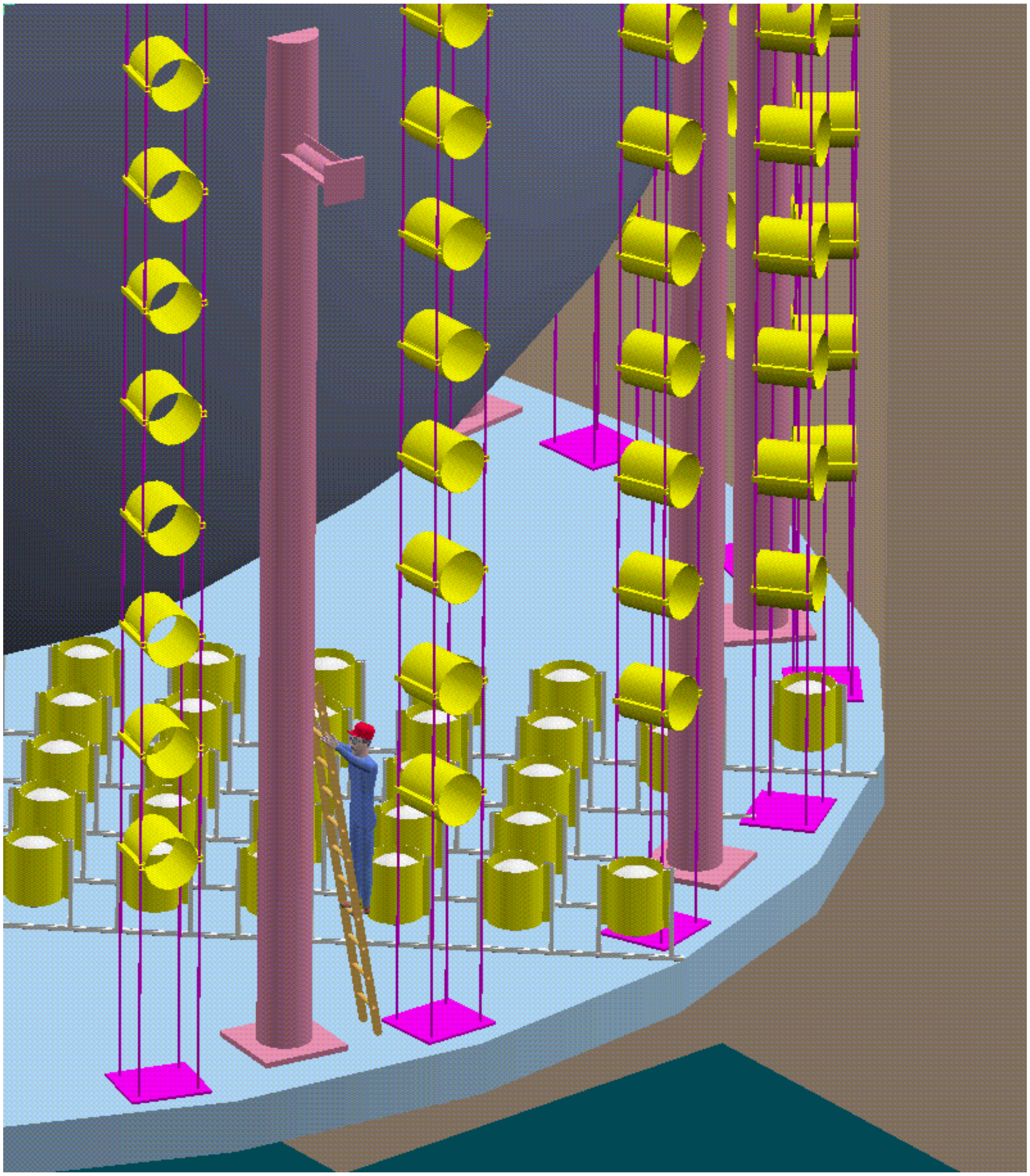

Figure 30: Layout of the veto anti-coincidence detector surrounding the PMT sphere. The PMTs on the floor and ceiling are on approximately a 1.1-meter grid using approximately 500 PMTs. The PMTs along the wall are suspended on a wire-cable anchor with a spacing of ∼ 1.5 meters.

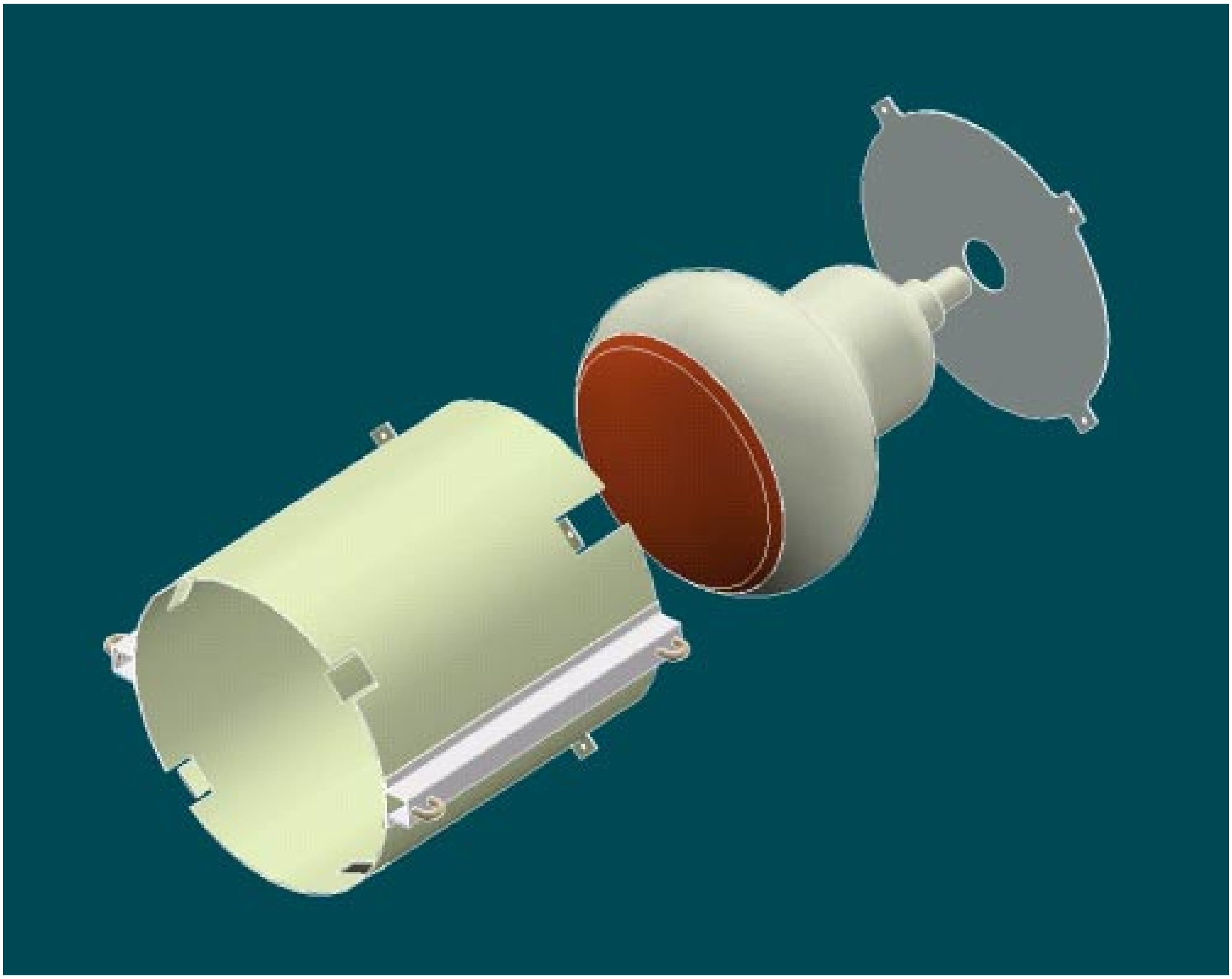

Figure 31: Sketch of the common PMT housings securing the PMTs in the veto detector. The μ-metal shields from Kamiokande may be adapted to fit this housing.

cavity and the significantly different geometry, especially at the detector waist, will somewhat reduce the production and detection of Cerenkov light in these regions. The photocathode coverage in the vertical lunes would be approximately 5.5%, however this lower coverage would be offset by the larger (on average) cosmic ray path lengths in water. The use of reflective material to separate the regions further increases the effectiveness of the cosmic ray muon detection in these sections.

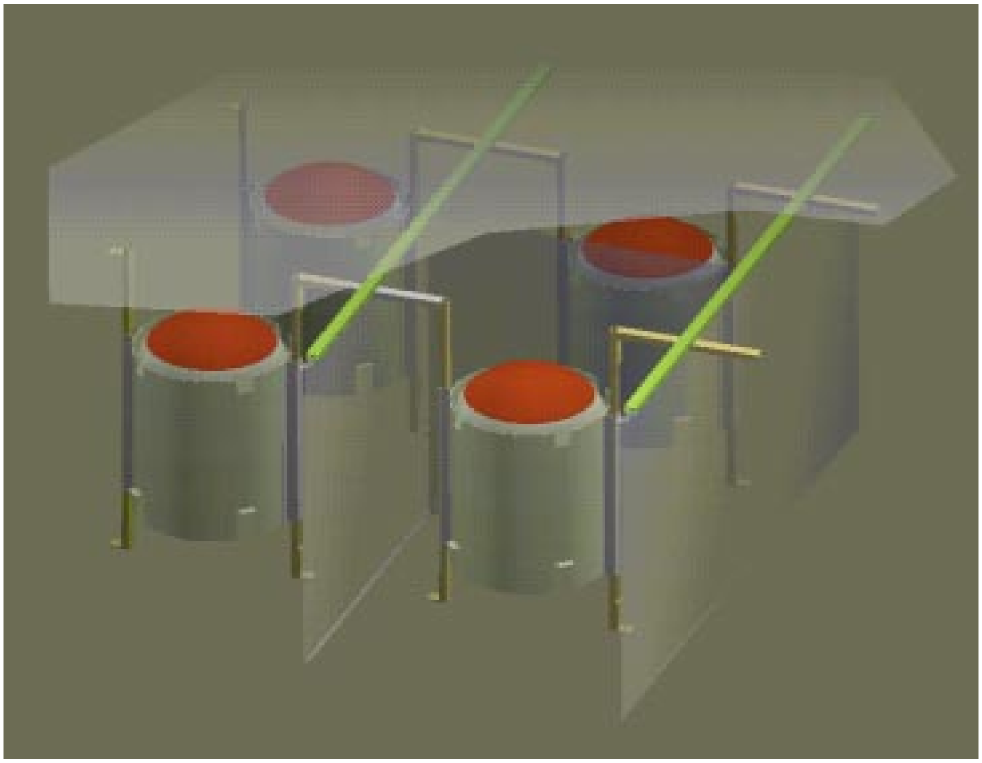

Figure 32: Sketch of the segmentation of the veto counter by Tyvek material. A lightweight stainless steel space frame will be used to support the curtains on the floor and ceiling. The vertical runners will be secured on stainless steel wire rope guides.

The extensive experience in developing the Palo Verde experiment and the Sudbury Neutrino Observatory will be used to specify appropriate materials for the aggressive ultrapure water environment to ensure an appropriate experimental lifetime of the veto counter.

5.8 Calibration and Monitoring Systems

A thorough understanding of detector performance will be crucial in extracting reliable physics conclusions from the observed measurements. To this end an accurate calibration and monitoring system will be installed, which will be used to (a) convert observed pulse heights to energy depositions, (b) relate the timing and pattern of pulses to positions, (c) optimize the discrimination between signal and background, and (d) determine detection efficiencies as a function of energy to an accuracy commensurate with the attainable statistical precision, at least in the energy range relevant to reactor antineutrino measurements. The calibration procedure will rely heavily on direct measurements, but it will have to be based also on detailed simulations of the detector and its response to the events of interest. This is especially important because it will not be possible to duplicate exactly with the available sources all of the characteristics of antineutrino-induced reactions.

It will, of course, also be necessary to calibrate and monitor with comparable accuracy the performance (e.g., power levels and operating characteristics) of the reactors that produce the neutrinos, and the necessary protocols will be set up to insure that this information is reliably integrated into the data stream.

The detector calibration system will consist of overlapping techniques, so that cross-checks can be made and the calibration and monitoring program can be easily adapted to the detector needs based on actual running experience. In the description below, emphasis is placed on calibration and monitoring for detection of low-energy antineutrinos from reactors, but it will be designed so that it can be used also in a variety of other experiments such as those with solar neutrinos, terrestrial radioactivity and neutrinos and antineutrinos from supernovae. The energy range over which reliable calibrations are needed extends from 0.5-10 MeV. It should be possible to extend this range to about 50 MeV by using the decay electrons from stopped muons. The range on the low-energy side can be readily extended down to 0.2 MeV with the use of additional gamma sources of lower energy in order to cover the region important for solar neutrinos.

It is perhaps worth pointing out that many of the reactor-induced events will involve pulses caused by single photoelectrons, and that it will therefore be especially important to determine accurately the single-photoelectron efficiency of each photomultiplier tube. Experience has shown that no single source of calibration can by itself guarantee the understanding of a large and complex detector such as KamLAND. For this reason we propose to install a calibration system that is redundant and will make possible a variety of cross-checks.

The detector will have to be carefully calibrated prior to the start of extensive data taking, and its performance will have to be monitored continuously. The detailed calibration procedure itself is expected to be incompatible with regular data acquisition, and it may well take several weeks to completely calibrate the whole system. We expect that it will probably not be necessary to make such detailed calibrations more than once a year and possibly even less frequently, unless, of course, the response of the detector shows significant changes over time. A system of light pulsers and LEDs will be used to monitor any changes in the response of the detector during the data-taking phase of the experiment.

We will analyze the patterns of pulses in our detector by decomposing them into successions of simple events. The response of the detector to the signal and background processes will then be determined by measuring its response to each of the relevant simple processes. For detection of $e^{\pm}$ and gammas over the relevant energy range we will rely mainly on γ-sources. Energy depositions of $e^{\pm}$ and gammas in scintillator are understood well enough so that detector simulations tuned to the γ calibration data can be used to model the detector's response to $e^{\pm}$. As a check on this method some direct cross calibrations between gammas and $e^{\pm}$ are foreseen using external test facilities in conjunction with mono-energetic electron and γ sources.

The calibration and monitoring system will consist of the following components, which are described in detail in the following sections:

(1) Gamma Sources - Calibrated gamma sources, mono-energetic and point-like, spanning the energy range from 0.5 MeV to 6 MeV would be positioned at different locations within the detector volume. Data from such sources will be used to measure the energy response as a function of position and to tune/check the detector simulation program used to calculate the positron detection efficiency. In particular, the capability to place the source at any position will be exploited for understanding the effect of fiducial volume cuts on detection efficiency.

(1) Neutron Sources - Calibration data similar to that for gamma sources would be taken with neutron point sources positioned at various locations in the active detector volume. These measurements would be used to estimate the neutron detection efficiency and to improve pulse shape discrimination (PSD) as a way to suppress background.

(3)Alpha sources - We will expose the detector to α sources in order to measure the quenching factor and PSD.

(4) Light Flasher System - Sources of short light pulses having the same spectral profile as the scintillation light will be placed at different positions inside the detector. With a dynamic range of one to several thousand photoelectrons per PMT we will be able to study single photoelectron gain, PMT timing (including walk corrections), PMT gain linearity and scintillator stability on a frequent basis. In addition LEDs will be installed to monitor detector response continuously.

(5) Cosmics - Cosmic-ray muons which stop in the detector and decay provide the well-known Michel spectrum with endpoint energy 52.8 MeV. The Michel electron energy spectrum could be used to measure the detector response at the higher energies relevant, for instance, to supernova neutrino detection. Although limited in statistics stopping muons which are captured on nuclei provide another means of measuring the neutron detection efficiency.

5.8.1 Gamma Sources

Gamma sources are primarily intended for calibrating the response of the detector to gammas and positrons in the energy range 0.5-6 MeV. The following sources could be used for this purpose: ^{137}Cs (0.662 MeV), ^{54}Mn (0.835 MeV), ^{65}Zn (1.116 MeV), ^{60}Co (2.506 MeV), Am-Be (4.43 MeV), and one additional source, yet to be selected, to provide a calibration point between 5 and 10 MeV. For example ^{16}N ($T_{1/2} = 7.1$ s) emits a 6.13 MeV gamma (68% branching ratio) which might be suitable. It has the further advantage of having 4.3-10 MeV betas to produce a trigger pulse. Such a source would need some kind of capillary tube. In principle, calibration data from one source combined with measurements from the light flasher system should be good enough to calibrate the detector response; however, given the importance of measuring accurately the energy distribution of positrons in the 1-6 MeV range, we think it prudent to directly measure the detector response at several different energies. It is probably not necessary, however, to perform detailed measurements with every source. For example, to determine position scaling and understand the effects of fiducial volume cuts, it may well suffice to carry out measurements at many different locations only for two sources, a low-energy one and a high-energy one.

Several schemes for positioning the sources within the central volume have been considered. The source-positioning mechanism must allow reliable and reproducible positioning of the various sources over the whole fiducial volume of the detector. Care must be taken that it does not damage the balloon holding the scintillator liquid. External controls and position monitors are needed to move the sources easily and accurately to well-defined locations. Finally it must be capable of being inserted and retracted through the relatively narrow neck of the containment vessel without introducing unwanted radioactive contamination. The sources themselves must be mounted in a stable and leak-proof manner on the source-positioning mechanism. Attention will be paid to minimizing occlusion of scintillation light by the source capsules and the mechanical components. A possible solution is shown in Figure 33 . It consists of swiveling and telescoping parts supported from the chimney, and these can be fully retracted when not in use. The location of the sources would be controlled externally. It may be desirable to fix an LED to the end of the source carriage and to detect its signal as an independent determination of source position. The source positions will be known with an accuracy of better than 5 cm.

5.8.2 Neutron Sources

It will be important to calibrate accurately the neutron detection efficiency for inverse beta decay events in the fiducial volume. A possible source is ^{17}N ($T_{1/2} = 4.1$ s) which can be triggered with an accompanying beta. In addition to detailed simulations direct calibrations could also be made with ^{252}Cf and Am-Be sources. ^{252}Cf is a spontaneous fission source that produces about twenty gammas and four neutrons, on average, per fission. One may trigger on the prompt energy deposit from the

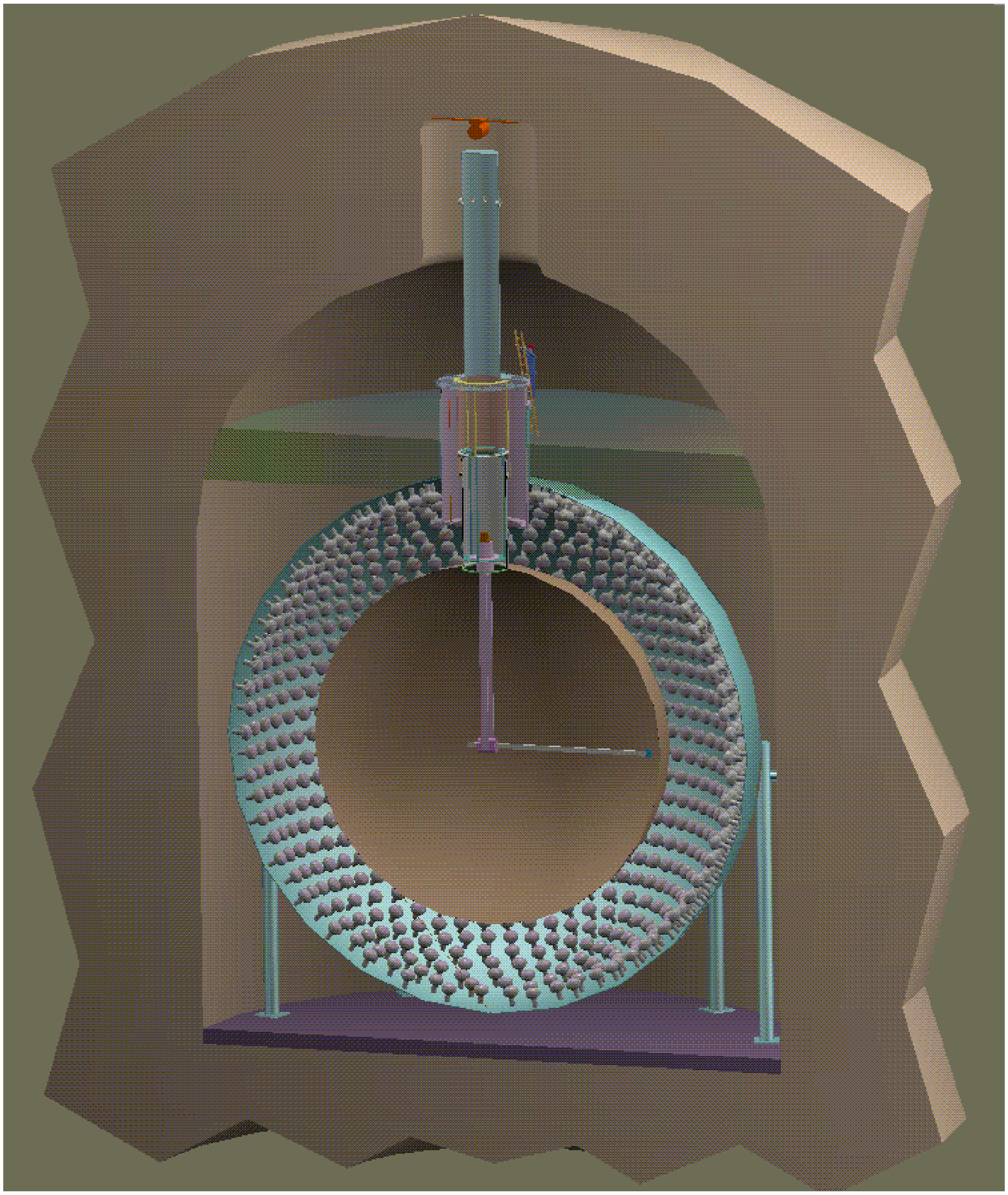

Figure 33: Possible layout for the source-positioning arm.

gammas or a neutron capture and then measure the number of neutrons subsequently detected within a defined time window. The average number of neutrons detected and the mean time between captures can be folded with detector simulation to calculate the neutron detection efficiency. Am-Be is a somewhat simpler source in that for each 4.4 MeV gamma produced, one neutron is produced. One can then collect a sample of events triggered on the 4.4 MeV gamma (plus energy promptly deposited by the neutron) and then calculate the neutron detection efficiency from the subset of events in which there is a delayed coincidence with a 2.2 MeV gamma. To obtain events cleanly triggered by the 4.4 MeV gamma, we could attach a small NaI detector to the source and require that it detect the 4.4 MeV gamma. A complication for these sources is that the produced neutrons typically have energies of the order of a few MeV and therefore they will travel further before thermalization than the neutrons from the inverse beta decay induced by low-energy antineutrinos. Consequently, the detection efficiency for these neutrons must be scaled (by simulation) to take into account effects like position cuts between prompt and delayed events. Although the systematics due to these corrections will probably be small we are also exploring the possibility of using lower-energy neutron sources. One candidate is Sb-Be, which emits neutrons whose average kinetic energy is on the order of 10 keV. Such a source, which emits only single neutrons, would have to be calibrated to an accuracy of a few percent for our purpose. Further work is needed to establish the efficacy of this method. We are surveying other neutron sources with no or very low energy accompanying gamma radiation for the purpose of PSD and quenching calibration. The mechanics for positioning the neutron sources would be the same as that for the gamma sources.

5.8.3 Alpha Sources

Many backgrounds are related to decay chains involving α emitters, so it is important to measure well the energy depositions by α particles. Because it is difficult to handle α sources with very thin sealing layers, we are considering two independent ways to address this calibration. One possibility would be to build a transparent container with walls with an index of refraction similar to that of the scintillator and to fill it with scintillator sampled from the main detector. A small short-lived α source could then be dissolved in the scintillator; (e.g.,220Rn, with a half-life of 55 s is a possible candidate). The container could then be moved through the KamLAND scintillator with the same system used for the other sources with no risk of contamination since the source would be contained inside a thick wall and anyway the isotope has a very short half-life. Two drawbacks of this scheme are that it would not reproduce local variations of scintillator response and it might not be easy to replenish the α emitter in situ. Another scheme is to rely on the ^{222}Rn contamination in the detector as a source of calibration. This source would be spread uniformly throughout the volume of the detector and would be active during the entire life of the experiment. Position information from individual α-induced events could then be reconstructed by using time-of-flight and amplitude information in the same way as is done for neutrino events.

5.8.4 Light Flasher System

The purpose of the light flasher system is to calibrate the PMT timing, balance the gain of the PMTs, and determine the linearity of the PMT response (including readout chain). It will further be used to monitor scintillator transparency, and it will be a useful tool for commissioning and checking the detector readout. To carry out these tasks, we intend to install a light flasher system having the same spectral profile as the scintillator light. It will be capable of producing short pulses of variable amplitude, and provide point sources which are at varying distances from the PMTs. The burden of the above tasks will be mainly borne by a laser-based system similar to one being used by the CHOOZ experiment. In this system, UV light pulses (3 ns width) from a nitrogen laser are injected into a bulb of scintillator which is viewed by the detector. The wavelength of the laser light falls within the absorption band of the scintillator, hence light is emitted having the same characteristics as the scintillator light. As shown in Fig 34, the laser light is transmitted to the scintillator bulbs via quartz fiber optics, and its intensity is modulated with computer-controlled attenuator wheels. It will be monitored using source-stabilized photodiodes and PMTs. We plan to locate eight bulbs at regularly-spaced locations on the PMT support sphere to be used for daily monitoring of the scintillator transparency, and to attach one bulb to the source positioning assembly in order to be able to flash the detector from the same position as the sources during the source calibration runs. To minimize possible contamination of the highly purified scintillator by extraneous objects, no sources will be left permanently in the central detector. One additional bulb, however, will be mounted on a tether so that it can be easily deployed from its "parking" position in the chimney. This bulb will be used to emit light from within the balloon, and thereby to provide us with a controllable light source that originates in the same region as actual physics events.

The laser flasher system is limited in rate to 20 Hz, and therefore, we will also install an LED system to carry out tasks for which accurate knowledge of light intensity is not required but which would benefit from higher repetition rates. These tasks include gain balancing the PMTs, debugging the detector readout, and monitoring single photoelectron gains. A similar LED system will be also used to monitor the muon veto system.

5.8.5 Cosmic-Ray Muons

Electrons from the decay of muons at rest have a well-known energy spectrum which can be used to measure the detector response at higher energies (up to 50 MeV). The rate at which muons stop in the detector is of the order of 0.001 Hz and nearly

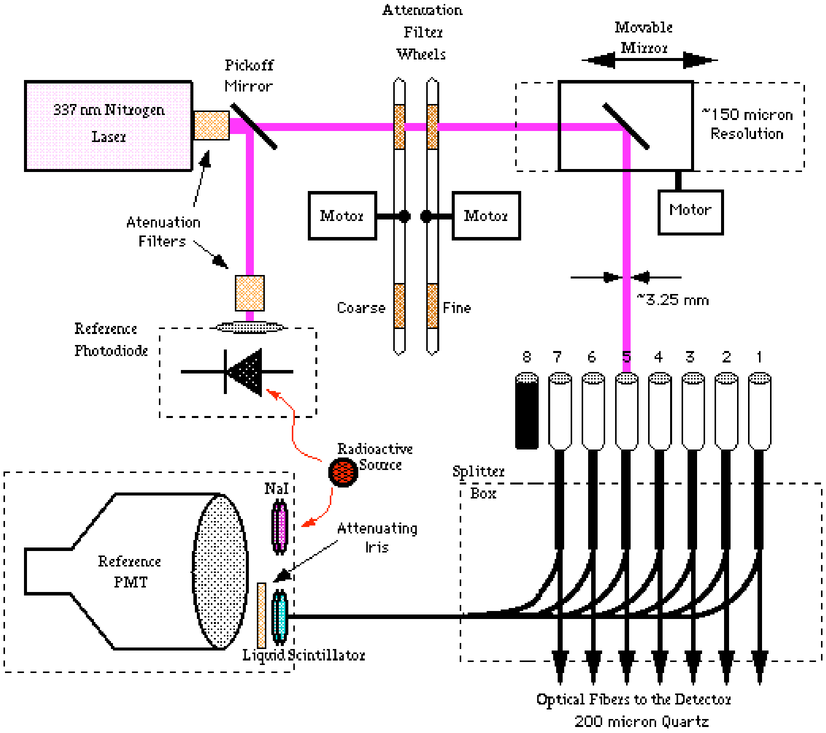

Figure 34: Schematic of system for controlling and monitoring the laser flasher system.

all of the stopped muons decay. Consequently, there will be about 100 muon decay-at-rest events per day in the detector. This rate is too low for dedicated runs, but event samples of useful size can be accumulated with a dedicated trigger for stopped muons that is OR'd with the other experimental triggers. In addition about 3% of negative muons which stop in the KamLAND central detector are captured on ^{12}C nuclei through one of the following reaction channels:

$$\begin{aligned} \mu^- +^{12}\mathrm{C} &\rightarrow {}^{12}\mathrm{B} \qquad (17\%) \\ &\rightarrow {}^{11}\mathrm{B} + n \qquad (78\%) \\ &\rightarrow {}^{10}\mathrm{B} + 2n \qquad (5\%) \end{aligned}$$

By triggering on the stopped muon, it may be possible to exploit the latter two channels and measure the neutron detection efficiency. Although the rate of useful events is pitifully low, neutrons produced in this way and accumulated over two or three years have the potential of allowing a measurement of the time-averaged neutron detection efficiency with an accuracy of a few percent. This technique has been demonstrated by the KARMEN experiment [20].

5.8.6 External Test Facility

As a cross check on the reliability of our calibration procedures, especially in the case of the gamma-positron calibrations, it may be desirable to set up an external test facility consisting of a modest-sized tank filled with scintillator and looked at with phototubes arranged in a configuration which simulates that of the actual detector. In addition to measuring the response of this system to the various sources contemplated for use in the experiment, it may also be desirable to expose it to mono-energetic electrons from an accelerator. Checks on the other proposed calibration methods would be made as needed.

5.9 High Sensitivity Radioassay

The contribution of radioactivity to the KamLAND detector background should be kept to a minimum in order to limit the uncorrelated backgrounds. This is also essential for the solar neutrino experiment. The design and construction of the experiment does not permit a phased approach to obtaining these goals. There do not exist realistic decontamination methods to reduce radioactive backgrounds from the detector components once the experiment is constructed. KamLAND can directly utilize the experiences from SNO's clean-room construction and its severe limitations on radioactivity.

The sensitivity of the KamLAND experiment varies with distance from the central scintillator target. Those materials making-up the central target or which are exposed to the central target have the strictest requirements for low radioactivity. This region includes the target balloon, the suspension ropes, access chimney, calibration devices, scintillator piping and sampling devices, and liquid scintillator. The materials used in the shielding region have the next strictest requirements including the shielding oil, PMTs, PMT cables, and stainless steel vessel. The emanation of radon, a noble gas, with a 3.8-day half-life in the ^{238}U decay chain is of particular concern. The emission of this gas by detector components in different regions can result in higher backgrounds throughout the detector as the radon mixes in the different fluids. In the outer layers of the veto counter we have the loosest requirements. In addition to our concern for the intrinsic radioactive contamination of the detector components, the requirements for surface contamination are equally rigorous. The radioactive contamination of mine dust and construction debris is typically a thousand to a million times that of specially selected materials (for example, stainless steel to acrylic). The material handling and construction practices for KamLAND will require attention to control surface contamination through the entire construction of the detector to achieve its background goals.

The details of the radioactive backgrounds are discussed elsewhere in the proposal. However, to establish a perspective on the required levels of contamination control the concentrations of uranium and thorium in the stainless steel needs to be below approximately 1 part per billion (ppb) while the scintillator will ultimately require levels below 10^{-16} g/g level. Surface contamination requirements will require the average density of "dust" on the detector components within the PMT sphere be below 0.4 g/cm^2 while the levels on the target volume must be at least an order of magnitude lower.

In the following we will discuss separately the facilities we envisage for the qualification of the external components and the plans we have to extend our trace analysis sensitivity to the extreme level required.

5.9.1 External Materials

Much of the monitoring of detector components will be accomplished using the low background facilities of both Caltech and Lawrence Berkeley National Laboratory. Concentrations of U, Th, K, Co in bulk material such as steel, plastic, glass, and cables, which require ppb levels of accuracy, can be obtained with well-shielded germanium detectors. Both institutions have a long and successful history of low-background counting for experimental programs. Caltech has several Ge detectors situated in basement facilities and LBNL has both NaI and Ge detectors in a specially constructed facility in Berkeley. To obtain levels required for the target balloon and inner volume components ($\sim$ ppt level) cosmic-ray backgrounds require the use of very well shielded special low background counting facilities. The LBNL's Oroville facility has the most sensitive direct counting reach of any facility at the collaboration's disposal (underground facilities in Sudbury and Gran Sasso have similar limits).

5.9.2 Internal Materials

The liquid scintillator and all materials close by need to be surveyed to extremely tight activity limits. While the tolerable U and Th concentrations of 10^{-14} g/g are already difficult to test, levels near 10^{-16} g/g, required for the second phase of the experiment are at the limit of today's the sensitivity. While a simple calculation shows that spectroscopy is not a viable option, mass spectroscopy and neutron activation techniques offer interesting prospects, with the caveat that both techniques only probe the long-lived parents of the decay series, hence assuming radioactive equilibrium in the entire decay chains. The SNO experiment used the neutron activation technique (followed by chemical concentration of uranium species) to confirm the bulk of the acrylic used in its central target was below 0.5 ppt for both U and Th.

The first technique has been greatly refined for the study of geophysical sciences. In particular a group at Caltech reported reference measurements of the ^{232}Th content of sea water (in 1 to 10 l samples) down to concentrations of 10^{-14} g/g with a background of 4×10^{-15} g/g (distilled water blank, the filament blank being 1/4 of this value) by means of Thermal Ionization Mass Spectrometry (TIMS). Using the same method this group reports reference a U blank of 3×10^{-15} g/g for their mass spectrometer. To reduce the sample size the U/Th is precipitated quantitatively by using a small amount of Fe hydroxide. As this method is based on U/Th being in aqueous solution we would need to develop a method to quantitatively extract U/Th from an organic solvent into water in order to use it for the KamLAND experiment. This should be feasible by water extraction as U/Th generally have a higher solubility in polar solvents than in organic solvents. We are presently studying the methods to be used to calibrate the extraction efficiency. Careful choice of the chemicals used is needed to make sure that a measured value is in fact not due to a cross contamination. We are discussing this project with G.J. Wasserburg of Caltech and are exploring a possible cooperation in this field.

The Borexino collaboration has developed a very sensitive Neutron Activation Analysis (NAA) reference for meta-stable isotopes. In this technique the sample is irradiated in a high flux reactor, producing unstable isotopes from the nuclei in the impurities. The products of activation of ^{238}U, ^{232}Th and ^{40}K have short lifetimes and decay into ^{239}Np ($T_{1/2} = 2.4$ d), ^{233}Pa ($T_{1/2} = 27.0$ d) and ^{42}K ($T_{1/2} = 12.4$ h) that are then dissolved in liquid scintillator. A coincidence set-up, using a low background Ge detector, helps to selectively count the isotopes wanted with virtually no background. As none of the products of activation occurs naturally, the purity requirements for the chemicals used in the sample preparation can be substantially relaxed compared to a TIMS analysis. Clean room handling and high purity vessels are however needed before and during the irradiation.

Although organic substances are well suited for NAA, as the matrix does not produce long-lived isotopes that could interfere with the analysis, the irradiation of these substances in a reactor is technically rather challenging as one has to deal with substantial pressure build-up due to radiolysis of the sample.

We are planning to start immediately an R&D program on these techniques in order to be able to develop the expertise needed to address the requirements for a very low background experiment.

A Other Physics Targets

Although the reactor oscillation search, and the observation of solar neutrinos once the scintillator purification reaches its goal, will represent the core of research at KamLAND, a number of other measurements, requiring modest backgrounds, will also be possible. These measurements, including detection of terrestrial antineutrinos, neutrinos from a possible supernova, hypothetical sources of astrophysics anti-neutrinos, nucleon decay, atmospheric neutrinos, neutron production by muon spallation in underground detectors, and the possible study of double beta decay with KamLAND, are discussed in this subsection. Although these measurements do not represent the main motivation for KamLAND, they will provide a very interesting complement to the main core of science for little extra effort. However, in most cases the advanced electronics, proposed by the US collaboration, is essential in these applications. The measurement of double beta decay requires, in addition, high radiopurity of the scintillator, and access to the corresponding source material. If that program can be in fact carried out, it would represent a very important advance comparable to the core reactor and solar neutrino programs.

A.1 Supernova Detection

The KamLAND detector, containing a large amount of carbon, opens the possibility of detecting the scattering of ν and $\bar{\nu}$ from supernovae explosions on carbon nuclei.

With the standard assumptions (a supernova at the distance of 10 kpc from us, with 3×10^{53} erg energy release, equally divided between the six neutrino flavors[88]) we arrive at the KamLAND count rate of

$$N_\nu = \frac{35.3\langle\sigma\rangle}{T(\mathrm{MeV})} \text{ counts}, \tag{14}$$

where the thermally averaged cross section $\langle\sigma\rangle$ is in units of 10^{-42} cm^2 and the temperature is in MeV. We assume here that the detection efficiency is 100%.

Of particular interest for the supernova detection at KamLAND are the charged current reactions populating the ground states of ^{12}N and ^{12}B and the neutral current reactions populating the 15.11 MeV state in ^{12}C. The signal for these exclusive reactions will be essentially background free due to the possibility of observing the delayed coincidence of the charged current reactions and the sharp peak at 15.11 MeV for the neutral current reaction.

The expected number of events is shown in Table 14 where we made the usual assumptions about the temperatures of different neutrino flavors indicated in Column 1. The first three lines give the number of events expected without effects of neutrino oscillations. The fourth line gives the expected number of events when vacuum oscillations (and maximum mixing) are present such as in the “just so” oscillation scenario of the solar neutrino puzzle. Finally, in the last line we show the number of events expected for the matter-enhanced MSW oscillations.

Temperature (MeV)	$\nu_e {}^{12}\mathrm{C} \rightarrow {}^{12}\mathrm{N}_{gs} e^-$	$\bar{\nu}_e {}^{12}\mathrm{C} \rightarrow {}^{12}\mathrm{B}_{gs} e^+$	$\nu_x {}^{12}\mathrm{C} \rightarrow {}^{12}\mathrm{C}(15.11)\ \nu_x$
3.5 (ν_e)	1.9	-	1.5
5.0 ($\bar{\nu}_e$)	-	7.4	4.2
8.0 (ν_x)	-	-	51.9$^{a)}$
vacuum osc.	14.5	13.8	57.6$^{b)}$
MSW osc.	27	7.4	57.6$^{b)}$

Table 14: Expected rates in KamLAND for supernova neutrinos scattering on carbon. Different cases discussed in the text are presented. In $^{a)}$ we add the contribution of all ν_x and their antiparticles while in $^{b)}$ we give the total number of 15.11 MeV photons detected.

Thus, one can see that using these reactions, one can exclude, or confirm, various oscillation hypotheses. So, for example, if the "just so" neutrino oscillations are responsible for the solar neutrino deficit, we expect to see 14.5 counts in the $\nu_{\mathrm{e}}^{12}\mathrm{C} \rightarrow^{12} \mathrm{N}_{\mathrm{gs}}\mathrm{e}^-$ channel, and 13.8 counts in the $\bar{\nu}_{\mathrm{e}}^{12}\mathrm{C} \rightarrow^{12} \mathrm{B}_{\mathrm{gs}}\mathrm{e}^+$ channel. That would represent about 5 σ, i.e. enough to claim a discovery of this solution of the solar neutrino problem.

Another possibility is the MSW matter-enhanced neutrino oscillations $\nu_{\mathrm{e}} \leftrightarrow \nu_{\mathrm{x}}$. In that case we would observe 27 counts in the $\nu_{\mathrm{e}}^{12}\mathrm{C} \rightarrow^{12} \mathrm{N}_{\mathrm{gs}}\mathrm{e}^-$, again a 5 standard deviations effect. No other neutrino detector offers such a sensitivity to this oscillation mode.

But most important is the neutral current excitation of the 15.11 MeV state. This signal, dominated ($\sim$ 90%) by the ν_x neutrinos, will be visible at more than 5 standard deviations level above the more numerous positrons from the reaction $\bar{\nu}_{\mathrm{e}} + \mathrm{p} \rightarrow \mathrm{e}^+ + \mathrm{n}$. This will allow to determine at KamLAND the ν_x temperature to ± 1 MeV. This would be a very significant result.

A few detectors with liquid scintillators and hence containing carbon exist, or are being built (MACRO, LVD, BOREXINO). However, none of them can compete with the size and resolution of KamLAND.

We thus conclude that the target size and composition at KamLAND guarantee unique supernovae observations that will complement the higher statistics of Super-Kamiokande with a number of specific measurements.

A.2 Terrestrial Anti-Neutrinos

The earth radiates about 40 TW of heat from its surface. About 40% of this energy (or 16 TW) is believed to have radiogenic origin with 90% of it deriving from decays of ^{238}U and ^{232}Th. Radiogenic heat is therefore an essential component of the present dynamics of our planet. As discussed by several authors[81] these phenomena could be directly studied by detecting anti-neutrinos from the β decays of these actinides (terrestrial anti-neutrinos). KamLAND will be able to detect the terrestrial anti-neutrinos for the first time and thus open a new field in geophysics.

Since the maximum energy of terrestrial anti-neutrinos is 3.27 MeV, the maximum in the prompt part of the detected event will be 2.49 MeV (including the annihilation radiation). The expected observed energy spectrum will have a characteristic double hump structure shown in Fig. 35. As shown in the Figure, the reactor neutrino signal will be readily separated from the terrestrial anti-neutrino signal.

The two lower spectra (Ia and Ib) superimposed in Fig.35 correspond to two different possible geophysical models of the heavy element concentration in the oceanic and continental crusts [84]. In one year of data taking, model Ia would give an integral of 61 events, while model Ib would give only 41 events. Differentiation between them at 3σ level could be obtained in five years of data taking.

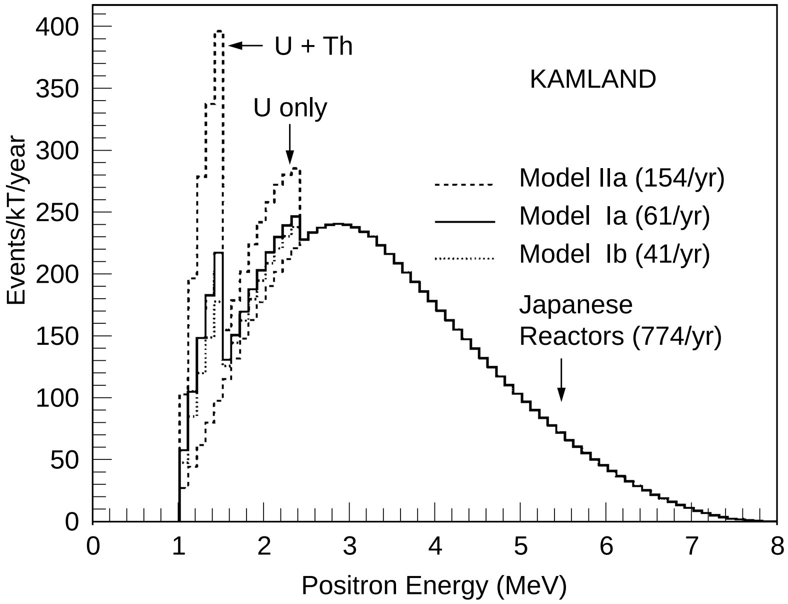

Figure 35: Energy spectrum from terrestrial anti-neutrinos compared with reactor signal as expected in KamLAND. Three different geophysical models are shown for the terrestrial anti-neutrinos and no oscillations are assumed for all the spectra shown.

A.3 Solar and Astrophysics Anti-Neutrinos

KamLAND will be the first large detector capable of identifying electron-anti-neutrinos from extraterrestrial sources with very small backgrounds, hence opening an entirely new window for the exploration of unknown phenomena. The double coincidence scheme used by KamLAND to identify $\bar{\nu}_{\mathrm{e}}$ provides a very effective background rejection, so that the expected instrumental background due to muon-produced neutrons and γ-rays from natural radioactivity and cosmogenic isotopes will amount to less than 0.1 event/day above 8 MeV. (Below 8 MeV the reactor and terrestrial neutrinos will dominate.)

One possible source of $\bar{\nu}_{\mathrm{e}}$ is the Sun, possibly by the magnetic/flavor transitions or by oscillations $\nu \rightarrow \bar{\nu}$. We will consider that as a generic case and compare our sensitivity to such $\bar{\nu}_{\mathrm{e}}$ to the present and ultimate sensitivities of SuperKamiokande, as described in[98]. There, the limit on the anti-neutrino flux of $\phi_{\bar{\nu}_{\mathrm{e}}} < 9 \times 10^4 \mathrm{cm}^{-2}\mathrm{s}^{-1}$ at 95%CL for energies above 8.3 MeV was obtained. In three years of data-taking this would give, for SuperKamiokande, a 95%CL limit of about 1% of the solar neutrino flux. Such flux would produce in KamLAND a clear signal of $\simeq$ 900 events/yr in the region above 8.3 MeV, where backgrounds for this type of events are expected not to exceed 30 events/yr. Hence in one year we could put a 95%CL upper limit on the antineutrino flux of $\phi_{\bar{\nu}_{\mathrm{e}}} < 3 \times 10^3 \mathrm{cm}^{-2}\mathrm{s}^{-1}$, or 0.1% of the flux of neutrinos from the sun.

Finally, another possible source of low energy anti-neutrinos could be given by the relics of gravitational collapses of massive stars. Such catastrophic events produced ν and $\bar{\nu}$ that accumulated in the universe. The number of such neutrinos is directly related to the amount of the baryonic matter bound in black holes and neutron stars, and their average energy is expected to be around 15 MeV. Because of the red shift, the energy spectrum carries information on the time distribution of large collapses during the history of our universe. While our ignorance on these parameters makes flux predictions generally uncertain a possible detection would be an extremely exciting feat. Following [100] we assume a constant rate of gravitational collapses and a mean density of matter in the universe of $10^{-31}\mathrm{g/cm}^3$, thus we would expect to detect about 40 $\bar{\nu}_{\mathrm{e}}$/yr above 8 MeV of energy in our detector. Different flux estimates, for instance[101], give substantially more pessimistic values. We note, however, that since the energy spectrum for these neutrinos is strongly peaked around few MeV, a low energy anti-neutrino detector such as KamLAND compares well with the much larger SuperKamiokande which suffers from a substantially larger "background" from solar neutrinos.

A.4 High Multiplicity Physics

One remarkable feature of the KamLAND detector will be its ability to completely reconstruct, with high efficiency, complex events, with non trivial time-sequences of energy depositions, in a very large volume of scintillator. This multihit capability is required for high efficiency detection of neutrons from anti-neutrino capture and background suppression. Here we explore the physics signatures that could benefit from this property of our detector.

A possible signal for new physics beyond the Standard Model would be the experimental evidence for nucleon instability. Large volume Čerenkov detector are ill suited for certain modes of nucleon decay, e.g for the “invisible” mode n $\rightarrow \nu\overline{\nu}\nu$. This mode can only be searched for indirectly, either by detecting neutrinos produced in the whole Earth by such decay [106], or by observing the nuclear relaxation following the sudden disappearance of a neutron in a nucleus. This last technique was pioneered by Kamiokande [103, 104] that has achieved the present best limit for the mode at $\tau > 4.9 \times 10^{26}$ y.

There are many reasons of principle to think that n $\rightarrow \nu\overline{\nu}\nu$ could be a very powerful indicator for new physics [105]. KamLAND, even with a mass substantially smaller than SuperKamiokande, will be competitive in the search for this mode, being able to detect low energy γ’s as well as heavy particles and, hence, accessing substantially more nuclear relaxation modes.

In a similar fashion our low energy, multihit capability may complement other detectors in the quest to understand the atmospheric neutrino anomaly. While until recently the study of atmospheric neutrinos has been limited to inclusive final states tagged by a lepton, recently SuperKamiokande [107] has performed an analysis of modes tagged by a π^0 and no lepton in the final state. Such modes are important since, being neutral currents, they are produced by all neutrino flavors and hence give a normalization to the rest of the measurements.

KamLAND will study modes with charged pions or other mesons and, in addition, some of the modes will be detected with very little background, thanks to the tag given by de-excitation of nuclei excited by the neutrino interaction. This technique, analogous to the one used in the detection of supernovae on carbon, will allow us to investigate, with low statistics but greater detail, the atmospheric neutrino anomaly.

A.5 Neutron Production by Muons

The muons penetrating deep underground and interacting with the rock in the vicinity of an underground detector are sources of a significant background. This background is reduced in practical applications by an active veto shield outside the fiducial volume which tracks the most dangerous muons (those close to the fiducial volume), and also eliminates charged particles created by the muon. In addition, the flux of the neutral particles (primarily neutrons) is reduced by the passive buffers surrounding the fiducial volume.

The quantitative description of the muon interaction with the rock deep underground is largely missing. It would be very useful for the whole field of underground physics to obtain data on the different aspects of the problem: a) how many neutrons are produced per muon in different depths, b) what is the energy distribution of these neutrons, and c) what is the angular distribution of the neutron with respect to the muon?

In KamLAND the muon flux is about $10^{-3}\mu/(\mathrm{m}^2\ \mathrm{s})$ and the muon rate through the whole detector is about 0.3 Hz. Half of the muons go only through the veto and the inert buffer and we estimate that they produce about 0.1 Hz of neutrons by muon spallation. A fraction of them ($\simeq 50\%$) will penetrate into the active scintillator volume, be moderated and eventually captured. A simple dedicated trigger will accept and tag a fraction of the events in which muons go through the veto, allowing us to accurately test the various scenarios of the muon spallation.

A rudimentary program along these lines has been recently carried out by the Soudan-2 collaboration [111]. While their measurement clearly shows the feasibility of such a program, KamLAND will be able to extract solid numbers that will benefit the entire community of underground detectors.

A.6 Double Beta Decay with KamLAND

The investigation of the neutrinoless double beta ($\beta\beta0\nu$) decay is at present the most sensitive probe for a Majorana neutrino mass. The extraordinary mass sensitivity of $\beta\beta0\nu$ could be crucial to establish the absolute neutrino mass scale, should neutrinos be Majorana particles. The most competitive limits obtained through this technique thus far are $\langle m_\nu \rangle < 0.5$ - 1.0 eV [112] and $\langle m_\nu \rangle < 0.2$ eV [113]

This subsection will discuss the potential of the KamLAND detector for a $\beta\beta0\nu$ experiment, and define the requirements in terms of scintillator purity and isotope loading.

The B-L number violating $\beta\beta0\nu$-decay requires massive Majorana neutrinos and hence the existence of physics beyond the Standard Model. The decay rate $(T^{0\nu}_{1/2})^{-1}$ is given by (neglecting right-handed admixtures to the weak interaction):

$$(T^{0\nu}_{1/2})^{-1} = F^{0\nu} \cdot |M^{0\nu}|^2 \cdot (\frac{\langle m_\nu \rangle}{m_e})^2, \qquad (15)$$

with $F^{0\nu}$ the phase space integral, $M^{0\nu}$ the nuclear matrix element, m_e the electron mass and $\langle m_\nu \rangle$ the effective Majorana neutrino mass. A measured $\beta\beta0\nu$ decay rate or a limit for it allows hence to draw conclusions on the fundamentally important quantity $\langle m_\nu \rangle$. We use nuclear matrix element calculations of [114] in our rate estimates, as this theoretical model covers almost all double-beta emitters.

To search for $\beta\beta0\nu$-decay with the KamLAND detector we would need to dissolve a large quantity of a $\beta\beta$ unstable isotope in the liquid scintillator. This will allow a calorimetric measurement of the sum energy of the emitted electrons as proposed in [115]. Like for the detection of solar neutrinos, in this approach $\beta\beta$-decays have no specific signature which would allow to suppress backgrounds. The two main experimental difficulties to be addressed are:

- The comparably low abundance of the decaying isotopes in the detector requires very low radioactivity concentrations in the liquid scintillator.
- The relatively poor energy resolution of liquid scintillator will scatter $\beta\beta2\nu$-events into the analysis energy window of the $\beta\beta0\nu$-mode thus causing an irreducible background.

Despite these inherent difficulties the KamLAND detector does allow the use of ton quantities of $\beta\beta$-emitters to be compared to kilograms (of highly enriched ^{76}Ge) in todays most sensitive experiment. This gain of almost three orders of magnitude in source strength might allow for the first time the exploration of Majorana neutrino masses below 0.1 eV. An additional advantage of KamLAND would be that most of the background could be measured before the scintillator is loaded with the double-beta emitter. If an effect would be observed with one double-beta emitter the measurement could be repeated by loading with a different isotope. In order to alleviate the two limitations described, scintillators with high loading and large light yield are essential. In our estimates we use $\sigma(E)/E = 10\%/\sqrt{E}$. In the following we will also use the same background model as in the solar neutrino section.

From all double beta emitters which have been considered for this estimate, ^{136}Xe is the most promising candidate. The noble gas Xe dissolves to up to 2% by weight in various organic solvents as benzene, cyclohexane, hexane, 2-methylheptane and dodecane [116]. In our estimate we will conservatively use a 1% concentration. We are planning to perform tests in our laboratories to determine what effect such concentrations have on light yield, transparency and stability of the scintillator. Although Xe has no radioactive isotopes, contaminations with radioactive noble gases, i.e., ^{85}Kr ($T_{1/2}$=10.7 y, Q_β=0.69 MeV, fission product) and ^{42}Ar ($T_{1/2}$=33 y, Q_β=3.52 MeV, atmospheric spallation) have to be carefully studied. The Caltech-Neuchatel-PSI double-beta experiment using enriched Xe gas in a TPC measures a U/Th concentration of 10^{-12} g/g in their counting gas using $\alpha-\beta$-coincidences [117]. In KamLAND we would need at least a factor 100 better Xe purity that could possibly be achieved by distillation since the three gases have quite different boiling points. The Caltech-Neuchatel-PSI TPC could probably be used in a not-too-far future to test Xe samples for radioactive contamination.

Since Xe is a gas at STP it is relatively easy to enrich isotopically by means of centrifugation. We have started to explore this possibility with the Kurchatov Institute in Russia and found that the quantities of isotope required, although very large, are not beyond the capacity of their facilities. This option will be further discussed in the future. In our estimate we will present both the case of natural Xe (8.9% ^{136}Xe) and Xe enriched to 89% ^{136}Xe.

Calculations predict a rate of $\beta\beta2\nu$-event as high as 0.02 and 0.2 s^{-1} for the two isotopic compositions. A Majorana neutrino mass of $\langle m_\nu \rangle = 0.1$ eV would give a $\beta\beta0\nu$-event rate of 12 and 122 events/year in the two cases. This very small signal rate defines the background requirements.

Component	Low reduction		High reduction	
	Xe^{nat} $[d^{-1}]$	Xe^{enr} $[d^{-1}]$	Xe^{nat} $[d^{-1}]$	Xe^{enr} $[d^{-1}]$
$\beta\beta 2\nu$	0.028	0.28	0.028	0.28
^{232}Th	$4 \cdot 10^{-3}$	$4 \cdot 10^{-3}$	$4 \cdot 10^{-3}$	$4 \cdot 10^{-3}$
^{238}U	1	1	0.2	0.2
^{222}Rn	1	1	0.2	0.2
^{40}K	0	0	0	0
Σ $[d^{-1}]$	2.1	2.3	0.44	0.69
$N_{\beta\beta 0\nu}$ $(\varepsilon = 0.48)$ $[y^{-1}]$	73	78	33	42
$T^{0\nu}_{1/2}$ [y]	$3.7 \cdot 10^{25}$	$3.5 \cdot 10^{26}$	$8.1 \cdot 10^{25}$	$6.4 \cdot 10^{26}$
$\langle m_\nu \rangle$ [eV]	0.24	0.08	0.17	0.06

Table 15: Background rates and neutrino mass sensitivity achievable with 10 tons of natural or enriched (89% ^{136}Xe) (1% loading). The estimate is done for the "high purity" scintillator model defined in the previous section. The two left columns contain our estimate for a ^{214}Bi reduction factor of 20 ("low reduction"), while for the right two columns a reduction factor of 100 ("high reduction") was assumed to account for $\alpha - \beta$-tagging. The line "$N_{\beta\beta 0\nu}$" denotes the limit on the counting rate that one can extract from the background. $T^{0\nu}_{1/2}$ and $\langle m_\nu \rangle$ are then derived from these counting rates.

We use $[Q_{\beta\beta}, Q_{\beta\beta}+2\cdot\sigma]$ as analysis interval I for the $\beta\beta 0\nu$-decay. This asymmetric interval reduces the $\beta\beta 2\nu$ irreducible background to reasonable levels yet maintaining an efficiency of 48% for the signal. Since the dominant source of background in I is ^{214}Bi from ^{222}Rn and ^{238}U in the scintillator, the achievable sensitivity strongly depends on our assumption on the tagging efficiency for the ^{214}Bi-^{214}Po sequence. Assuming such tagging efficiency to be 95% (99%) we obtain the "Low reduction" ("High reduction") result summarized in Table 15. We believe that such reduction factors are quite reasonable for such a short time sequence.

It is worthwhile to mention that among the running double-β decay experiments the largest source is ~10 kg of isotopically enriched ^{76}Ge [112]. This experiment, performed in the Gran Sasso underground laboratory in Italy, plans to reach a neutrino mass limit of about 0.2 eV few years from now. The French-Russian-US NEMO project in the Fréjus tunnel is in an advanced stage of preparation and will reach a sensitivity comparable to the Ge project mentioned above.

Several dedicated, very complex and expensive double-β decay experiments could handle sources of the size discussed for KamLAND. Particularly interesting are a much larger ^{76}Ge experiment at Gran Sasso ("GENIUS" [118]) and a cryogenic ^{130}Te search [119] also to be performed at Gran Sasso. Besides the acquisition of the costly enriched source material both these project require a substantial effort to build a large detector of complexity and cost comparable to our detector. In KamLAND's high purity phase we would only need to worry about the double-β source.

Our conclusion is that KamLAND in the future could be a competitive detector for a double-beta decay search. Although it is obvious that this physics is not within the reach of the initial phase of the experiment, the possibility of reaching 60 meV neutrino mass sensitivity strongly motivates the collaboration to study further the possibility of performing this type of measurements. As stated above, we expect to collect a wealth of information on the possible backgrounds and problems connected with double-beta decay while running the first phase of the experiment.

B Decay Chains of Selected Isotopes

^{238}U (4.5×10^9 y)	E_α	E_γ	per ^{238} U decays
|	4198	-	0.790
↓	4151	50	0.210
^{234}Th (24.1 d)	E_{β^-} Endpoint	E_γ	per ^{238} U decays
|	273	-	0.703
|	160	113	0.022
|	181	92	0.192
↓	136	137	0.083 *
^{234}Pa (1.2 m)	E_{β^-} Endpoint	E_γ	per ^{238} U decays
|	2197	-	0.982
|	1153	1001,43	0.009
↓	1099	1098	0.009 *
^{234}U (2.5×10^5 y)	E_α	E_γ	per ^{238} U decays
|	4775	-	0.714
↓	4722	53	0.286
^{230}Th (7.5×10^4 y)	E_α	E_γ	per ^{238} U decays
|	4688	-	0.763
↓	4621	68	0.237
^{226}Ra (1600 y)	E_α	E_γ	per ^{238} U decays
|	4784	-	0.944
↓	4602	186	0.056
^{222}Rn (3.8 d)	E_α	E_γ	per ^{238} U decays
↓	5490	-	1.000
^{218}Po (3.1 m)	E_α	E_γ	per ^{238} U decays
↓	6002	-	1.000
^{214}Pb (26.8 m)	E_{β^-} Endpoint	E_γ	per ^{238} U decays
|	1023	-	0.093
|	184	839	0.006
|	234	786,53	0.009
|	671	352	0.460
|	728	295	0.288
|	728	242,53	0.117
↓	511	512	0.027 *

^{214}Bi (19.9 m)	E_{β^-} Endpoint	E_γ	per ^{238}U decays
$\vert$	3272	-	0.199
$\vert$	790	1208,665,609	0.005
$\vert$	824	2448	0.015
$\vert$	824	1838,609	0.004
$\vert$	1068	2204	0.048
$\vert$	1153	1509,609	0.022
$\vert$	1153	2119	0.012
$\vert$	1255	1408,609	0.029
$\vert$	1261	1402,609	0.015
$\vert$	1278	1385,609	0.009
$\vert$	1382	1281,609	0.015
$\vert$	1425	1847	0.021
$\vert$	1425	1238,609	0.059
$\vert$	1508	1764	0.149
$\vert$	1508	1155,609	0.016
$\vert$	1542	1120,609	0.144
$\vert$	1542	1730	0.028
$\vert$	1729	934,609	0.027
$\vert$	1857	806,609	0.009
$\vert$	1894	1378	0.032
$\vert$	1894	768,609	0.040
$\downarrow$	1636	1636	0.102*
^{214}Po (164 μs)	E_α	E_γ	per ^{238}U decays
$\vert$	6902	800	0.0001
$\downarrow$	7687	-	0.9999
^{210}Pb (22 y)	E_{β^-} Endpoint	E_γ	per ^{238}U decays
$\vert$	64	-	0.160
$\downarrow$	17	47	0.840
^{210}Bi (5.0 d)	E_{β^-} Endpoint	E_γ	per ^{238}U decays
$\downarrow$	1163	-	1.000
^{210}Po (138 d)	E_α	E_γ	per ^{238}U decays
$\downarrow$	5304	-	1.000
^{206}Pb (∞)			

Table 16: ^{238}U decays chain. Only decays with visible energy larger than 100 keV or branching ratio more than 0.5% are listed. Effects of internal conversion are not included as they have negligible effects on our calculations for a very large detector.

^{232}Th (1.4 × 10^{10} y)	E_α	E_γ	per ^{232} Th decays
│	4013	-	0.779
↓	3954	64	0.221

^{228}Ra (5.8 y)	E_{β^-} Endpoint	E_γ	per ^{232} Th decays
↓	46	-	1.000

^{228}Ac (6.1 h)	E_{β^-} Endpoint	E_γ	per ^{232} Th decays
│	2069	58	0.100
│	403	755, 911, 58	0.007
│	438	1631, 58	0.020
│	438	1502, 129, 58	0.006
│	444	1496, 129, 58	0.009
│	481	1588,58	0.031
│	481	1459, 129, 58	0.008
│	596	99, 463,911,58	0.015
│	596	99,463,969	0.011
│	596	99,409,965,58	0.008
│	596	563,911,58	0.016
│	596	563,969	0.009
│	596	509,965,58	0.010
│	959	772,338,58	0.012
│	959	840,270,58	0.005
│	973	322,774,58	0.005
│	973	322,503,328	0.005
│	973	322,503,270,58	0.006
│	973	1096,58	0.009
│	973	1154	0.010
│	1004	795,328	0.020
│	1004	795, 270,58	0.023
│	1104	965, 58	0.023
│	1104	836,128,58	0.007
│	1158	969	0.116
│	1216	911	0.191
│	1731	209,129,58	0.030
│	1731	338,58	0.086
↓	1063	1064	0.202 *

^{228}Th (1.9 y)	E_α	E_γ	per ^{232} Th decays
|	5423	-	0.715
↓	5340	84	0.285
^{224}Ra (3.7 d)	E_α	E_γ	per ^{232} Th decays
|	5685	-	0.949
↓	5449	241	0.051
^{220}Rn (56 s)	E_α	E_γ	per ^{232} Th decays
↓	6288	-	1.000
^{216}Po (0.145 s)	E_α	E_γ	per ^{232} Th decays
↓	6778	-	1.000
^{212}Pb (11 h)	E_{β^-} Endpoint	E_γ	per ^{232} Th decays
|	574	-	0.123
|	274	300	0.052
↓	335	239	0.825
^{212}Bi (61 m)	E_{β^-} Endpoint	E_γ	per ^{232} Th decays
|	2254	-	0.555
| 64%	634	1620	0.015
|	742	785,727	0.011
|	1527	727	0.044
↓	1127	1127	0.015*
^{212}Po (299 ns)	E_α	E_γ	per ^{232} Th decays
↓	8784	-	0.640
^{208}Pb (∞)			
^{212}Bi (61 m)	E_α	E_γ	per ^{232} Th decays
| 36%	6090	-	0.098
↓	6050	40	0.262
^{208}Tl (3.1 m)	E_{β^-} Endpoint	E_γ	per ^{232} Th decays
|	1040	763,583,2615	0.008
|	1292	511,583,2615	0.085
|	1525	861,2615	0.052
|	1525	277, 583, 2615	0.026
|	1803	583,2615	0.175
↓	2500	2501	0.014 *
^{208}Pb (∞)			

Table 17: ^{232}Th decays chain. Only decays with visible energy larger than 100 keV or branching ratio more than 0.5% are listed. Effects of internal conversion are not included as they have negligible effects on our calculations for a very large detector.

^{40}K (1.3×10^9 y)	E_{β^-} Endpoint	E_γ	per ^{40} K decays
↓ 89.3%	1311	-	0.893
^{40}Ca (∞)			
^{40}K (1.3×10^9 y)		E_γ	per ^{40} K decays
| 10.7%		1461	0.105
↓		-	0.002
^{40}Ar (∞)			

Table 18: ^{40}K decays chain. Decays with visible energy less than 100 keV or branching ratio more than 0.5% are listed.

^{60}Co (5.3 y)	E_{β^-} Endpoint	E_γ	per ^{60} Co decays
↓	318	1173, 1333	1.000
^{60}Ni (∞)			

Table 19: ^{60}Co decays chain. Decays with visible energy less than 100 keV or branching ratio more than 0.5% are listed.

References

[1] Z. Maki, M. Nakagawa and S. Sakata, Prog. Theor. Phys., **28**, 870 (1962).

[2] B. Pontecorvo, Zh. Eksp. Teor. Fiz. **53**, 1717 (1967).

[3] L. Wolfenstein, Phys. Rev. **D 17**, 2369 (1978); S.P. Mikheyev and A.Yu. Smirnov, Yad. Fiz. **42**, 1441 (1985) (Sov. J. Nucl. Phys. **42**, 1441 (1985)); Nuovo Cim. **9C**, 17 (1986); S.P. Rosen and J. M. Gelb, Phys. Rev. **D34**, 969 (1986); S.J. Parke, Phys. Rev. Lett. **57**, 1275 (1986); S.J. Parke and T.P. Walker, Phys. Rev. Lett. **57**, 2322 (1986); W.C. Haxton, Phys. Rev. Lett. **57**, 1271 (1986); T.K. Kuo and J. Pantaleone, Rev. Mod. Phys. **61**, 937 (1989).

[4] Particle Data Group, Eur. Phys. J., **3**, 1 (1998). See especially, pp. 320-330.

[5] Kamiokande Collaboration (K.S.Hirata et al.), Phys. Lett. **B205**, 416 (1988); **280**, 146 (1992).

[6] IMB Collaboration (D.Casper et al.), Phys. Rev. Lett. **66**, 2561 (1991); IMB Collaboration (R.Becker-Szendy et al.), Phys. Rev. **D 46**, 3720 (1992).

[7] Soudan-II Collaboration (W.W.M.Allison et al.), Phys. Lett. **B 391**, 491 (1997).

[8] Super-Kamiokande Collaboration (Y. Fukuda et al.), Phys. Lett. **B433**, 9 (1998).

[9] Fréjus Collaboration. (K. Daum et al.), Z. Phys. **C66**, 417 (1995).

[10] Kamiokande Collaboration (Y.Fukuda et al.), Phys. Lett. **B 335**, 237 (1994).

[11] Super-Kamiokande Collaboration (Y. Fukuda et al.), Phys. Lett. **B436**, 33 (1998).

[12] Super-Kamiokande Collaboration (Y. Fukuda et al.), Phys. Rev. Lett. **81**, 1562 (1998).

[13] CHOOZ Collaboration (M. Apollonio et al.), Phys. Lett. **B420**, 397 (1998).

[14] G. Gratta, to appear in Proceedings of WIN 99, Cape Town, South Africa, January 1999.

[15] M. Messier for Super-Kamiokande Collaboration, American Physical Society, The Division of Particles and Fields Conference, University of California, Los Angeles, January 5-9, 1999.

[16] V. Barger, S. Pakvasa, and T.J. Weiler, Phys. Lett. **B437**, 107 (1998).

[17] LSND Collaboration (C. Athanassopoulos et al.), Phys. Rev. Lett. **81**, 1774 (1998).

[18] LSND Collaboration (C. Athanassopoulos et al.), Phys. Rev. **C58**, 2489 (1998).

[19] http://www.neutrino.lanl.gov/LSND/DNP.html

[20] For information, see `http://www-ik1.fzk.de/www/karmen/karmen_e.html`.

[21] For information, see `http://www.neutrino.lanl.gov/BooNE`.

[22] J. N. Bahcall, "Neutrino Astrophysics," Cambridge University Press, (1989).

[23] J.N. Bahcall and M.H. Pinsonneault, Rev. Mod. Phys. **67**, 781 (1995).

[24] B.T. Cleveland, T. Daily, R. Davis, J.R. Distel, K. Lande, C.K. Lee, P.S. Wildenhain, J. Ullman., Astrophys. J. **496**, 505 (1998).

[25] GALLEX Collaboration (M. Cribier for the collaboration), Nucl. Phys. Proc. Suppl. **70**, 284 (1999).

[26] SAGE Collaboration (D.N. Abdurashitov et al)., Nucl. Phys. Proc. Suppl. **48**, 299 (1996).

[27] Kamiokande Collaboration (Y. Fukuda et al.), Phys. Rev. Lett. **77**, 1683 (1996).

[28] Super-Kamiokande Collaboration (Y. Fukuda et al.), Phys. Rev. Lett. **81** 1158 (1998), Erratum-ibid. **81** 4279 (1998); hep-ex/9812009; hep-ex/9812011.

[29] J.N. Bahcall, P.I. Krastev, and A.Yu. Smirnov, Phys. Rev. **D58**, 096016 (1998).

[30] M. Fukugita and A. Suzuki, "Physics and Astrophysics of Neutrinos", Springer Verlag, 1994.

[31] J N. Bahcall and P. I. Krastev, Phys. Lett. **B436** 243 (1998).

[32] For information, see `http://www.hep.anl.gov/NDK/HyperText/numi.html`.

[33] P. Vogel, Phys. Rev. **D29**, 1918 (1984).

[34] K. Schreckenbach *et al.*, Phys. Lett. **B99**, 251 (1981); **B160**, 325 (1985); F. von Feilitzsch *et al.*, Phys. Lett. **B118**, 162 (1982); A. A. Hahn *et al.*, Phys. Lett. **B218**, 365 (1989).

[35] See for example Y. Declais *et al.* Phys. Lett. **B 338**, 383 (1998); G. Zacek *et al.* Phys. Rev. **D 34**, 2621 (1986).

[36] G. Zacek *et al.* Phys. Rev. **D 34**, 2621 (1986).

[37] The Federation of Electric Power Companies, Japan, "Status of Electric Power Industry 1996-97", in Japanese.

[38] For information, see `http://almime.mi.infn.it/`.

[39] Borexino Collaboration (G. Alimonti et al.), Nucl. Instr. and Methods, **A 406**, 411 (1998).

[40] Borexino Collaboration (G. Alimonti et al.), Astroparticle Physics, 8 (1998) 141.

[41] Borexino Collaboration (G. Ranucci et al.), Nucl. Phys. Proc. Suppl. **70**, 377 (1999).

[42] For information, see `http://www.sno.phy.queensu.ca/`.

[43] J. M. Gelb and S.P. Rosen, hep-ph/9809508.

[44] A. Friedland, A. de Gouvêa, and H. Murayama, in preparation.

[45] J.N. Bahcall and P.I. Krastev, Phys. Rev. **C56**, 2839 (1997).

[46] J. N. Bahcall, S. Basu, and M.H. Pinsonneault, Phys. Lett. **B433**, 1 (1998).

[47] K. Hirata, *et al.*, Phys. Rev. **D44**, 2241 (1991).

[48] G.L. Cassiday *et al.*, Phys. Rev. D 7 (1973) 2022.

[49] M. Aglietta et al. Nuovo Cimento **C12**,467(1989).

[50] F.F. Khalchukov*et al.*, Nuovo Cimento, 6C (1983) 320.

[51] K.V. Alanakyan*et al.*, Sov. J. Nucl. Phy. 34 (1981) 828.

[52] J. Delorme ét al. Phys. Rev. **C52**, 2222 (1995).

[53] BOREXINO Collaboration, private communication from M. Chen.

[54] J. Cugnon *et al.* Nucl. Phys. A 625 (1997) 729; A. Ferrari *et al.* Z. Phys. C 70 (1996) 413, Z. Phys. C 71 (1996) 75.

[55] W.R. Webber *et. al*, Phys. Rev. C 41(1990)547.

[56] V. McLane *et. al*, "Neutron Cross Sections", Vol.2, Academic Press, Inc. 1988.

[57] G. Alimonti *et al.* Phys. Lett. B 422 (1998) 349.

[58] L. Oberauer, Private communication, scaled from the yield measured in a CERN test beam.

[59] R.B. Firestone, V.S. Shirley *et al.* "Table of Isotopes" Eighth Edition, Wiley Interscience 1996.

[60] R. Brun, *et al.*, "GEANT 3", CERN DD/EE/84-1 (revised), 1987.

[61] P. A. Aarnio, *et al.*, "FLUKA user's guide", TIS-RP-190, CERN, 1990

[62] T. A. Gabriel, *et al.*, ORNL/TM-5619-mc, April 1977.

[63] SuperKamiokande Collaboration, Private Communication.

[64] J.B. Birks, "The Theory and Practice of Scintillation Counting", McMillan, New York, 1964; J.B. Birks, "Photophysics of Aromatic Molecules", Wiley and Sons, London, 1970.

[65] J. B. Benziger, *et al.*, "A Scintillator Purification System for a Large Scale Solar Neutrino Experiment", submitted to NIM; J. B. Benziger, *et al.*, "A Large Scale Low Background Liquid Scintillation Detector: The Counting Test Facility at Gran Sasso", submitted to NIM; G. Bellini *et al.*, Nucl. Phys. Proc. Suppl. 48 (1996) 363.

[66] J. Shirai, “Purification System”, KamLAND-NOTE-97-06.

[67] G. Bellini *et al.*, Nucl. Phys. Proc. Suppl. 48 (1996) 363.

[68] See section 4.2 of G. Bellini *et al.*, Nucl. Phys. Proc. Suppl. 48 (1996) 363.

[69] R.S. Raghavan, “LENS”, Talk at Neutrino 98, Takayama, Japan, June 1998.

[70] P. Alivisatos, Science 271 (1996) 933.

[71] T. Taniguchi, A read-out system for Kam-LAND experiment, internal KamLAND note, December 1998

[72] H. Kurashige et al., A new data acquisition system for TRISTAN experiments using TKO box, IEEE Trans. on Nuclear Sci., v. 35, No.1 (1988) 257-260; H. Kurashige et al., A new data acquisition system adopting pipelined scheme for TKO box, IEEE Trans. on Nuclear Sci., v. 41, No.4 (1994) 1267-1270.

[73] A.L. Wintenberg, et al., ”Monolithic Circuits for the WA98 Lead Glass Calorimeter”, in Proceedings of NSS 94; M.L. Simpson, et al., ”An Integrated CMOS Time Interval Measurement System with Sub-nanosecond Resolution for the WA-98 Calorimeter”, *IEEE Journal of Solid-State Circuits*, vol. 32, No. 2, 1997, pp 198-205; A.L. Wintenberg, et al., ”A CMOS Integrating Amplifier for the PHENIX Ring Imaging Čerenkov Detector”, in Proceedings of NSS 97; A.L. Wintenberg, et al., ”The RICH Chip - A CMOS Integrated Circuit for the PHENIX Ring Imaging Čerenkov Detector”, to be published in the *IEEE Transactions on Nuclear Science*.

[74] C.L. Britton, et al., ”An Analog Random Access Memory in the AVLSI-RA Process for an Interpolating Pad Chamber”, IEEE Transactions on Nuclear Science, vol. 42, No 6, Dec. 1995

[75] G. Gratta *et al.*, NIM A 400 (1997) 456.

[76] KARMEN Collaboration, Private Communication.

[77] M. Roy-Barman, J.H. Chen and G.J. Wasserburg, Earth and Planetary Science Letters 139 (1996) 351

[78] P.S. Andersson et al., Earth and Planetary Science Letters 130 (1995) 217

[79] T. Goldbrunner et al., Nucl. Phys. B 61B (1998) 176

[80] G. Eders, Nucl. Phys., 78 (1966) 657.

[81] G. Marx, Czech. J. of Physics B, 19 (1969) 1471;
G. Marx and I. Lux, Acta Phys. Acad. Hung., 28 (1970) 63;
C. Avilez *et al.*, Phys. Rev. D23 (1981) 1116.

[82] L. Krauss *et al.*, Nature 310 (1984) 191.

[83] J.S. Kargel and J.S. Lewis, Icarus 105 (1993) 1.

[84] R.S. Raghavan *et al.*, Phys. Rev. Lett. 80 (1998) 635.

[85] C.G. Rothschild, M.C. Chen, F.P. Calaprice, Submitted to Geophys. Rev. Lett.

[86] Borexino at Gran Sasso, ed. G. Bellini *et al.* INFN Milano 1992,
R.S. Raghavan, Science 267 (1995) 45.

[87] Review of Particle Properties, Phys. Rev. D54 (1996)

[88] H.A. Bethe, Rev. Mod. Phys. 62 (1990) 801.

[89] H.T. Janka *et al.* Astrophys. J. 433 (1994) 229.

[90] J. Engel, E. Kolbe, K. Langanke, and P. Vogel, Phys. Rev. C **54**, 2740 (1996).

[91] C. Athanassouploulos et al., Phys. Rev. C **56**, 2806 (1997).

[92] B. Zetnitz, Prog. Part. Nucl. Phys. **32**, 351 (1994).

[93] Y.-Z. Qian et al., Phys. Rev. Lett. **71**, 1965 (1993).

[94] A. Antonioli et al. , Nuovo Cim. C **14**, 631 (1991).

[95] E.Kh. Akhmendov, Sov. Phys. JETP 68 (1989) 690;
H. Minakata and H. Nunokawa, Phys. Rev. Lett. 63 (1989) 121;
C.S. Lim and W.J. Marciano, Phys. Rev. D37 (1988) 1368;
E.Kh. Akhmendov, Phys. Lett. B257 (1991) 163;
E.Kh. Akhmendov, 4th International Solar Neutrino Conference, Heidelberg, Germany, Apr 1997.

[96] J.N. Bahcall, N. Cabibbo and A. Yahill, Phys. Rev. Lett. 28 (1972) 316;
J.N. Bachall *et al.*, Phys. Lett. B181 (1986) 396;
Z. Berezhiani *et al.*, Z. Phys. C54 (1992) 351 and JETP Lett. 55 (1992) 151;
Z. Berezhiani, M. Moretti and A. Rossi, Z. Phys. C58 (1993) 423.

[97] M.B. Voloshin, M.I. Vysotskii and L.B. Okun, Soviet J. Nucl. Phys. 44 (1986) 440;
P.A. Sturrock, G. Walter and M.S. Wheatland, Ap. J. 491 (1997) 409.

[98] G. Fiorentini, M. Moretti, F.L. Villante, Phys. Lett. B413 (1997) 378.

[99] Y. Fukuda *et al.* e-print Archive hep-ex/9805021, May 1998.

[100] G.V.Domogatskii Sov.Astron. 28, 30 (1984) 30.

[101] T. Totani *et al.* in proceedings of the 17^th International Conference on Neutrino Physics and Astrophysics, Helsinki, Finland 1996; World Scientific.

[102] M. Ambrosio *et al.* Phys. Lett. B 406 (1997) 249.

[103] Y.Totsuka, *in the Proceedings of the 7th Workshop on Grand Unification/ICOBAN '86*, edited by J.Arafune (World Scientific, Singapore, 1986), p. 118.

[104] H. Ejiri, *Phys. Rev.* **C48** (1993) 1442.

[105] Yu. Kamyshkov, *in the Proceedings of the First International Conference on Particle Physics Beyond the Standard Model*, Castle Ringberg, Germany, June 1997; Editor H.V. Klapdor-Kleingrothous, IOP Publishing Co., 1997, p. 542.

[106] C. Berger *et al.*, Phys. Lett. B269 (1991) 227.

[107] Y.Fukuda et al., Super-Kamiokande Collaboration, Talk presented by T.Kajita at Neutrino-98 Conference, Takayama, June 1998.

[108] M. Nakahata *et al.*, Jour. of Jap. Phys. Soc. 55 (1986) 3786.

[109] R. Hertenberger, M. Chen, and B. L. Dougherty, Phys. Rev. **C52**, 3449 (1995).

[110] J. Delorme, M. Ericson, T. Ericson, and P. Vogel, Phys. Rev. **C52**, 2222 (1995).

[111] E. A. Petterson, Neutrino-96, p.223, World Scientific, Singapore, 1997.

[112] L. Baudis et al., Phys. Lett. B 407 (1997) 219

[113] L. Baudis et al., Limits on the Majorana neutrino mass in the 0.1 eV range, hep-ex/9902014

[114] A. Staudt, K. Muto and H.V. Klapdor-Kleingrothaus, Euro. Phys. Lett. 13 (1990) 31

[115] R.S. Raghavan, Phys. Rev. Lett. 72 (1994) 1411

[116] H. Stephen and T. Stephen, Solubilities of Inorganic and Organic Compounds, (1963) 586

[117] F. Boehm, private communication, (1998)

[118] H.V. Klapdor-Kleingrothaus, Contribution to Neutrino 98, Takayama, Japan, Jun 98.

[119] O. Cremonesi, Contribution to Neutrino 98, Takayama, Japan, Jun 98.